UCLouvain

FACULTE DES SCIENCES

Faculté des sciences

Synthesis and Characterization of Novel Imidazole Crown Ethers for Host–Guest Interactions

Auteur : Can Karaman

Encadrant : Martin Schoenauen

Promoteur : Michael Singleton

Lecteurs : Charles Andre Fustin, Raphael Robiette et Yann Garcia

Année académique 2025-2026

Master [120] en sciences chimiques à finalité spécialisée : chimie de l'industrie

Acknowledgements

The completion of this thesis marks the end of my education at the graduate level. Therefore, I believe it is important to reflect on the work and express my gratitude to the people who made it possible.

Initially, I want to express my gratitude to Professor Michael Singleton for giving me the opportunity to work in his lab. His door was always open for questions and discussions. I am very appreciative of the guidance he provided in the context of the project, but also on other topics.

I also want to acknowledge Martin, whose day-to-day supervision made this good body of work possible. Answering all my questions and making the data publication ready. Also important to highlight his importance in the project, including assistance with data processing, helping with the supporting information, and extending the work further. But also, aside from the science our general discussions made coming to the lab more enjoyable.

It is also important to mention the group members Seb, Charles, Zahid, Saima, Louis, and Tatiana. They all individually contributed to creating a welcoming and productive lab environment. I truly could not have asked for a better group to perform my master thesis in.

I also want to express my gratitude to Koen, Laurent, Fabio and Gabriella. They all contributed in different ways to allow day to day research possible.

Finally, I want to thank my family who have supported me through all my studies. My parents, sister, aunts and uncles have all played an important individual role in getting me to where I am today. Supporting me in multiple ways including financially but also giving me important advice on next steps within my academic and professional journey.

Abstract

Crown ethers exhibit important supramolecular behaviour due to their ability to coordinate positively charged species. Due to this property, they have a wide variety of applications. Since the initial crown ether discovery there have been efforts made to incorporate various functional groups within the crown ether scaffold. These modifications lead to novel properties and increasing the possibility for important applications, emphasizing the need to create crown ether scaffolds with diverse substituents.

This project aims to synthesize a crown ether which incorporates an imidazole functional group spacing the ether functionalities. The incorporation of an imidazole can introduce novel properties to the crown ether, including tautomerization, pH responsiveness, and an N-atom in the cavity. In the literature, only a few imidazole-containing crown ethers have been reported. One of the most notable examples is the work of Zimmerman. However, the proposed synthetic route requires numerous steps and resulted in low overall yields.

Here the concerted synthesis of a protected imidazole macrocycle is reported with an overall yield ranging between 2 to 13%. Following the synthesis, host-guest studies were performed via NMR titrations with KPF_6 and $NaPF_6$ to assess their binding properties. Demonstrating that the newly synthesized imidazole crown ethers generally have similar binding properties to classical crown ethers. However, subtle differences in geometry and binding strength due to the incorporation of the imidazole were also observed. The binding properties were further extended to pseudorotaxane formation through the complexation of secondary ammonium ions. Interestingly, the novel crown ether exhibited exceptional affinity to secondary ammonium ions.

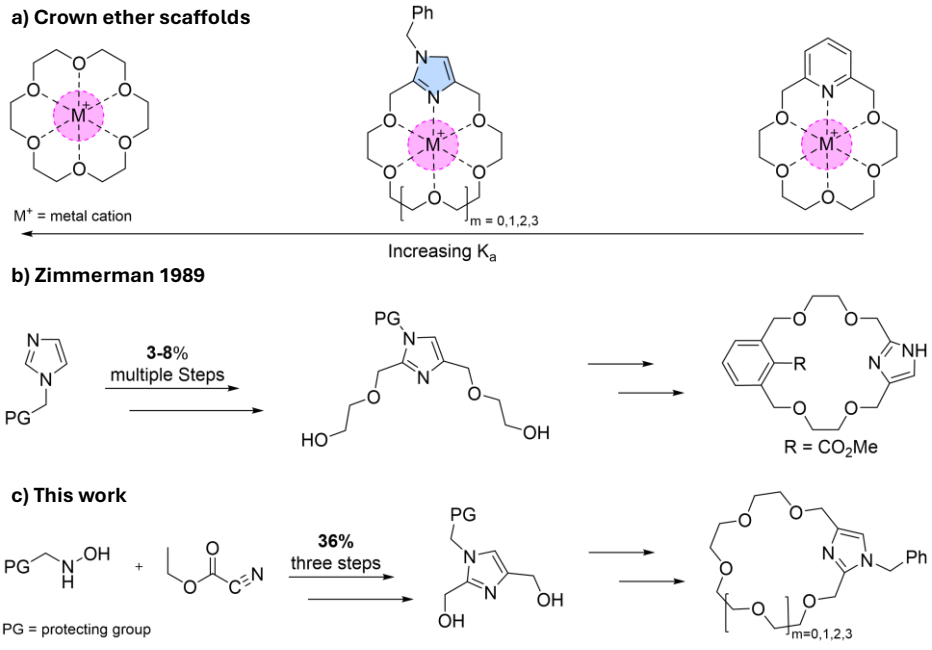

Table of Contents

1 Project Motivation 1

2 Introduction 1

2.1 Crown Ether History 2

2.2 Crown Ether Synthesis 4

2.3 Crown Ether Binding Supramolecular Interactions 8

2.4 Crown Ether Derivatives 11

2.5 N-heteroaromatic Containing Crown Ethers 14

2.6 Imidazole Crown Ethers 15

2.7 Reported Imidazole containing "crown ethers" 17

2.7.1 Zimmerman Syntheses 18

3 Objectives 20

4 Results and Discussion 21

4.1 Retrosynthesis 21

4.2 Synthesis 22

4.2.1 Synthesis of Imidazole diol intermediate **3** 22

4.2.2 Imidazole Macrocycle Cyclization 24

4.2.3 Deprotection of the Imidazole Macrocycles 26

4.3 Study of alkali metal binding by the imidazole crown ethers. 28

4.3.1 NMR titrations 28

4.3.2 Imidazole Macrocycle Crystal Structure 32

4.3.3 Reporting K_a from Titration Experiments 34

4.3.4 K_a of Imidazole Macrocycles with K^+ and Na^+ 38

4.4 Imidazole Macrocycles for Pseudorotaxanes. 40

5 Conclusion 45

6 Perspectives 47

References 49

Supporting Information 55

General Information 55

Synthesis 56

Synthesis of (Z)-1-amino-N-benzyl-2-ethoxy-2-oxoethan-1-imine oxide **(1)** 56

Synthesis of 2-ethyl 4-methyl 1-benzyl-1H-imidazole-2,4-dicarboxylate **(2)** 56

Synthesis of (1-benzyl-1H-imidazole-2,4-diyl)dimethanol **(3)** 57

Synthesis of 1-benzyl-2,4-bis(chloromethyl)-1H-imidazol-3-ium **(4)** 57

Cyclization General Procedure A 58

Titrations 61

NMR titrations SI 62

Pseudorotaxane formation 86

X-Ray Crystallography Data 92

Computational Details 94

^{1}H and ^{13}C characterization data 96

Supporting Information References 103

Abbreviations

Å	Angtrom
12C4	12-crown-4
15C5	15-crown-5
18C6	18-crown-6
21C7	21-crown-7
24C8	24-crown-8
Bindfit	Online fitting tool for supramolecular binding data.
DB24C8	Dibenzo-24-crown-8
DB27C9	Dibenzo-27-crown-9
DB30C10	Dibenzo-30-crown-10
DBA.HPF$_6$⊂ImBn24C8	Dibenzyl ammonium and ImBn-24-crown-8 pseudorotaxane
DBA.HPF$_6$⊂Py24C8	Dibenzyl ammonium and Py-24-crown-8 pseudorotaxane
DBA.HPF$_6$⊂DB24C8	Dibenzyl ammonium and DB-24-crown-8 pseudorotaxane
DFT	Density Functional Theory
DIPEA	N,N-diisopropylethylamine
$\Delta\delta_{HG}$	Total chemical shift due to host-guest complexation
$\Delta\delta$	Observed change in chemical shift
ΔY	Observed physical change
δ_{obs}	Observed chemical shift
ESI	Electrospray Ionization
Et$_3$N	Triethylamine
EtOAc	Ethyl acetate
EXSY	Exchange spectroscopy
G	Guest
[G]	Free guest concentration
[G]$_0$	Initial guest concentration
H$_2$SO$_4$	Sulfuric acid
H-bond	Hydrogen bond
HCl	Hydrochloric acid
[HG]	Host-guest complex concentration
HRMS	High Resolution Mass Spectrometry
HSAB	Hard Soft Acid Base
Hz	Hertz
ImBn15C5	(Z)-benzyl-11H-3,6,9,12-tetraoxa-1(2,4)-imidazolacyclotridecaphane
ImBn18C6	(Z)-benzyl-11H-3,6,9,12,15-pentaoxa-1(2,4)-imidazolacyclohexadecaphane
ImBn21C7	(Z)-benzyl-11H-3,6,9,12,15,18-hexaoxa-1(2,4)-imidazolacyclononadecaphane
ImBn24C8	(Z)-benzyl-11H-3,6,9,12,15,18,21-heptaoxa-1(2,4)-imidazolacyclodocosaphane
J	Coupling constant
K$_a$	Association constant
KPF$_6$	Potassium hexafluorophosphate
K$^+$	Potassium ion

LG	Leaving Group
m/z	Mass-to-charge ratio
MeCN	Acetonitrile
MeOH	Methanol
MIMs	Mechanically Interlocked Molecules
mM	Millimolar
M^{-1}	Per molar
NaH	Sodium hydride
$NaPF_6$	Sodium hexafluorophosphate
Na^+	Sodium ion
NMR	Nuclear Magnetic Resonance
NOESY	Nucelear Overhauser Effect Spectroscopy
Nu	Nucleophile
PF_6^-	Hexafluorophosphate anion
pH	Potential of hydrogen
ppm	Parts per million
Py18C6	Pyridine-18-crown-6
Py24C8	Pyridine-24-crown-8
qNMR	Quantitative Nuclear Magnetic Resonance
Rf	Retention factor
SD	Standard Deviation
$SOCl_2$	Thionyl chloride
THF	Tetrahydrofuran
uc	Uncomplexed species
UV-Vis	Ultraviolet-visible spectroscopy
% wt	Percent weight

1 Project Motivation

This project originated from the need to access an imidazole-containing crown ether for a separate project within the group, where it served as the macrocycle component in a rotaxane scaffold. The target macrocycle needed to be a classical crown ether scaffold but with the incorporation of an imidazole replacing a singular CH_2OCH_2 unit. However, the literature methods for the synthesis of an imidazole containing crown ether are long and inefficient. This prompted us to investigate a novel synthetic route to access imidazole crown ethers more directly and reliably. This work introduces a novel imidazole crown ether synthesis and studies the effect of the imidazole on the cation binding properties. Also extending this towards secondary ammonium ions to validate their future use for rotaxane synthesis.

2 Introduction

Crown ethers are cyclic compounds with a cavity lined by repeating ether donor atoms within a flexible framework (Figure 1). This flexible framework creates a high degree of conformational freedom, allowing interconversion between various conformations at low energy barriers.[1] The arrangement of oxygen heteroatoms facilitates coordination to positively charged guests. Together, conformational flexibility and the organization of donor atoms allow crown ethers to form stable complexes with cations.[2] This ability to accommodate guests within the macrocyclic cavity is central to the host-guest chemistry of crown ethers.[3]

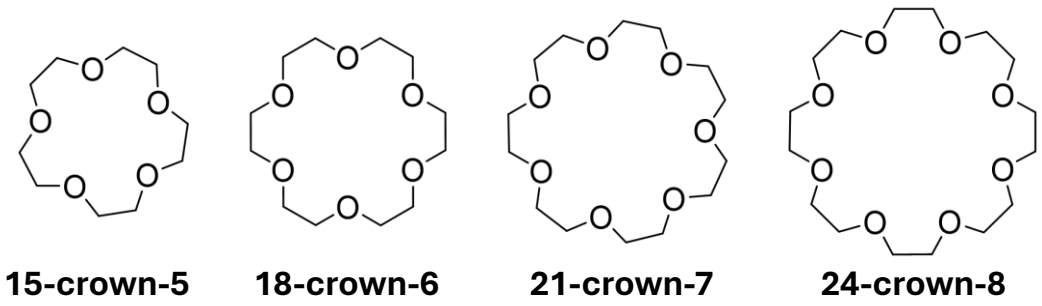

Figure 1. Classical crown ether structures.

The ability for crown ethers to coordinate is the main property of interest, leading to interesting applications. For instance, coordination to cations can enhance lipophilicity increasing solubility of inorganic salts in non-polar media.[4] This property is often used in phase-transfer catalysis, which uses the solubilizing power of crown ethers to allow ionic reactions to occur in aprotic media.[5] However, crown ether coordination is not limited to metal cations; crown ethers are also capable of complexing positively charged organic substrates in aprotic solvents. Therefore, through the coordination of crown ethers with

a variety of organic guests, large and complex supramolecular systems can be designed. This coordination is often used to thread various molecules through the cavity, creating mechanically interlocked molecules. Consequently, crown ethers are often important components in rotaxanes, catenanes, and molecular machines.[6] These examples represent only a small subset of crown ether applications. Others include selective ion recognition and sensing[7], metal ion extraction[8], ion transport processes and functional materials.[9] This versatility arises from their tunable binding properties and structural adaptability.

The discovery of crown ethers and their properties is an important milestone in the development of supramolecular chemistry, as these compounds were among the first molecular systems that exhibited supramolecular behaviour.[1] Crown ether research began with the synthesis of simple crown ether scaffolds, focusing more on metal complexations studies. However, current research mostly explores methods for their application in diverse fields. Often their applicability in fundamental and applied chemistry is heavily dependent on modification of donor atoms, ring size, or ancillary groups. These modifications can lead to enhanced selectivity, new functional responses, and changes to the binding affinity.[4] This introduction first outlines the history of crown ethers, before discussing different synthetic approaches, binding behaviour and finally developing structurally diverse crown ethers.

2.1 Crown Ether History

Crown ethers were accidentally discovered in 1967 by Charles Pedersen. He was investigating coordination chemistry and was attempting to synthesize multidentate phenolic ligands to explore their effects on the vanadyl group (VO^{2+}). While performing a reaction to synthesize the ligands, he observed unexpected behaviour of an isolated byproduct, which prompted him to explore it further. The synthetic scheme attempted by Charles Pedersen to synthesize the desired ligand is depicted in Figure 2.

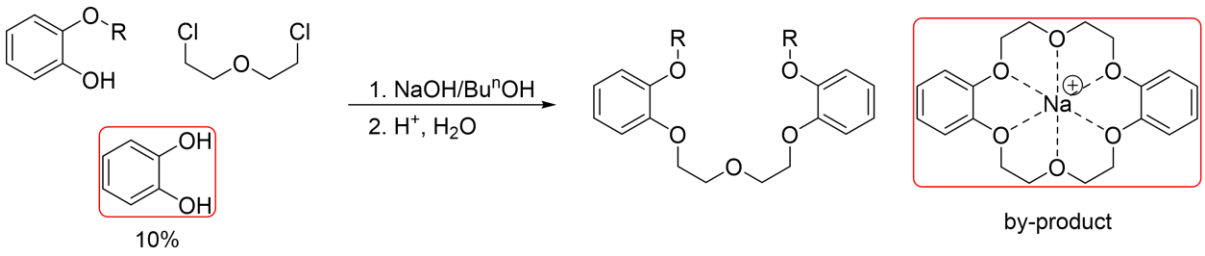

Figure 2. First synthetic scheme for the first macrocycle by Charles Pedersen.[10]

The catechol starting material contained approximately 10% of the mono-unprotected catechol impurity. Knowingly, the synthesis was executed as purification was planned following the reaction. The crude mixture was described as an “unattractive goo”, upon

purification only 0.4% of a white crystalline compound was isolated. Given the unexpectedly low yield of such a classical reaction, it was presumed to not be the desired uncyclized multidentate ligand.[10]

This unexpected result prompted the exploration of the by-product for the reaction. The reaction was then checked by UV-Vis spectroscopy; it is known that this phenol and their ethers absorb at 275 nm with a distinct absorption pattern (Figure 3a). In the presence of an alkaline metal the absorption pattern does not change but rather exhibits batochromic shift given free hydroxyl groups, this is shown as the dashed line in Figure 3a. The unknown compound was dissolved in methanol where it was only partially soluble, and a spectrum was run (Figure 3b). The obtained spectrum was characteristic of a phenolic compound containing a free hydroxyl group (Figure 3b). However, upon treatment with sodium hydroxide a new spectral pattern was obtained (Figure 3b), which was unexpected from previous observations.

Furthermore, it was observed that when sodium hydroxide was added to solution the compound became more soluble in methanol. To further confirm the solubility change was not a consequence of alkalinity, but due to sodium ions, various non-basic methanol soluble salts were introduced in solution with the unknown compound. This rendered the unknown compound soluble in methanol. These preliminary tests confirmed the presence of a new species and the synergistic behaviour with cations.[10]

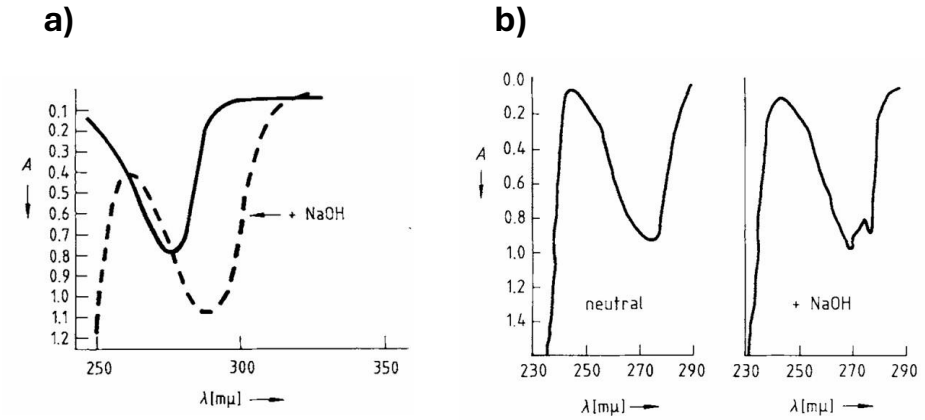

Figure 3. a) Expected absorption spectra of the uncyclized product b) novel experimental absorption of the first crown ether adapted from literature.[7]

From here further testing was performed to elucidate the structure of the impurity and its binding capabilities to cations. These tests included elemental analysis, molecular modelling and obtaining a crystal structure. Isolating the crystals and performing x-ray diffraction showed the 3D representation with the cation in a cavity with the repeating crown ether functionalities ordered in a cyclic manner. This was the first example of a stable neutral complex formed with alkali metals, and the first example of a crown ether.[2]

Pedersen further explored these macrocyclic crown ether structures, due to the unique properties exhibited by these crown ethers. The nomenclature of crown ethers is

introduced by Pedersen because the IUPAC names become very complicated, using the epithet “crown” to name of these compounds due to the molecular model resembling a crown.[10] Values on either side of the term “crown” are used to describe the cyclic moiety of the compounds. The first value denotes the total number of atoms and the second the number of heteroatoms within the cyclic part of the of the compound. Given a more diverse crown ether, the substitution is named first, then the description of the cyclic part *i.e.* dibenzo [18] crown-6-ether for the one shown in Figure 2.[10]

Finally, Pedersen wanted to explore how the synthetic scheme worked. Upon reproducing the reaction with the correct equivalences for the desired crown ether product. A 45% yield of the dibenzo [18] crown-6-ether was achieved without high dilution. Macrocyclization is a cyclization reaction where a ring closure leads to a ring of 12 atoms or more. This reaction is unfavourable due to entropic penalties, where the functional groups need to react over a large surface area, therefore smaller cyclization reactions occur more readily. Consequently, Pedersen proposed that the macrocyclization ring closure step was facilitated via a sodium cation through templation. These cations were introduced into the reaction as an ion pair for the base of the reaction. Applying this knowledge, Pedersen was able to synthesize 60 different macrocyclic polyethers. Creating a wide variety of polyethers with ring sizes ranging from 12 to 60 atoms and incorporating different substituents within the scaffold such as heteroatoms sulfur and nitrogen.

While studying the newly synthesized crown ethers Pedersen was able to formulate various conclusions on their properties. Finding that the most effective complexing crown ethers were ones that contained 5 to 10 oxygens within the ring.[10] Also noting the drastic increase in solubility due to ion complexation was consistent for the diverse crown ether structures.[11]

All this groundbreaking work by Charles Pedersen culminated in him sharing the Nobel Prize in 1987, demonstrating the importance of crown ethers. The synthetic work by Charles Pedersen and contributed by others enabled the development of various synthetic methods towards crown ethers.

2.2 Crown Ether Synthesis

Charles Pedersen introduced six synthetic methods for crown ethers and their derivatives. These are not six unrelated reactions: each employ subtle differences in connectivity and post synthetic modifications for a different cyclization step. Interestingly, these synthetic methods have not changed much since Pedersen initially reported them.[12] All the synthetic methods use Williamson ether synthesis.[13] This is a reaction that occurs via an S_N2 where an alkoxide ion acts as a nucleophile, to displace a good leaving group (LG) such as a halide or tosylate. Resulting in the formation of an unsymmetrical ether (Figure 4). The competing elimination reaction may limit the yield or applicability of a Williamson ether synthesis with some substrates.[14]

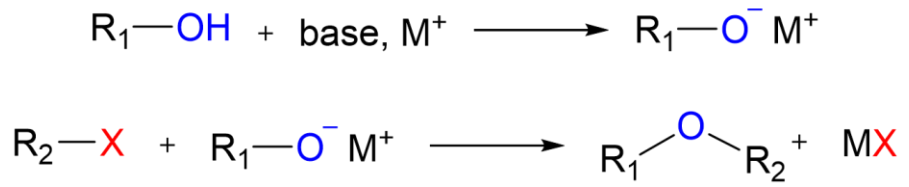

Figure 4. General reaction scheme for a Williamson ether synthesis.

Most of the synthetic methods for crown ethers and derivatives reported by Pedersen uses polyether diols and dihalo linkers as the building blocks. All methods follow the design principle that the nucleophile containing fragment introduces the flexible repeating ether functionalities controlling the cavity geometry. Whereas the electrophilic fragment acts as a divalent spacer which is more tunable to facilitate macrocyclization. Pedersen also uses a base containing a templating cation to form the alkoxides which facilitates the Williamson ether synthesis. Figure 5 and Figure 6 represents the synthetic routes proposed by Pedersen, where A represents any divalent organic group, due to the tunability of the spacer group.[13]

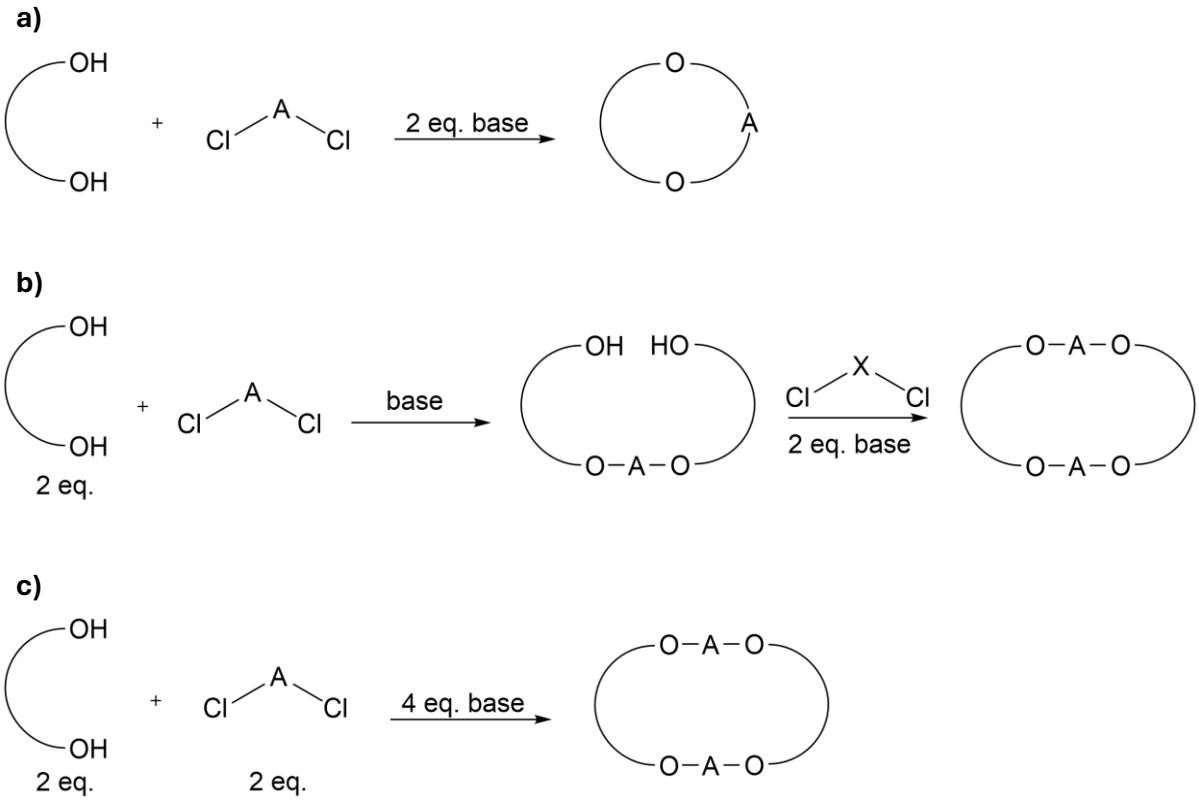

Figure 5. Methods a-c) for the synthesis of crown ethers as reported by Pedersen. Where A is any divalent organic group.[11]

One of the simpler schemes is method a) (see Figure 5) where the larger fragment that contains the diol will attack both ends of a smaller dihalide linker closing the ring. Pedersen reported that this method is preferential for the formation of monobenzo crown ethers. Next, the stepwise route b) was reported, where two equivalences of a long chain diol react with a dihalide linker. This leads to two separate diol molecules adding onto

either side of the dihalide linker, giving an acyclic precursor. Then, other equivalences of the dihalide linker are added in the presence of a base to facilitate the cyclization of the macrocycle. Method c) demonstrates the one pot assembly version of method b). In this method, two equivalents of the diol react with two equivalents of the dihalide linker, leading to macrocyclization in which all four components are incorporated into the macrocyclic framework. Due to the lack of preformation, this approach can lead to decreased selectivity and the possibility for side products, which is reflected in the low yields compared to other methods.[13] Method b) was particularly useful for crown ethers with two or more benzo groups. This is demonstrated by Pederson achieving 80% yield using method b) and 45% yield using method c) to synthesize a dibenzocrown ether.[15]

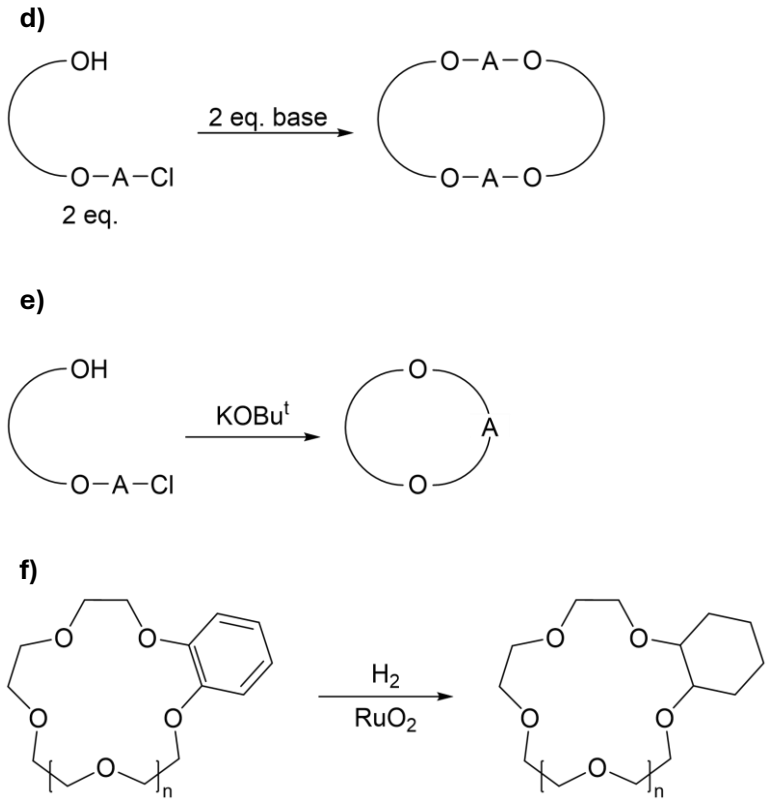

Figure 6. Methods d-f) for the synthesis of crown ethers as reported by Pedersen. Where A is any divalent organic group. [11]

A cyclodimerization is shown in method d) (see Figure 6), where the starting molecule contains both a halide and the diol functionalities. Consequently, using two equivalents of the compound in the presence of a base, should allow two of the same substrates to react with one another to form the resulting macrocyclic product. Method e) is more specialized involving a preformed hydroxy-halo polyether that undergoes an intramolecular reaction allowing the cyclization to occur. Method d) and e) differ from other methods, as the cyclization occurs via one singular substrate. This is advantageous as it eliminates the need for the synthesis and design of a secondary reactant. However, Pedersen also reports lower yields when using method d) and e).[13] The final method f) described by Pedersen is distinct from the other methods as it involves post-synthetic

modification. For instance, the possibility of the hydrogenation of the benzene ring with ruthenium catalyst. Here the crown ether is already formed, and the benzene is reduced to a cyclohexane. This is important because saturated crown ethers have more basic oxygens allowing better complexation.[13]

2.2.1 Dilution for Cyclization

Each method described employs two important key strategies to favour cyclization over the formation of polymeric side products. The first method is to use high-dilution conditions during the reaction, as developed by Ruggli *et al.* in 1912.[16] This is the notion that high dilution conditions favour the intramolecular reaction and therefore cyclization. The theoretical analysis and the experimental set-up of high dilution was extensively described by Ziegler *et al.* who observed that the tendency for cyclization of medium to large rings was low.[17] This was a result of entropic penalties and the possibility of a reaction towards oligomeric chains. The use of dilute conditions however, increases the likelihood of cyclization, which can be explained through kinetics.[18]

$$r = k[Nu^{2-}][RX_2] \quad (1)$$

$$r_{intra} = k_1[Nu^{-}RX] \quad (2)$$

$$r_{inter} = k_2[Nu^{-}RX]^2 \quad (3)$$

The Williamson ether synthesis follows an S_N2 mechanism indicative of 2nd order kinetics. This is due to the nucleophile (Nu^{2-}) reacting with a separate electrophilic substrate (RX_2) in the rate limiting step as show in eq. (1).

However, macrocyclization occurs through two consecutive Williamson reactions, the initial addition followed by the ring closure. The initial substitution follows classical 2nd order kinetics eq (1), here *r* is the reaction rate, k is the rate constant, Nu^{2-} is the concentration of the nucleophile and RX_2 is the concentration of the electrophilic dihalide. The first substitution is the same for the inter and intramolecular product. However, the second substitution will determine the final product.

If the second substitution occurs intramolecularly it follows first order kinetics eq. (2), due to one species reacting with itself. Therefore, the reaction rate is only dependent on the concentration of one species, making the intramolecular reaction favoured at dilute conditions. For the intermolecular/polymerization reaction a second species needs to insert itself into the mechanism. This adds another variable making the reaction rate proportional to the square of the concentration eq. (3).[18]

$$\frac{r_{intra}}{r_{inter}} = \frac{k_1}{k_2[Nuc^{-}RX]} \quad (4)$$

Eq. 4 further demonstrates this relationship, showing that when $[Nu^{-}RX]$ is decreased, the rate of the intramolecular reaction increases ($r_{intra} > r_{inter}$). If the rate is higher for

the intramolecular reaction and therefore the macrocyclization, the product will not react further. This demonstrates that dilute conditions increases intramolecular reaction probability, forming crown ethers at better yields. What is described in this section is known as the Ruggli-Ziegler dilution principle.[19]

2.2.2 Template Effect

The other condition used during the synthesis of crown ethers is the template effect. This is a phenomenon where a molecule or molecular framework acts as a structural guide that directs or facilitates the formation of a specific product. The templation is directed by non-covalent interactions and is not covalently incorporated in the final product. For macrocyclization reactions the template effect is often mediated by a metal cation such as Na^+. It will organize the acyclic precursor into a cyclic conformation, arranging the cyclization reactive sites in proximity as shown in Figure 7. There are two important effects the templation has on the system: i) the kinetic effect, and ii) the thermodynamic effect.[20]

i) The kinetic template effect induces the organization of the reactive sites, allowing the cyclization reaction to occur faster. Essentially, lowering the kinetic barrier for ring closure and increasing the effective molarity by preorganizing reacting ends.

ii) The thermodynamic template effect occurs for systems in equilibrium when the template stabilizes the cyclic product, making the cyclization more thermodynamically favourable. As a result, the macrocycle-template complex is lower in free energy, shifting the thermodynamic balance towards macrocycle formation.[21]

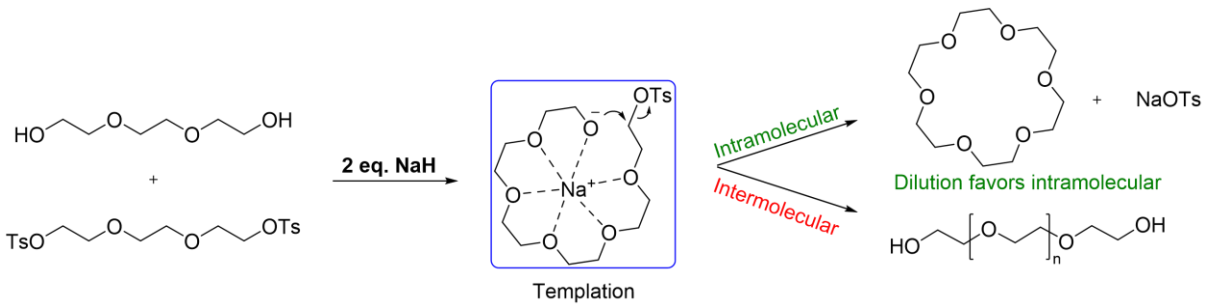

Figure 7. Templating effect and the inter vs intramolecular competition during macrocyclization reactions.

2.3 Crown Ether Binding Supramolecular Interactions

The main property of interest of crown ethers is their ability to bind cations through the designed cavity. This binding can be described as a dynamic equilibrium defined by the association constant (K_a). For a 1:1 system, this can be represented as the ratio of the complex to the free species in solution as shown in eq. (5) and in Figure 9.

$$K_a = \frac{[complex]}{[crown][cation]} \quad (5)$$

Therefore, a higher K_a would be indicative of stronger binding.[20] This dynamic process of ion-crown ether association depends on several factors such as the properties of the ligand, solvent, and the interacting ion. The energies required to form the crown ether-ion complex can be demonstrated by a Born-Haber cycle, where X^- is the anion, M^+ is the cation and C is the crown ether (Figure 8).[2]

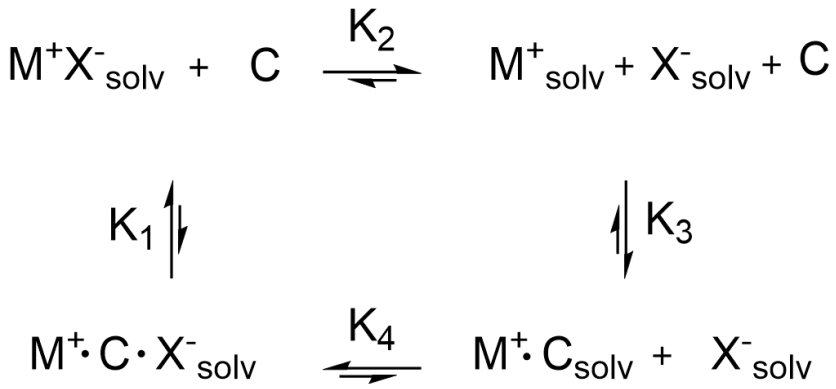

Figure 8. Born Haber cycle for crown ether cation binding. [2]

The Born-Haber cycle in Figure 8 shows that complexation is not solely due to attractive forces, it is rather due to a balance of energetic contributions including host-guest association but also solvation, and desolvation. In polar solvents the equilibrium that corresponding to K_2 is favoured, due to the strong solvation of the cation and anion. Polar solvents induce strong solvation because they form stabilizing ion-dipole interactions with the anion and cation separately. This makes desolvation for complexation energetically costly and therefore reducing complex formation. The opposite is true in apolar solvents where the weaker solvation reduces this penalty, shifting the equilibrium towards complexation ($M^+ \cdot C \cdot X^-_{solv}$), such that K_4 predominates.[2] Globally this shows that the energy gained from the host-guest interaction must compensate for the energy required to remove solvent molecules, allowing binding to be thermodynamically favourable. Taken together, this demonstrates the important role solvents play in host-guest chemistry.[22]

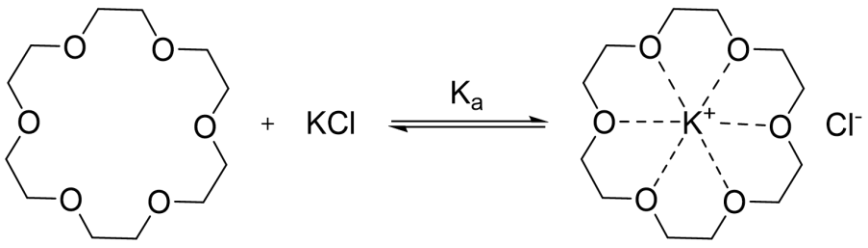

Figure 9. Classical crown ether-cation binding mechanism.

Having established the thermodynamic framework needed for binding to occur, it is also important to consider the specific interactions responsible for stabilizing the crown ether-cation complex. This stabilization stems from the coordination of the cation in the

crown ether cavity through non-covalent interactions such as ion-dipole, hydrogen bonding (H-bonding) and other electrostatic interactions.

An ion-dipole interaction is one between a full charge and a partial one. Bond energies for ion-dipole interactions range from 10 to 50 kJ mol^{-1}, depending on the dipole moment, media, ion charge, and the distance.[23] In crown ether complexes this ion-dipole interaction occurs via the oriented lone pairs of the oxygen (dipole) and the cationic guest (ion). For guests which are protonated cations, such as a secondary ammonium, H-bonds are one of the main driving forces for the stabilization. An H-bond is the attraction between a proton donor (X-H) and an acceptor (Y), where the proton seeks to bind to the electron rich region of the acceptor often at the lone pair. It has typical interaction strengths between 0-40 kJ mol^{-1}.[24] There are also other non-covalent interactions such as van der Waals or π-stacking, however they are much weaker and are less consequential in cation coordination.

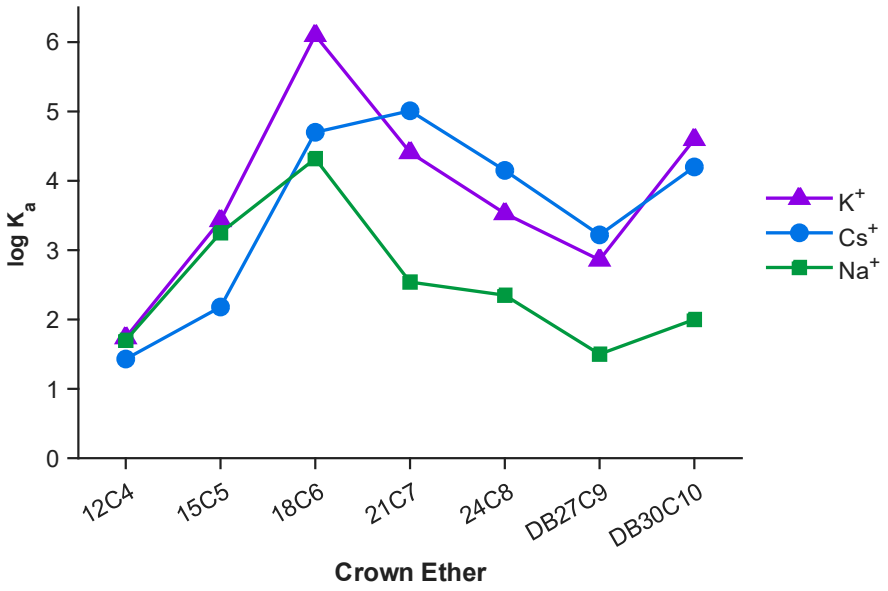

Figure 10. Comparison of literature values for the association constant K_a of crown ethers with different ring sizes with alkali metals of different ionic radii in MeOH at 25°C.[2] DB denotes dibenzo substituted crown ethers.

The affinity for the guest is dependent on a multitude of factors, one of them is the relative size complementarity of the crown ether host and the cationic guest. This refers to the close match between the ionic radius of the cation and the cavity of the crown ether. This is sometimes referred to as the size fit model. The close match should allow for the cation to insert itself nicely within the crown ether cavity giving optimal contact distances and angles between all donor atoms and distorting the crown ether less. This shows that when size complementarity is matched a more stable complex forms giving a high K_a. However, this is not always the case as there are other factors that can play a bigger role in defining host-guest stabilization and therefore the K_a.[25] These factors include the number and location of the oxygen atoms, steric hindrance on the cavity, charge density of the guest, and the solvent effects. This is demonstrated on Figure 10 where the

macrocycle with cavity of 30 atoms forms the most stable complex with K^+ but has the best size complementarity to Cs^+. Consequently, the size fit model is not a universal rule rather a simplified but important predictor for possible affinity of the host and guest.[2]

For small alkali and alkaline earth cations, the size fit model is less predictive as their affinity is strongly influenced by their solvation, and less by size complementarity. This is because small cations have a high charge density and therefore are very strongly solvated. Consequently, there is a large desolvation penalty to form host-guest interactions for these species, influencing the magnitude of the interaction. Notably, K^+ is less strongly solvated than Na^+ or Li^+, meaning breaking solvent-ion interactions has a smaller energetic cost for K^+ allowing more stable complexation. Therefore, K^+ often exhibits higher affinity for most oxygen-containing macrocycles.[26] This is also demonstrated in Figure 10 where K^+ consistently has higher affinity than Na^+. If the solvation energies are similar, then the size-fit model can be more representative of the affinity.

Varying the donor groups can also lead to changes in the affinity for specific guests. For instance, replacing an oxygen heteroatom with a nitrogen usually leads to a decrease in affinity for alkali and alkaline earth cations. This is due to the oxygen being a harder donor. Whereas the softer donation of nitrogen can increase the affinity for transition metals consistent with hard soft acid base (HSAB) theory. Finally, the substitution of the crown ether can affect binding, due to changes in electronic and geometric properties. Leading to increased rigidity and a decrease in flexibility for a more selectivity crown ether-guest interaction.[27]

2.4 Crown Ether Derivatives

Modification of the classical crown ether structure has been of interest because it can lead to changes in the properties of crown ethers including selectivity, conformation and binding interactions. Some of these modifications include the incorporation of new substituents within the macrocyclic framework such as heterocycles, aromatic units or introducing side chains via direct functionalization.

2.4.1 Lariat crown ethers

Lariat crown ethers are derivates that contain a side arm, which can introduce a secondary binding site. In 1978 Okahara and co-workers created a novel crown ether scaffold incorporating a flexible side arm with a donor group (Figure 11a).[28] The side arm ties up the cation vertically while the crown ether cavity lassos it horizontally.[29]

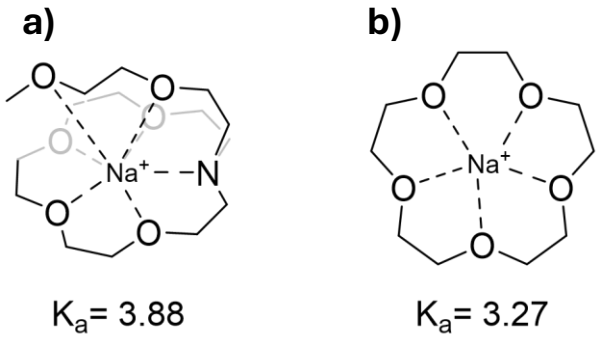

Figure 11. The association constant (log(K_a)) a) for a lariat crown ether and Na^+ taken from literature.[28] b) A classical crown ether complexing Na^+ and the logK_a value taken from literature.[2]

The introduction of a new donor atom on the side arm leads to a basketlike coordination and can lead to stronger binding, adopting a similar 3D structure to a cryptand. The side arm can be further tuned to introduce selectivity via guest size, or charge density. This side arm is not limited to classical donor atoms it can also introduce groups which are capable of membrane insertion, hydrogen bonding, and cation-π interactions.[30] These properties are used in applications in modelling cation-π interactions, membrane transport and as secondary interaction sites for rotaxanes and pseudorotaxanes.[31]

2.4.2 Benzo crown ethers

The first synthesized crown ether was a dibenzo crown ether, as represented in Figure 2. However, Pedersen reported that they bind cationic guests less favourably compared to classical unsubstituted crown ethers shown in Figure 1.[11] This same pattern was observed with other crown ethers where an aromatic substituent was introduced into the scaffold (Figure 12).[32]

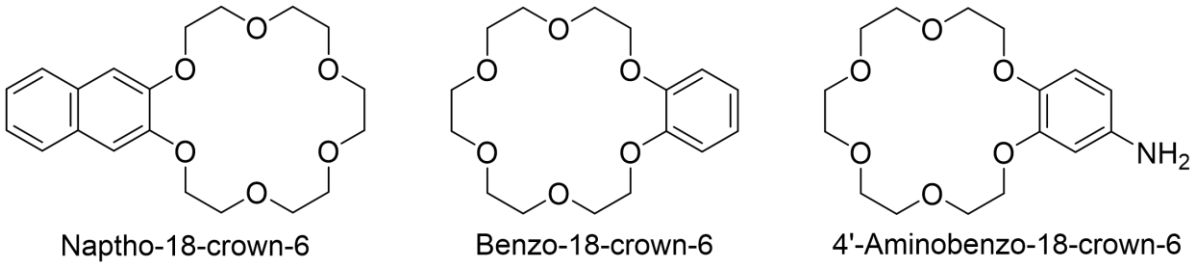

Figure 12. Diverse benzo substituted crown ethers, with similar binding properties attributed to the substitution.

There are a few reasons for the observed poorer binding of benzo substituted crown ethers. They create a more rigid cyclic scaffold due to the introduction of sp^2 carbons within the cavity, making them less conformationally adaptable to accommodate a guest. Furthermore, the electron withdrawing nature of the substituents decreases the oxygen basicity, decreasing the binding.[33] However, there are also potentially beneficial changes, such as the increased chemical stability and lipophilicity in comparison to aliphatic crown ethers. Finally, the π- π interactions that occur between the substituents and the rigidity is a property that can be used in larger supramolecular assemblies such

as rotaxanes and pseudo rotaxanes.[34] This demonstrates that a subtle change can lead to differences in binding properties and therefore applications.

2.4.3 Crown ethers for mechanically interlocked molecules

Crown ethers are an important structural motif for mechanically interlocked molecules (MIMs) such as rotaxanes and pseudorotaxanes. MIMs are a class of molecules where discrete molecular units are linked together by mechanical bonds. This means separation of each unit is not possible unless a covalent bond is broken due to mechanical interlocking. Some classical examples of MIMs are rotaxanes, and catenanes. Mechanical bonding is important because while each subunit remains associated together, there remains free dynamic motion, allowing the substituents to undergo controlled motions such as shuttling, rotation, and translation, without disassociating from one another.[35] These MIMs are often used to construct molecular machines which have a variety of applications.[36]

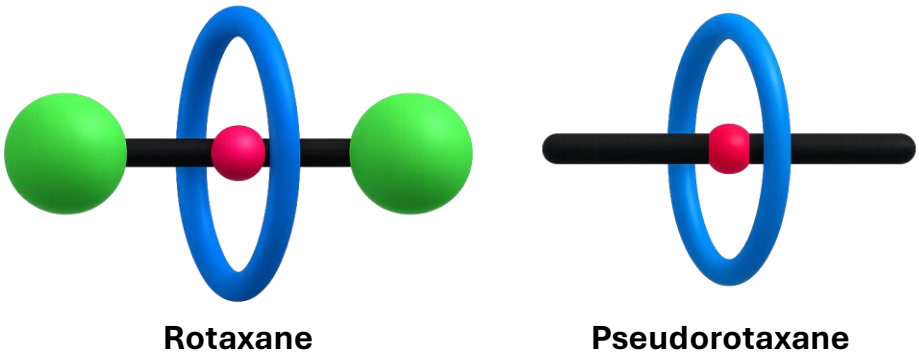

Figure 13. Schematic structure of a pseudorotaxane and rotaxane.

Crown ethers are used extensively for synthesizing rotaxane, and pseudorotaxane like structures (Figure 13). The first reported synthesis of rotaxanes can be traced back to 1967 as reported by Harrison *et al.*[37] A rotaxane consists of a linear axle threaded through the cavity of a macrocycle, with two bulky stoppers at each end of the axle. The stoppers inhibit the dissociation of each component.[38] This is the basic structural scaffold for a rotaxane however, more complex rotaxanes have been constructed with multiple macrocycles or axles.[38] A pseudorotaxane which translates to a “false” rotaxane, has the same structure without the bulky groups. The axle of a pseudorotaxane is held in place of the cavity by non-covalent interactions. Therefore, it is a structure between a classical supramolecular one and a MIMs.[35] Applications for these structures include molecular devices[45] such as logic gates[41] or sensors[42], in molecular machines such as nanomotors or elevators to name a few.[43]

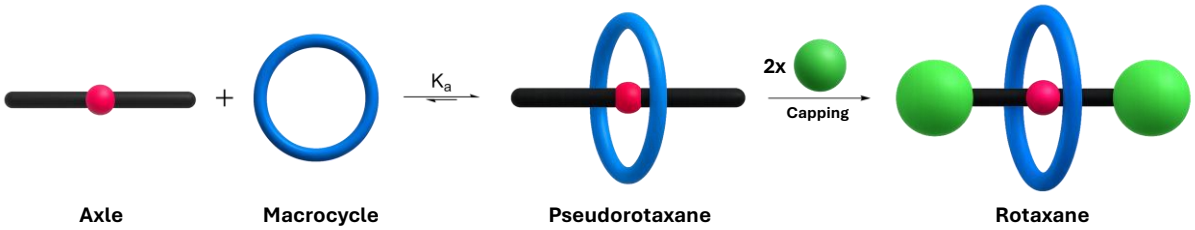

Figure 14. Capping strategy for rotaxane formation via the pseudorotaxane intermediate.

The reason crown ethers are used in these systems is their capacity to interact with positively charged moieties in the axle through H-bonds, ion-dipole, and electrostatic interactions. These interactions favour the threading of the axle through the cavity of crown ethers.[44]

The host-guest binding is an important factor in the synthesis of rotaxanes. A common method for the synthesis is the use of a capping strategy.[45] Capping is where a host-guest interaction is created between the axle and the macrocycle without the stoppers. After this interaction, two bulky groups are covalently attached onto both ends of the axle (Figure 14). Consequently, the higher the association constant for the pseudorotaxane the more it is available for the capping reaction, therefore increasing the yield of the final rotaxane synthesis.[46,47] Crown ethers form strong pseudorotaxanes, and modifications to the scaffold can increase the association, this can be interesting in rotaxane synthesis.[48]

A common method to generate a pseudorotaxane is by utilizing secondary ammonium ions on an axle forming H-bonds with crown ethers. The ammonium ion is incorporated between two linear arms of the axle, then the H-bonding allows the threading of the axle through the large cavity of the crown ether, forming the pseudorotaxane.[49]

The interaction between the crown ether and the axle facilitates synthesis/formation but is also used to create functionality. The crown ether can be shuttled along the axle between different recognition sites, due to external stimuli such as pH, redox, light or temperature. This response can then be harnessed to be used in molecular machines.[50] The different substituents on the crown ether scaffold are important in the responses to external stimuli. For instance, the incorporation of a protonation site, and the modulation of the pH in the medium can lead to changes in crown ether-axle affinity, leading to a molecular response.[51] This, demonstrates a repeating motif where the importance of creating diverse crown ether scaffolds is highlighted.

2.5 N-heteroaromatic Containing Crown Ethers

An interesting example of modified crown ethers is the inclusion of N-heteroaromatic units within the cavity. In these structures a nitrogen-containing heteroaromatic is introduced replacing one or multiple ether functionalities. There are numerous examples

of crown ethers containing N-heteroaromatic groups such as pyridines, pyroles, pyrimidines and triazoles.[52–57]

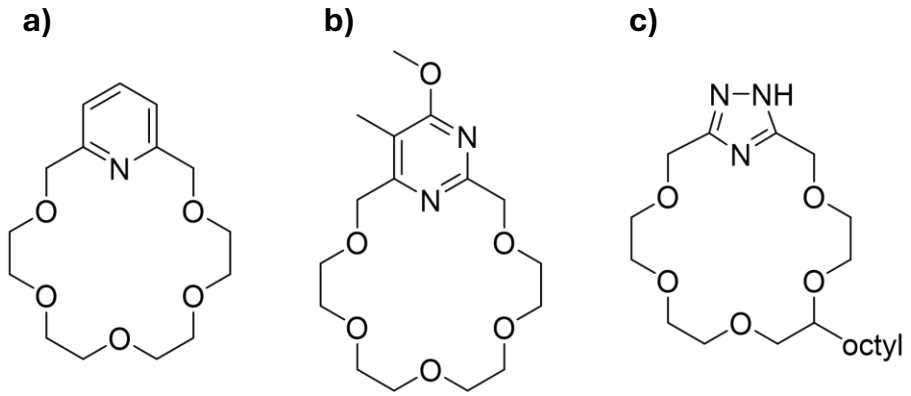

Figure 15. Different N-heteroaromatic containing crown ethers a) pyridine[54] b) pyrimidine[51] c) triazole[53].

The incorporation of an N-heteroaromatic introduces structural changes to the cavity and novel electronic features. The biggest addition to the crown ether cavity is the introduction of a nitrogen donor site which creates a different donor environment. Nitrogen donors are more polarizable and less hard than oxygen, meaning they may be better suited for transition metal coordination. Also, the nitrogen donor is more directional, as they have better spatial orientation of the donor site. This creates a more defined and geometrically constrained binding, giving greater control over binding orientation.[58]

Similarly to dibenzo crown ethers, the aromatic nature of the N-heteroaromatics introduces sp^2 hybridized carbons which increases rigidity of the crown ether framework. This rigidity was observed by Li *et al* reporting that the triazole substituted crown ether provides a more trigonal recognition site for RNH_3^+ groups (Figure 15c).[55]

Furthermore, these N-heteroaromatics also introduce the possibility to behave as strong H-bond donors or acceptors depending on the heterocycle. Notably this was observed by Staveren *et al*. when exploring the binding of the pyridine based crown ether (Figure 15a).[56] They reported a much higher K_a for the pyridine crown ether with protonated cations compared to classical crown ethers. The numerous reports for the synthesis N-heteroaromatic crown ethers, shows their applicability and importance in host-guest chemistry.

2.6 Imidazole Crown Ethers

Despite the variety of N-heterocycle containing structures described, imidazole containing crown ethers are rare. This is odd, given the possible advantages that imidazoles can offer. Notably, an imidazole spacer adds extra elements to the crown

ethers such as pH responsiveness, a H-bond acceptor/donor ability, tautomerization and basicity.

Depending on the tautomeric form, imidazoles can have different supramolecular interactions with the guest. An imidazole in its neutral form contains both a N-H hydrogen bond donor and a pyridine-like nitrogen. The pyridine like nitrogen contains an available lone pair that can act as a hydrogen bond acceptor or a metal coordination site. However, tautomerisation switches the interaction exhibited by the nitrogens via a proton transfer, altering which interaction is directed towards the cavity (Figure 16). This switch can occur spontaneously depending on the guest that is being coordinated and the interaction it prefers. This allows the host to adapt its binding to the guest, potentially allowing binding of either cations or anions.[59]

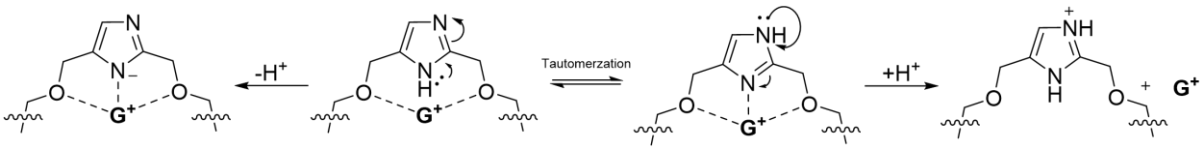

Figure 16. Imidazole tautomerization mechanism.

Imidazole is also pH responsive meaning it can be protonated and deprotonated at mild conditions. This suggests that at one pH it can bind the guest effectively and at another pH the binding is less effective, thereby acting as a molecular switch (Figure 17). Protonation of the imidazole disfavours cation binding by introducing a positive charge within the cavity. This creates a repulsion between the cationic guest and the macrocycle, and changes the donors, electronics, and conformation, leading to reduced association. Finally, an imidazole nitrogen can coordinate stronger and more directionally than oxygen, allowing better coordination to softer cations[60]. This is seen in nature where soft metal coordination often involves imidazole groups.

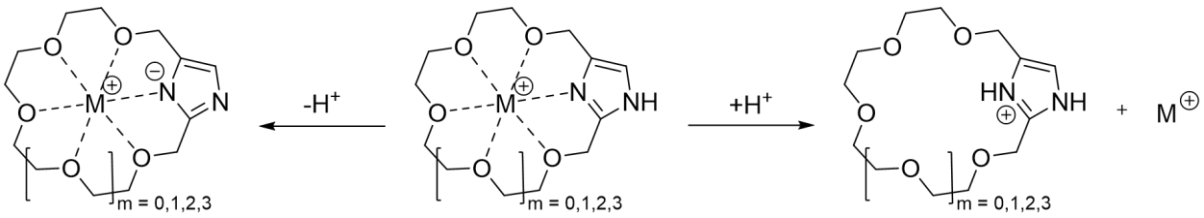

Figure 17. Deprotonation and protonation behaviour and the effect on cation binding.

To date, a true imidazole containing crown ether has not been described, which is a crown ether solely consisting of ether and an imidazole functionality. Current reported imidazole "crown ethers" contain additional aza, amide or benzene units within the macrocycle, deviating away from a true crown ether scaffold. Therefore, there is a gap in the literature towards the synthesis of imidazole crown ethers.

2.7 Reported Imidazole containing "crown ethers"

Only a handful of crown ether structures containing an imidazole have been described, (Figure 18). All of them contain an imidazole substitution and a repeating ether functionality in part of the cycle but also incorporate other functionalities.

Llinas *et al* reported the synthesis of an imidazole crown ether for anion recognition.[61] Their macrocyclic design contains a bis-imidazole unit which provides two N-H groups forming strong hydrogen bonds with anions as seen in Figure 18a. They were able to achieve macrocyclization through the activation of the carboxylic groups using diphenylphosphoryl azide, for the coupling with an amine. Also, the surrounding diamide framework introduces amide N-H donors, giving a macrocycle cavity capable of anion binding. Their systems showed a high association constant ranging from 10^4 to 10^5 for biphosphate or chloride anions.

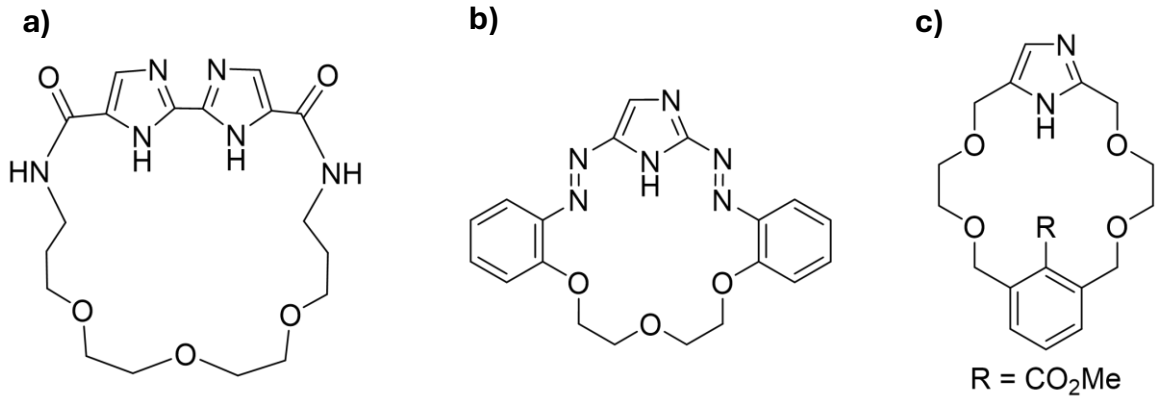

Figure 18. Structures of imidazole crown ether scaffolds reported by a) Llinas et al[61] b) Biernat et a[62] and c) Zimmerman et al.[59,63]

The Biernat group reported an elegant synthesis of chromogenic azole-containing crown ethers, including imidazole-based macrocycles, as shown in Figure 18b.[62] Their objective was to replace the phenolic unit found in previously reported chromogenic crown ethers with an azole residue, such as pyrrole or imidazole. Upon binding to cationic species, the imidazole macrocycles exhibited a strong colour change from red to yellow, maintaining chromogenic properties. In addition the authors showed that the macrocycles could also bind bismuth(III) or Lead(II) ions.[64]

Interestingly, the imidazole derivatives were obtained in synthetically useful yields, with one imidazole macrocycle isolated in 42% yield via reaction of a bis diazonium unit with an imidazole. While synthetically useful, this approach yields highly functionalized aza crown ethers deviating away from classical crown ether properties.[62]

Finally, Zimmerman and co-workers described a crown ether structure more similar to classic crown ethers in an attempt to mimic aspartate and histidine pairs found in numerous enzymes.[63] In this work, a crown ether structure containing both an imidazole

group and a carboxylic acid moiety was targeted (Figure 18c), with the goal investigating how an intramolecular H-bond could influence the imidazole basicity. To this end, their crown ether included not only an imadazole group, but also a benzylic acid spacer. Nevertheless, their synthetic route provides the most direct way to obtain structures similar to classical crown ethers through Williamson ether synthesis.

2.7.1 Zimmerman Syntheses

Zimmerman 1988

In their first reported synthesis, Figure 19, Zimmerman et al. described a 7-step synthesis for their crown ether structure with an overall 0.8% yield.[63]

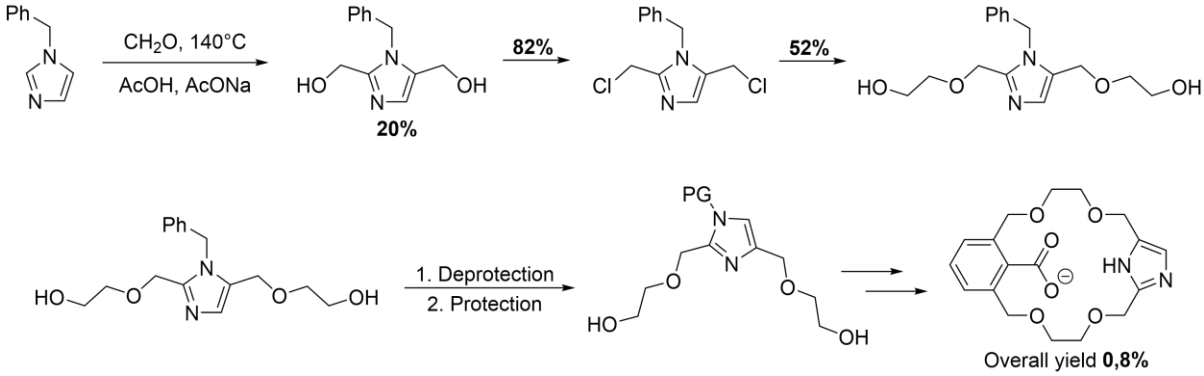

Figure 19. Summary of first synthetic scheme reported by Zimmer et al towards the final imidazole macrocycle[63].

As described earlier, the crown ether synthesis through Williamson ether reaction requires having an imidazole unit carrying either two alcohol functionalities or two leaving groups. Zimmerman and co-workers obtained this unit through an initial hydroxymethylation of N-benzyl imidazole. However, this reaction has two main limitations.

First, the reaction gives a mixture of the mono, bis and tri substituted products, and the desired isomer is only obtained in 20% yield. Second, the regioselectivity of the reaction gives the 2,5-bis(hydroxymethyl)imidazole isomer, which causes problems for cyclization. Indeed, with the 2,5-isomer, the benzyl group is oriented towards the cavity, disfavouring the conformations needed for ring closure.

As a result, they performed a subsequent chlorination, substitution with ethylene glycol, and then a deprotection/protection sequence to obtain the 2,4-substituted isomer. The choice to extend the ether functions prior to deprotection/protection, is likely due the need for these longer chains in their targeted structure and to avoid the isolation of the highly polar 2,(4)5-bis(hydroxymethyl)imidazole. The result is that their precursor for cyclization could only be obtained in 3% overall yield in five steps.[63]

Zimmerman 1989

To follow up on this work Zimmerman published a second improved synthetic route towards similar imidazole-based crown ethers.[59] They used a novel pathway to directly construct the 2,4 functionalized imidazole from substrates **1** and **2** .

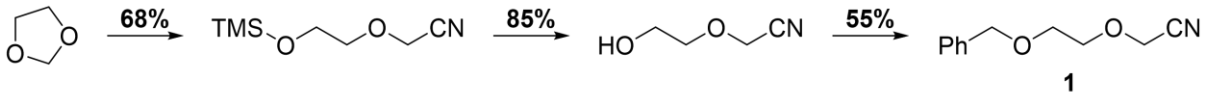

*Figure 20. Synthetic route for the precursors **1** for synthesis of the imidazole diol.*

The proposed synthetic route for the precursors **1** and **2** requires a multistep synthesis to achieve solely the precursors. They reported the synthesis of the precursor **1** at 32% overall yield over three steps (Figure 20) and precursor **2** at 31% overall yield over four steps (Figure 21).

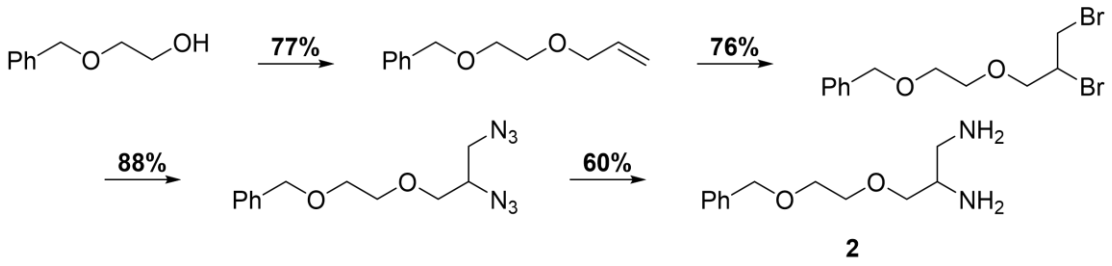

*Figure 21. Synthetic route for the precursors **2** for synthesis of the imidazole diol. [59]*

Subsequently substrate **1** is converted into its ethyl imino ether and reacted directly with **2** in a one pot process. From this a further three steps are required to get to the final diol intermediate. These steps include an oxidation, a protection and a reduction of the phenyl groups. They report an 8% overall yield for the diol over eight steps. From the diol intermediate the crown ethers are obtained through a classical Williamson ether reaction followed by deprotection. Interestingly they were able to achieve high yields (61%) for the cyclization at room temperature (Figure 22).[59]

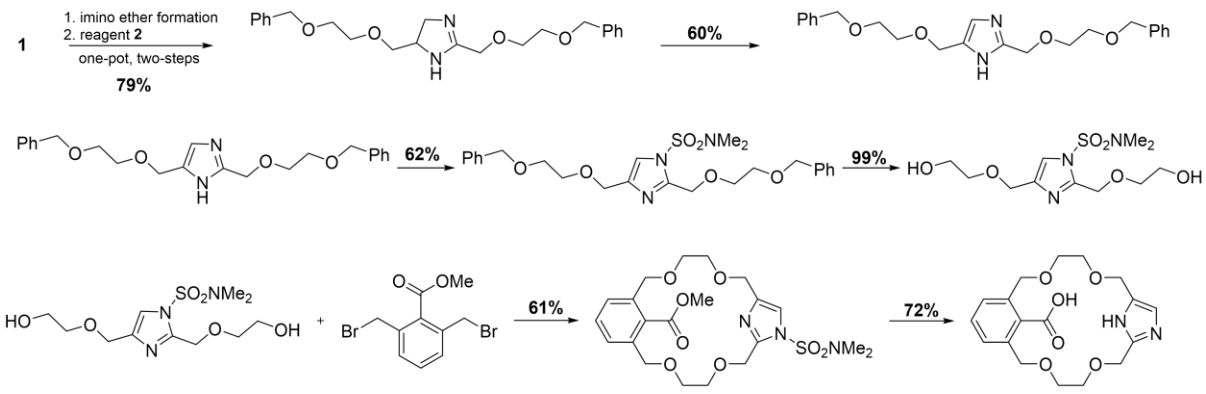

Figure 22. Full synthetic route of Zimmerman from the diol to the final cyclized product.[59]

Examining the second work towards the synthesis of the crown ether there are some drawbacks. The synthetic route for the final crown ether proceeded in a low **3.5%** overall yield over 13 steps, reflecting the laborious nature of the synthesis. A shorter and more direct synthesis of a 2,4-bis(hydroxymethyl)imidazole precursor would provide a modular and a straightforward route to imidazole containing crown ethers.[59]

3 Objectives

The design of novel crown ethers remains important for expanding their applications. In this respect, the synthesis of an imidazole containing crown ether, where a singular CH_2OCH_2 fragment is replaced with an imidazole unit, is an interesting target. This structural change allows studying the effect of the substitution on cation binding and potentially for pH responsive receptors. However, current synthesis methods suffer from low yields or long reaction sequences. To this end, three different objectives were targeted within the project.

Objective 1 – Synthesis of imidazole containing crown ethers.

As described in the introduction, most crown ethers are obtained via Williamson ether synthesis. This requires the imidazole-2,4-diol **3** as a key precursor for the macrocyclization, for the target crown ethers of this project (Figure 23). While previously synthesized by Zimmerman and co-workers, the low yield or complex synthetic pathways for **3** limit its use for crown ether synthesis. We reasoned that **3** could be easily obtained through reduction of the corresponding ester. To this end, the first objective of this work is to develop an efficient approach to **3** and show that it can be used for the modular synthesis of imidazole crown ethers with varying cavity sizes.

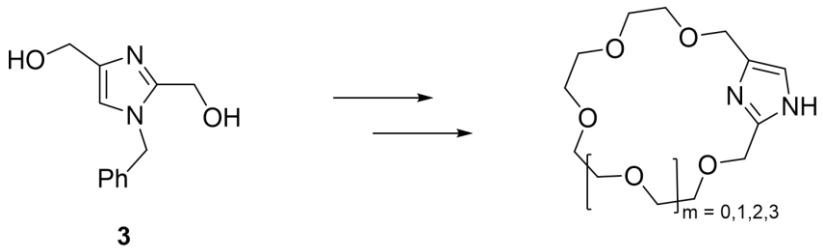

*Figure 23. Synthetic summary towards the final novel imidazole crown ethers from the important diol intermediate (**3**).*

Objective 2 – Study the influence of the imidazole on alkali metal binding.

The modification of the crown ether structure via incorporating an imidazole fragment, offers a unique possibility to study the how this fragment influences alkali metal binding (Figure 24). As such, the second objective of this work is to study the interaction between novel imidazole crown ethers with Na^+ and K^+. This will be done through NMR titrations

and the results will be compared to classical crown ethers and the related pyridine containing structures to better understand the influence of the imidazole group.

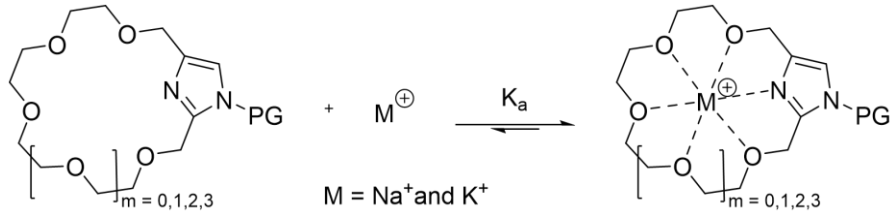

Figure 24. Binding representation of the targeted imidazole containing crown ether with a metal cation.

Objective 3 – Pseudorotaxane formation with secondary ammonium ions.

Given the importance of crown ethers for the synthesis of mechanically interlocked architectures, objective 3 will explore how the novel imidazole crown ethers influence mechanical architectures. The imidazole unit introduces increased basicity and a hydrogen bond accepting site to the cavity, therefore, it should strongly bind protonated cationic species. This expected strong affinity will be explored in the context of pseudorotaxanes. The structural binding of secondary ammonium ions will be explored as show in Figure 25, and compared to similar pseudorotaxanes.

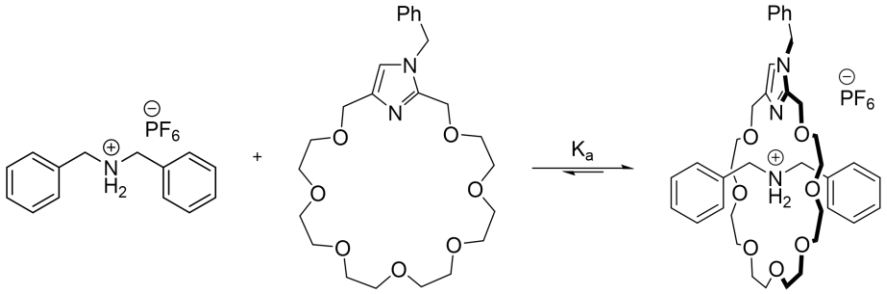

Figure 25. Plans for pseudorotaxane formation for the imidazole crown ethers.

4 Results and Discussion

4.1 Retrosynthesis

Two synthetic pathways were explored during the investigation, with the goal of synthesizing the imidazole macrocycles at good yields. Both synthetic pathways utilize Williamson ether synthesis to get the final cyclized macrocyclic products.

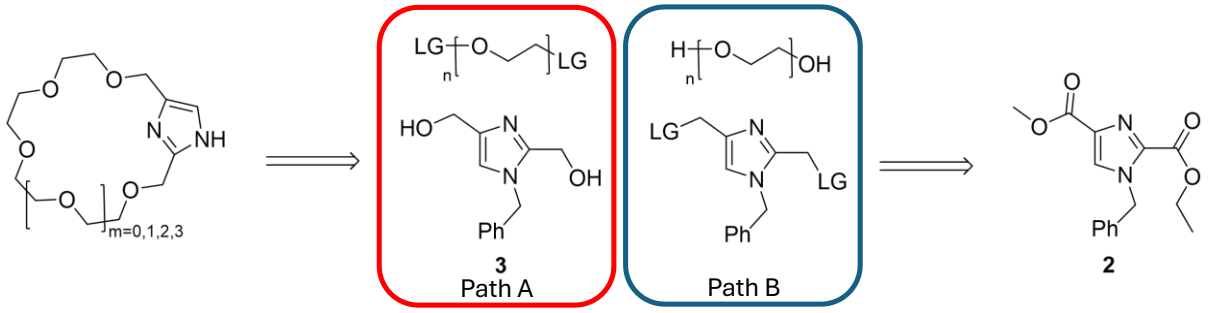

Figure 26. Retrosynthetic approach for the target imidazole crown ether.

Prior to starting the project, a retrosynthetic analysis of the desired final deprotected imidazole macrocycle was performed (Figure 26). Disconnection of one of the ether linkages within the macrocyclic framework revealed two key fragments. These being the disubstituted imidazole and the other a polyethylene glycol chain with varying lengths. The reaction proceeds through an S_N2 intramolecular reaction which is favoured by the templating base and high dilution conditions.

For the S_N2 reaction either of the fragments could contain the electrophilic LG or the nucleophilic -OH. This gave two complementary synthetic paths (Path A and Path B) to get to the final imidazole macrocycle. For either pathway to be successful the most important synthetic intermediate is substrate **3**. The glycol chain at different lengths is available commercially, and the tosylation of a glycol chain for path A is already reported. The imidazole for path B can also be readily obtained from substrate **3** via a classical chlorination reaction. As such, the 2,4-bis(hydroxymethyl)imidazole intermediate **3**, is key to the synthesis. Access to this intermediate was envisioned from reduction of the corresponding imidazole diester.

4.2 Synthesis

4.2.1 Synthesis of Imidazole diol intermediate **3**

Based on the above retrosynthesis, diol **3** was the initial key target and can be readily obtained by reduction of diester **2**. This exact diester has not been described previously, however, Branco *et al.* showed that the related N-methyl-2,4-(hydroxymethyl)imidazole could be obtained in two steps from ethyl cyanoformate and an N-substituted hydroxyl amine.[65]

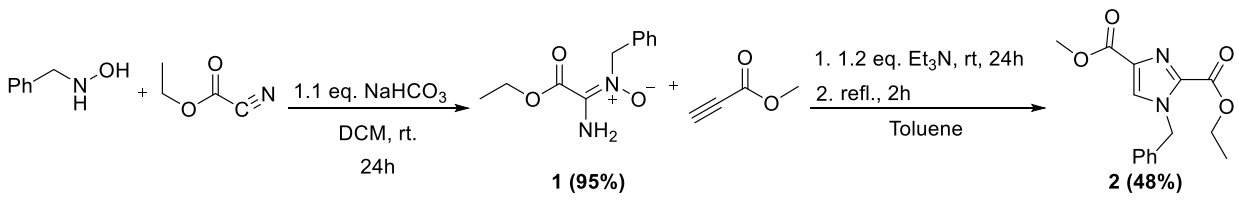

*Figure 27. Reaction scheme to give the imidazole diester intermediate **2**.*

To increase the solubility, we extended their approach via using N-benzyl hydroxylamine, the possibility of readily removing the benzyl group later was also an important consideration. To this end, N-benzyl hydroxylamine hydrochloride was reacted with ethyl cyanoformate in the presence of a base. The reaction proceeds through nucleophilic addition of the hydroxyl amine nitrogen onto the nitrile group of ethyl cyanoformate to give nitrone intermediate **1** at 95% yield. Nitrone **1** was then reacted with methyl propiolate and Et_3N as a base (Figure 27). For this reaction, there is an initial Michael addition, with a 1,4 addition of the nitrone oxygen onto methyl propiolate. Subsequently, the reaction under reflux undergoes a 3,3 sigmatropic rearrangement, to give an aldehyde containing intermediate (Figure 28). Condensation with the imine then gives the imidazole diester (**2**) in 46% overall yield across the two steps.

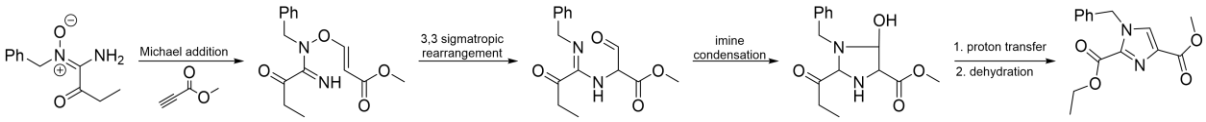

Figure 28. Imidazole formation mechanism.

One of the bottlenecks of the reaction was the solubility of the substrates in toluene. Following, addition of all reagents, a precipitate forms overtime, requiring extended sonication prior to being placing under reflux. Possibly, performing a solvent screen to solubilize the products better could have enhanced the reaction, this was not done due to time considerations.

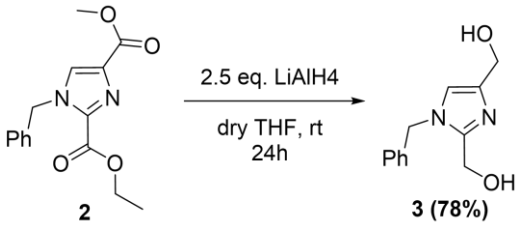

*Figure 29. Reduction reaction to give the important diol intermediate **3**.*

Following the cyclization, substrate **2** was reduced using $LiAlH_4$ (Figure 29). This was one of the most important steps during the project, as it yields the key intermediate **3**. Previous attempts in the group were made to reduce a similar substrate containing a methyl protecting group instead of a benzyl group. The reaction was successful, but the product had a high polarity, rendering it highly soluble in water, making isolation not possible. With the benzyl protecting group on substrate **2** no solubility issues were observed, allowing isolation. The reduction worked well at small scale, where 90% yields were obtained prior to purification, with the crude product being suitable for use in subsequent reactions. However, upon scale up, additional impurities were observed, requiring purification of **3** by column chromatography using highly polar solvents and leading to a yield of 78%. Nevertheless, gram quantities of intermediate (**3**) three could

be obtained. Giving **3** in 36% overall yield in just three steps, offering a substantial improvement over the procedures described by Zimmerman *et al*.

4.2.2 Imidazole Macrocycle Cyclization

By Williamson ether synthesis, from **3** two possible pathways as describe above can be envisaged for the imidazole crown ethers (Figure 26). For pathway A, the tosylated glycol chain was prepared previously within the group at good yield utilizing a reported procedure.[66] Initially, it was suspected that utilizing the imidazole as the nucleophile would work best and avoid potential problems with the activation of the electron rich imidazole. Therefore, the first cyclization attempts were done with the diol as the nucleophile and a tosylated glycol chain as the electrophile.

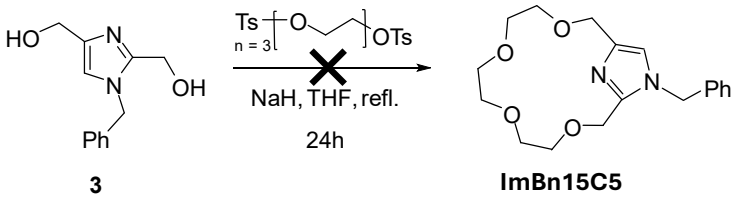

Figure 30. Preliminary cyclization attempts.

To avoid significant polymerization, dilute conditions were used to favour the intramolecular reaction. Pseudo high dilution conditions were simulated by using syringe pumps to slowly add a solution of the imidazole and glycol chain, diluted as much as permitted by the setup, to a refluxing solution of NaH in dry THF. Furthermore, NaH introduces Na^+ into solution, creating a template effect to facilitate the macrocyclization. Using this set up a preliminary cyclization was attempted, following the reaction scheme in Figure 30. Unfortunately, no product was observed in the ^1H NMR spectrum of the crude reaction mixture. The unsuccessful cyclization was attributed to possible E2 eliminations occurring on the tosylated substrate. Under basic conditions the β-H can be removed, and the C-OTs bond is broken to give the corresponding alkene polyether. Previous attempts within the group for a similar reaction were unsuccessful, all this meant that pathway A was abandoned.

*Figure 31. Chlorination reaction to give the dichlorinated imidazole (**4**).*

For pathway B, a good leaving group had to be introduced on the imidazole. Therefore, a chlorination reaction was performed on substrate **3** to give the dichlorinated imidazole (**4**) (Figure 31). The reaction to synthesize substrate **4** worked, and the product was

obtained at near quantitative yield. Importantly, previous attempts within the group to chlorinate a similar substrate resulted in the trichlorinated product. This was due to the reaction being run at reflux and leading to the decomposition of $SOCl_2$ into Cl_2, which chlorinates the aromatic core. This shows the importance of running the reaction at room temperature. While, this was a robust reaction, the product obtained was a hydrochloride salt, which decreased the solubility of substrate **4** in most organic solvents. To circumvent this issue a basic workup was attempted, to deprotonate substrate **4**. However, upon deprotonation and under atmospheric conditions, degradation was observed. Therefore, substrate **4** was used in macrocyclization in its protonated form as the hydrochloride salt.

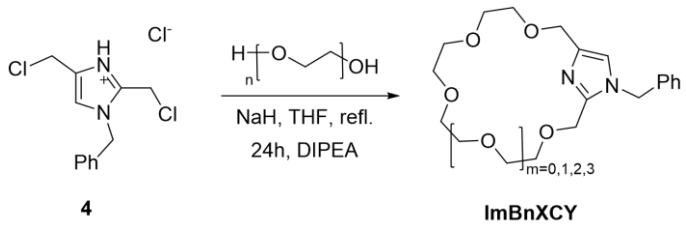

*Figure 32. Final cyclization scheme to give the final **ImBn** macrocycles.*

However, the direct use of the salt proved to be challenging for the slow addition via syringe pump as its limited solubility in THF lead to the clogging of the needles. To solubilize the substrate, one equivalence of DIPEA was added to the substrate solution prior to the slow addition. Under these conditions, reactions with tri-, tetra-, penta-, or hexaethyleneglycols afforded respectively the desired **ImBn15C5**, **ImBn18C6**, **ImBn21C7**, and **ImBn24C8** crown ethers in 6 to 36% yield after chromatographic purification (Figure 32).

The smallest macrocycle synthesized was the **ImBn15C5**. This was the least successful cyclization with the lowest yield at only 6%. Upon examining the crude ^{1}H NMR it was clear to see that the intramolecular reaction is less favoured than for the other derivatives as evident by the lower yield. Substantial polymer formation could be observed. It can be reasoned that due to the shorter glycol chain and the rigidity of the imidazole, there is potentially too much ring strain to favour the cyclization. For **ImBn18C6**, where some of this strain would be alleviated, a higher (36%) yield was obtained. Finally, for **ImBn21C7** and the **ImBn24C8**, the yields 22% and 15% respectively, were higher than **ImBn15C5** but notably lower than **ImBn18C6** potentially reflecting the increased degrees of freedom in the longer ethylene glycol chains. The higher degree of freedom also has entropic penalties for cyclization, because the greater number of accessible conformations reduces likelihood of beneficial preorganization for macrocyclization. We also cannot rule out a stronger Na^+ templating effect with **ImBn18C6** relative to the other derivatives, which is supported by their different binding constants. Nevertheless, this demonstrates that high yielding cyclization is a fine balance between avoiding excessing ring strain, but enough to restriction for ring closure.

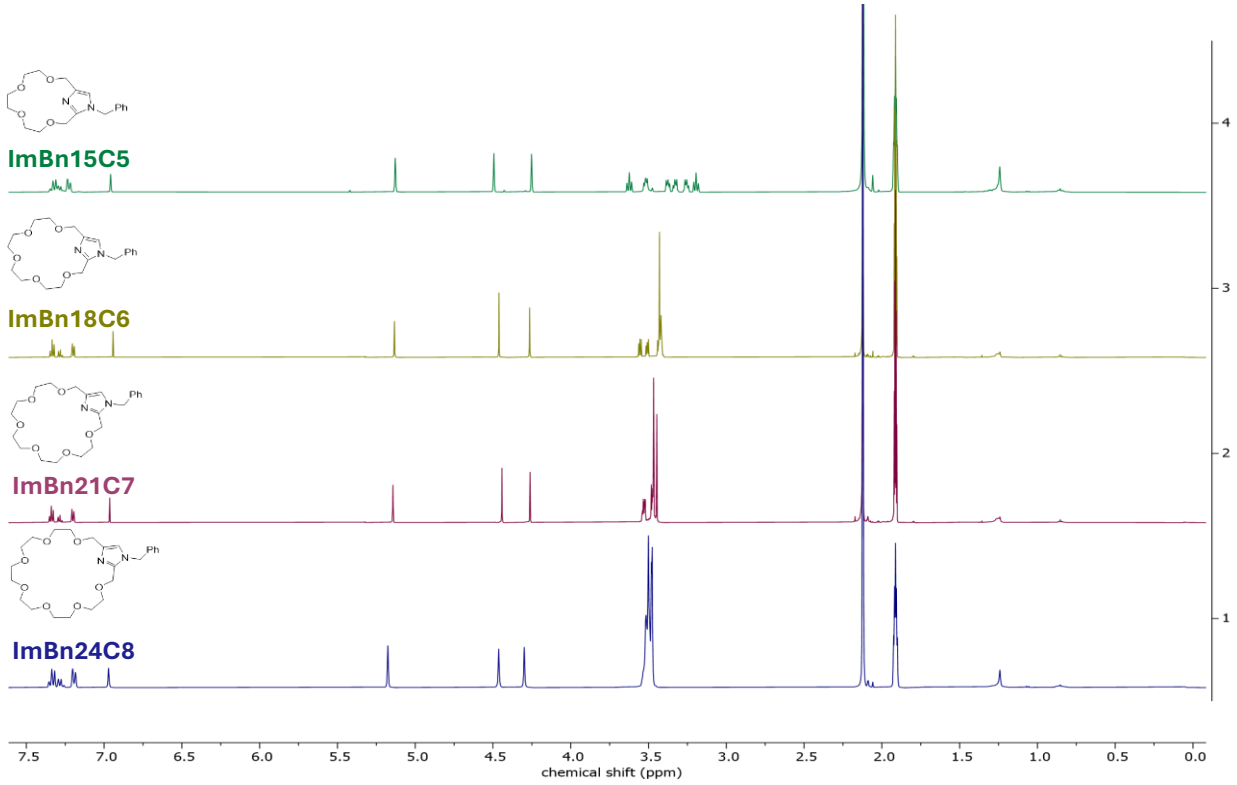

Figure 33. Stacked ^{1}H NMR spectra of all four final imidazole macrocycles.

All the different crown ethers could be obtained in good purity. The final spectrum obtained for each macrocycle are shown in Figure 33. For all of the derivatives, there are three defined separate signals between 4.0 and 5.5 ppm. The most down field shifted of these corresponds to the CH_2 of the benzyl group, while the two between 4.2-4.5 ppm correspond to the CH_2 groups on the imidazole. While these signals and the aromatic region of the four crown ethers look similar, interesting differences were observed for the resonances corresponding to the ethylene groups. As the ring size decreases, these signals become significantly more resolved and splitted. This is especially evident when looking at the NMR spectrum of **ImBn15C5**, where these signals are almost completely resolved. This likely occurs due to the more distinct local environments and the restricted conformational motion of the smaller cavity size. Whereas the larger macrocycles are more flexible and show greater spectral overlap due to the increased conformational averaging of the ethylene environments. This restricted motion also hints towards the increased ring strain for the **ImBn15C5**.

4.2.3 Deprotection of the Imidazole Macrocycles

We next looked to remove the benzyl protecting group. Part of the interest in imidazoles is their chameleonic nature, with exchange of protonated forms being possible through tautomerization, protonation, or deprotonation, all of which can influence their cation binding properties. For the imidazole crown ethers, the benzyl protecting group limits this as it locks tautomerization.

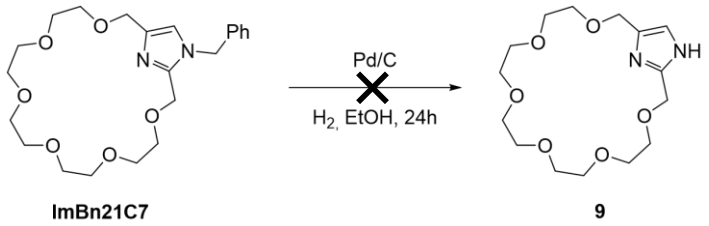

Figure 34. Preliminary unsuccessful reduction reaction scheme via hydrogenolysis, for the deprotection of the imidazole crown ethers.

For the deprotection, palladium catalysed hydrogenation was tested with **ImBn21C7**. The reduction was attempted following the reaction scheme on Figure 34, using Pd/C (20% wt) under hydrogen atmosphere. However, no reaction was observed by ^{1}H NMR, and the starting material was recovered. This is coherent with what was reported by Zimmerman *et al*, who described that deprotection only occurred when concentrated sulfuric acid was added to the reaction. Addition of the acid should protonate the imidazole yielding a better leaving group and facilitating the deprotection.

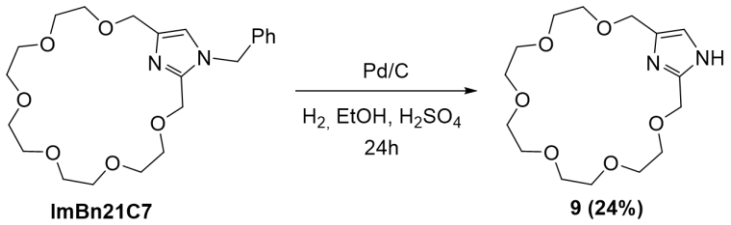

Figure 35. Reduction reaction scheme via hydrogenolysis, for the deprotection of the imidazole crown ethers.

Indeed, with the addition of a small amount of H_2SO_4, deprotection could be observed by ^{1}H NMR and mass spectroscopy. However, additional side products were also present. Still, the deprotected product could be isolated in 24% yield after workup and purification (Figure 35). One possible reason for the low yield could be associated to the work up. Following, filtration, a basic workup was performed to deprotonate the product **9.** NaOH was used to raise the pH to 14 which introduces the possibility of further deprotonating the imidazole, something that could be facilitated by the binding of an Na^+ ion. Potentially, taking care to limit the increase of the pH using a base without possible coordination could lead to increased yield. Furthermore, the reaction was run at very small scale making the purification challenging and contributing to the low yield. Overall, the deprotection process must be optimized further or new conditions used to deprotect the imidazole.

This synthesis presented here gives direct access to four novel imidazole crown ethers (**ImBn15C5**, **ImBn18C6**, **ImBn21C7**, and **ImBn24C8)** which vary in cavity size. This route offers advantages over current reported methods which employ laborious, low yielding syntheses towards similar crown ethers derivatives. Also reporting a modular and scalable pathway to the important diol **3** which can be used in downstream Williamson ether synthesis.

Notably the work by Zimmerman *et al*, which reports the closest scaffold for the macrocycles in this project, reported only an overall yield of 3.5% over 13 steps. In this project we report a 5-step synthetic route with an overall yield ranging between 2% and 13% depending on the crown ether size. This is already a consequential improvement. The imidazole crown ethers contain a cavity which could bind cationic guests, with subtle differences compared to classical crown ethers. Therefore, the binding of these novel imidazole crown ethers was explored further. The deprotection of the macrocycles would have introduced an extra element to the binding study due to possible tautomerization and (de)protonation. However, the deprotected derivatives were not used further due to the complications during the deprotection reactions.

4.3 Study of alkali metal binding by the imidazole crown ethers.

Having successfully synthesized and isolated the imidazole crown ether macrocycles, the next step in the project was to do host-guest studies. In order to understand the binding properties of the imidazole crown ethers with Na^+ and K^+. This analysis of the binding was done sequentially. Initially, the specific chemical shift patterns from ^1H NMR titrations are explored to form qualitative conclusions on the binding behaviour of the macrocycles. This binding in the solid state is further developed using crystallography. Finally, the data from ^1H NMR titrations can be extrapolated, and a regression model based on a 1:1 complexation can be constructed on the binding. This gives a quantitative analysis of the binding through the association constant (K_a) for each system.

4.3.1 NMR titrations

During an ^1H NMR titration a guest solution is added gradually to a host solution. In this work the host refers to the imidazole crown ether macrocycles, and the guest refers to Na^+ or K^+. When various aliquots of guest are added, they interact with host in solution. This interaction between the two leads to a physical change, which can be followed by ^1H NMR. This physical change is reflected by the changes in the chemical shifts for specific protons. The analysis of the difference in chemical shift can elucidate the interaction between the two entities. Figure 36, demonstrates the proposed interaction between host and guest for this project.

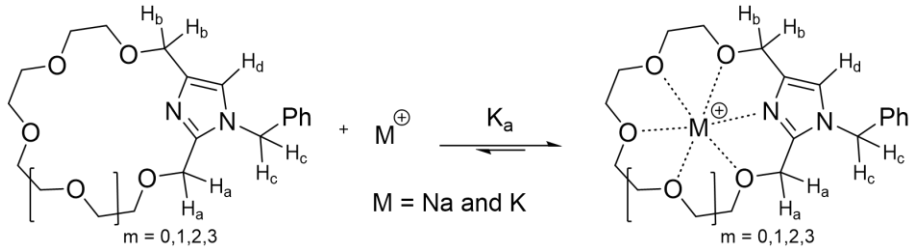

Figure 36. Proposed binding mode and proton assignment for the imidazole crown ethers with the cationic guests (M = Na^+or K^+). The labelled protons H_a to H_d correspond to the resonances monitored during ^1H NMR titrations.

The titrations were carried out in MeCN using dilute concentrations (0.5-1.5 mM). The amount of dilution was dependent on the system and the magnitude of the binding, stronger binding requires greater dilution for an accurate titration. MeCN was selected as the solvent because it is polar and weakly coordinating. Therefore, it does not disrupt the host-guest interactions, while nicely dissolving the ionic salt and the macrocycles. The ionic salts used to introduce the cationic guest into solution were KPF_6 or $NaPF_6$. These salts were used as the PF_6^- counterion has a diffuse charge, therefore it is weakly coordinating. This minimizes the competitive ion pairing or direct interaction with the host-guest complex. The solvent and salt choice allows the attribution of the chemical shift changes on the ^1H NMR primarily to host-guest complexation.

The samples for the ^1H NMR titrations were prepared by creating a stock solution of host and a stock solution of guest which was ten-fold more concentrated. The guest stock solution was made by dissolving the solid guest in host stock solution to mitigate dilution errors.

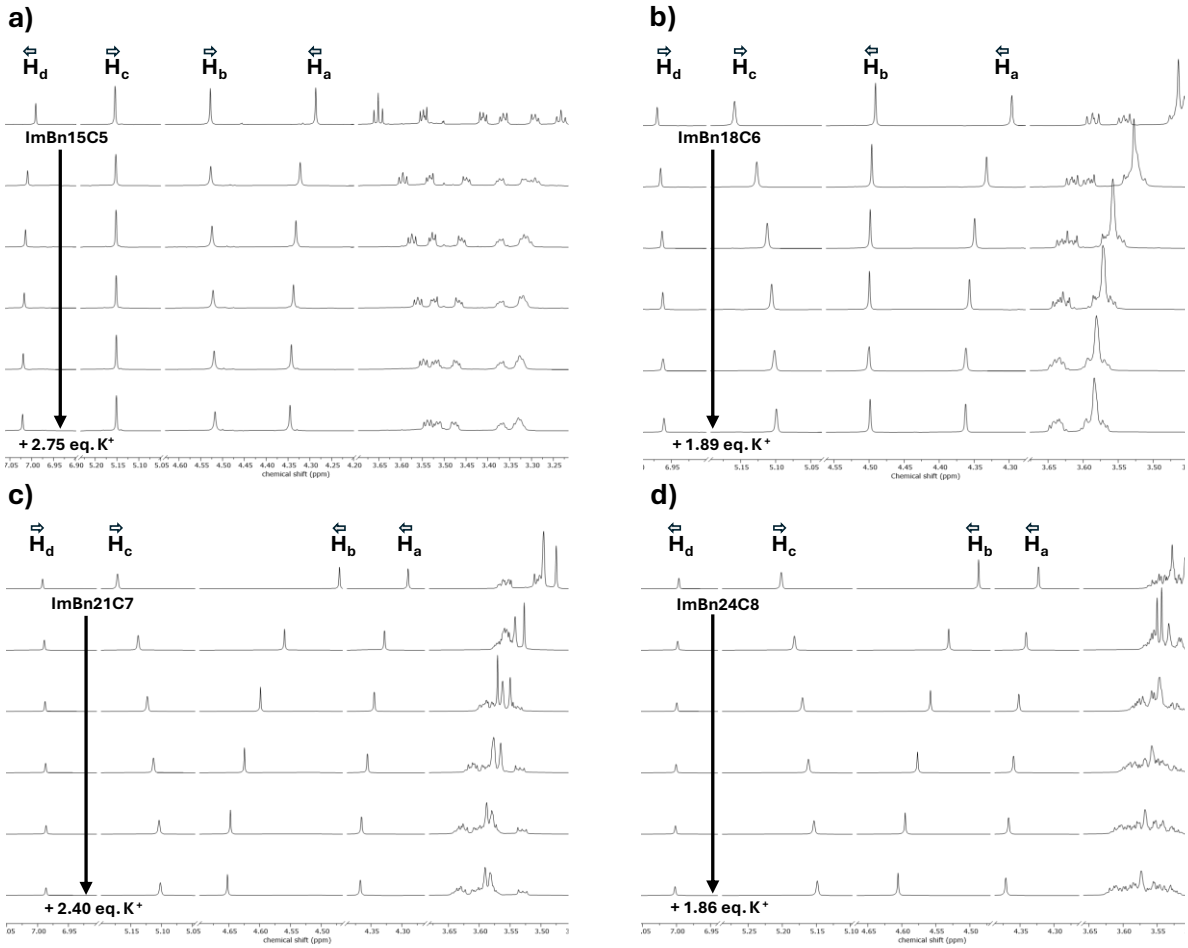

*Figure 37. Stacked excerpt of ^{1}H NMR spectra of four separate titrations of a) **ImBn15C5** (0.55 mM) b) **ImBn18C6** (0.43 mM) c) **ImBn21C7** (0.55 mM), and d) **ImBn24C8** (1.61 mM) with K^+ in MeCN at 20°C. Spectra are shown from top to bottom with increasing equivalents of K^+ added. The arrow (⇦/⇨) above the signals indicate the direction of the chemical shift during the titration.*

Figure 37 and Figure 38 show the stacked spectra and the chemical shift changes with added K^+ or Na^+. For each titration 20 ^{1}H NMR spectrum were recorded for various aliquots of guest addition. However, in Figure 37 and Figure 38 only six spectra are shown for clarity.

For both guest additions similar results were obtained. Upon titration of the of the crown ether derivatives with the respective cations, noticeable changes in chemical shift are observed, but no separate resonances corresponding to the complex appear. This suggests that the system is in fast exchange relative to the NMR chemical shift timescale. This means the rate of exchange between complexed and uncomplexed species is faster than the frequency separation between the two states. Therefore, a weighted averaging of the signals for the complexed and uncomplexed states is observed in the ^{1}H NMR spectrum. The position of the observed signals thus correlates to the extent of complexation.

The direction and the magnitude of this shift can provide an insight into the parts of the macrocycle which are most affected by binding. Protons near the binding cavity are the

most susceptible to electronic changes due to cation binding and therefore exhibit the greatest change in chemical shift. The protons in the -CH_2O- units of the macrocycle which resonate between 3.4 and 3.7 ppm are present around the cavity and in proximity to the cation. For macrocycles **ImBn18C6**, **ImBn21C7**, and **ImBn24C8** a consistent downfield shift is observed for these protons. This is due to cation binding which polarizes the cavity and reduces the electron density around the ether oxygens and nearby C-H environments, leading to deshielding of the protons.

Similar downfield shifts are observed for the 2-, and 4- position CH_2 groups on the imidazole, H_a and H_b, with **ImBn18C6**, **ImBn21C7**, and **ImBn24C8**. However, for **ImBn15C5**, only H_a undergoes a downfield shift, while H_b shifts upfield. This variation may reflect a difference in conformational changes upon cation binding. Notably, the increased rigidity enforced on the cavity by the imidazole substituent and the short glycol chain, could potentially push the -$CH_{2(b)}O$- group further away from the binding cavity, making it less susceptible to electronic changes, enforced by the cation binding. Changes in the freedom of the benzylic group may also give differences in the shielding of H_b in the free host.

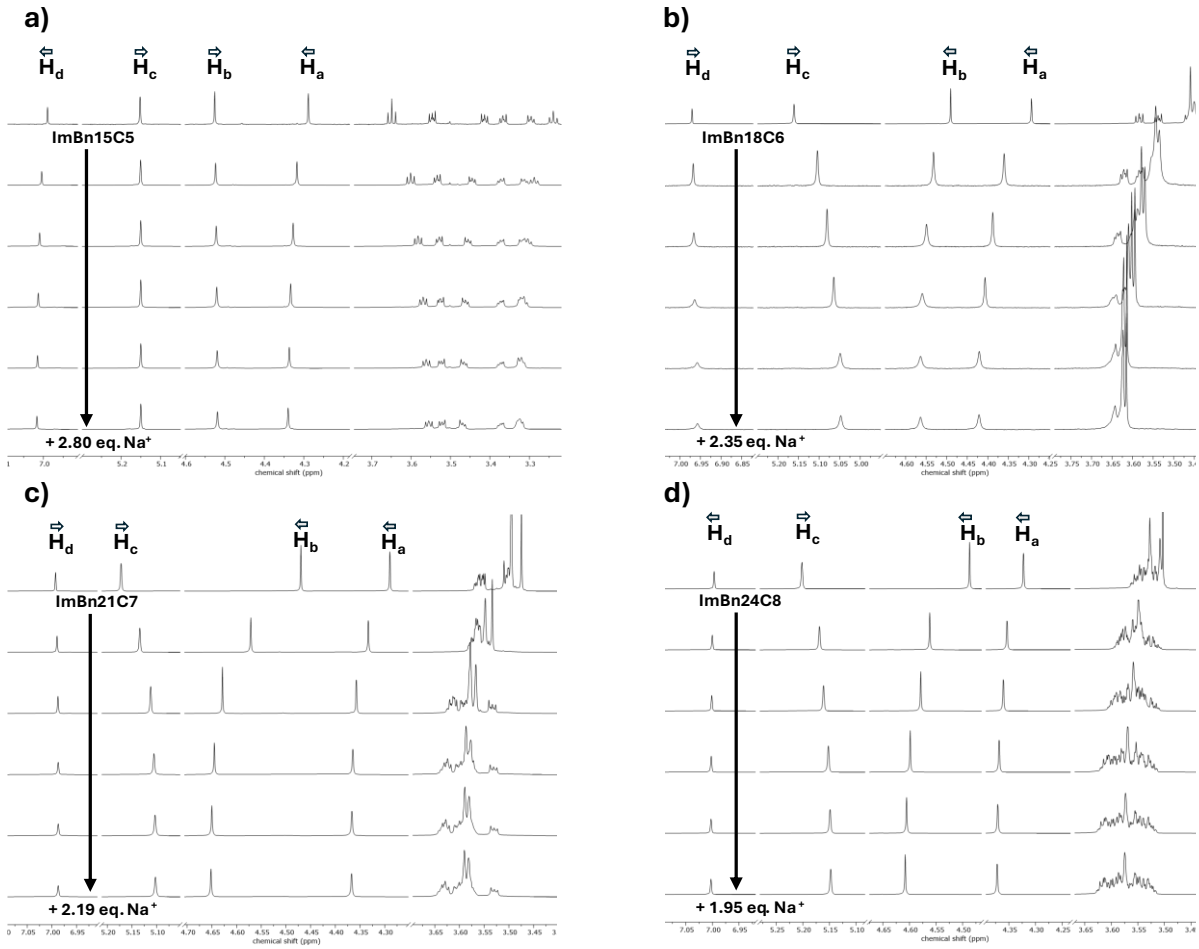

*Figure 38. Stacked excerpt of ^{1}H NMR spectra of four separate titrations of a) **ImBn15C5** (0.55 mM), b) **ImBn18C6** (0.45 mM), c) **ImBn21C7** (1.71 mM), and d) **ImBn24C8** (1.41 mM) with Na^+ in MeCN at 20°C. Spectra are shown from*

top to bottom with increasing equivalents Na^+. The arrow (⇦/⇨) above the signals indicate the direction of the chemical shift during the titration.

Relative to the latter, in all cases, the benzylic resonance (H_c) undergoes an upfield shift. The magnitude and consistency of shift were not expected considering the distal position of the benzylic protons relative to the cation binding cavity. However, this observation suggests that the free macrocycle likely folds on itself, placing the benzylic group closer to the cycle. Such observations are consistent with literature results on traditional crown ethers. The structures adopt a rigid collapsed conformation in solution to avoid repulsion between the oxygen atoms in the ring. Consistent with this, the energy minimized structure of free **ImBn18C6**, obtained through DFT calculations (ωB97X-D4/def2-TZVPP), suggest that in the absence of a cation, the plane of the imidazole ring should be nearly perpendicular to the macrocyclic portion of the molecule (Figure 39). This places the benzylic group in proximity to the ether oxygens. This could be expected to lead to deshielding of these protons in the free host, while cation coordination should force this group more to the exterior of the structure. This can be seen in the X-ray structure of **ImBn18c6•KPF_6**.

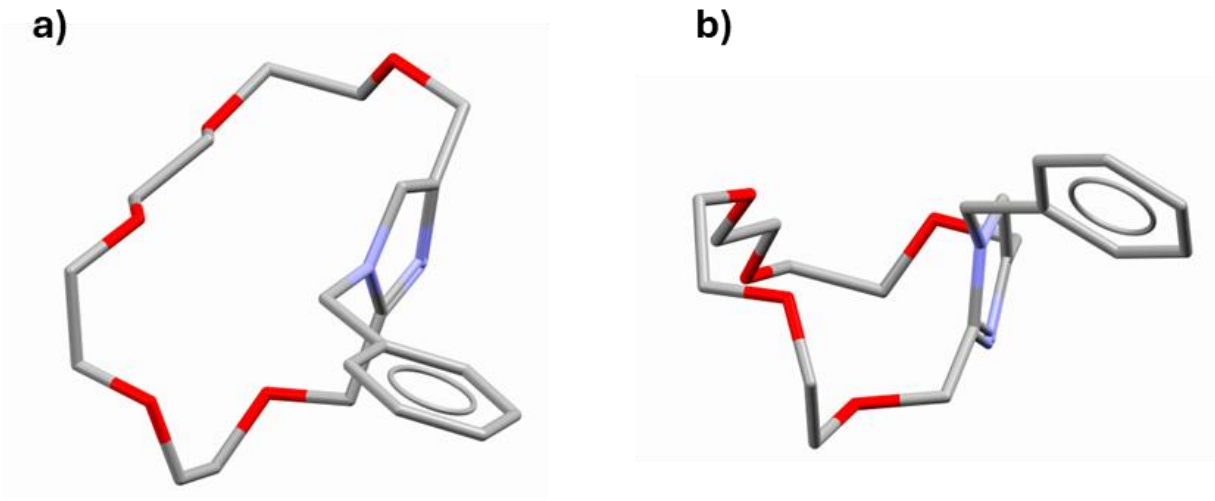

Figure 39. a) Vertical and b) horizontal view of the energy minimized (ωB97X-D4/def2-TZVPP) structure for free ***ImBn18C6.***

4.3.2 Imidazole Macrocycle Crystal Structure

Crystals of **ImBn18c6•KPF_6** suitable for X-ray diffraction were grown by slow diffusion of hexane into a solution of DCM containing a 1:1 mixture of the crown either and cation. The complex crystallized in the P1 space group, giving the crystallographic structure presented in Figure 40.

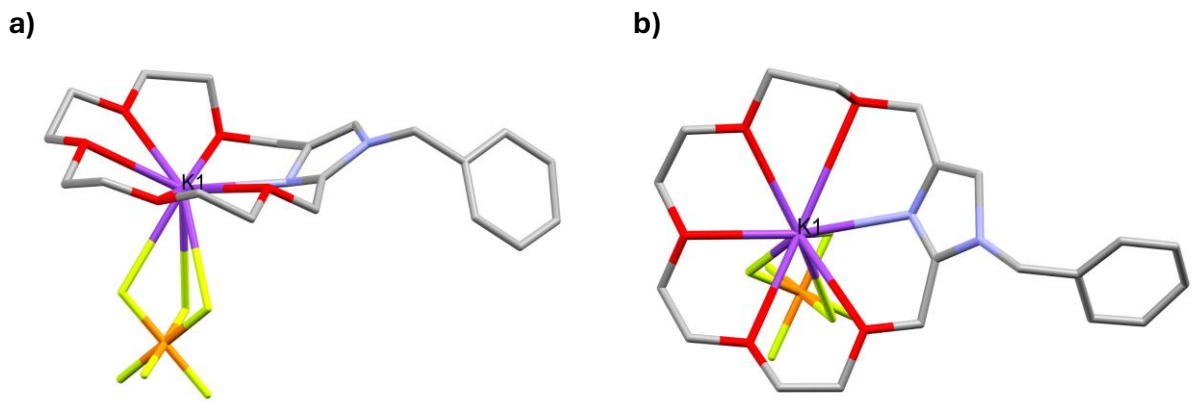

*Figure 40. a) Horizontal and b) vertical view of the **ImBn18C6** K^+ complex crystal structure.*

When analysing the crystal structure, various conclusions can be made on the solid-state interactions of the system. Firstly, the crystal structure confirms the expected 1:1 stoichiometry of the binding. The K^+ places itself closer to the ether oxygen atoms rather than the imidazole nitrogen, defining the main binding pocket. This is due to the interaction of K^+ with oxygen heteroatoms being stronger than nitrogen heteroatoms. Still, from the crystal structure it is clear that the imidazole unit does not simply act as a passive substituent but does participate in cation coordination.

Although PF_6^- anion was selected for its non-coordinating properties, from the solid-state structure the interaction of PF_6^- with K^+ is observed. The interaction of the anionic PF_6^- slightly displaces K^+ out of the binding cavity, disrupting the planar coordination.

In addition, upon coordination of the imidazole the benzyl protecting group is pushed away from the cavity. This is a further indication of the binding induces conformational rearrangement of the macrocycle, consistent with the upfield shift of H_c.

Overall, the unsymmetric and distorted structure of the bound macrocycle is clear relative to a classical crown ether geometry. To characterize this distortion more coherently, bond distances and bond angles provided by the crystallographic structure were explored.

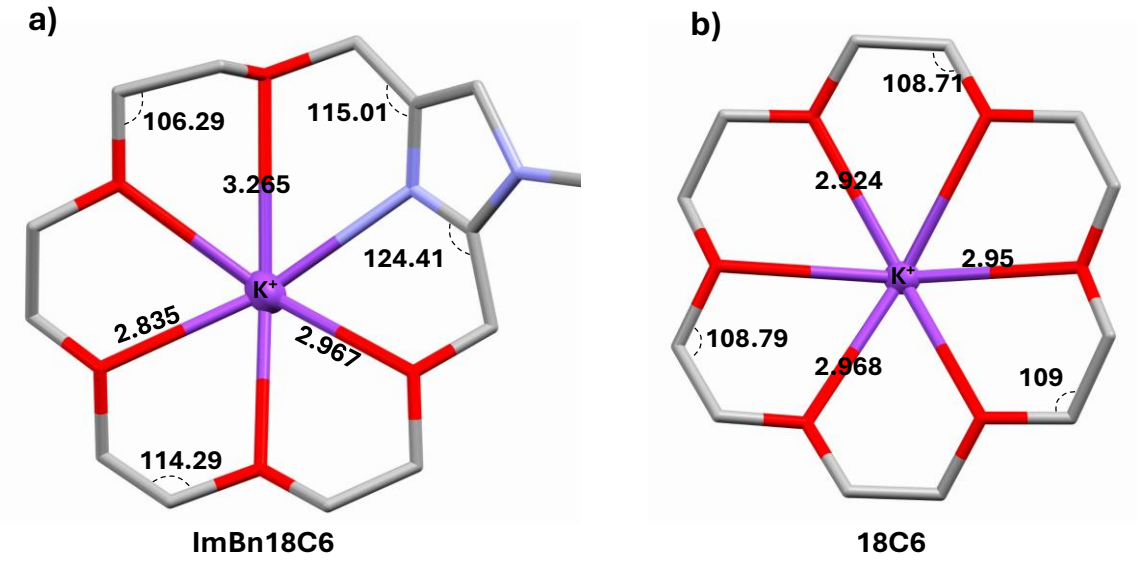

*Figure 41. Crystal structure with important bond angles and bond distances (Å) of a) **ImBn18C6** bound to K^+ and b) a reported structure of 18C6 bound to K^+.*[74]

Focusing on the cavity of **ImBn18C6** (Figure 41a) and comparing the geometric values with a classical **18C6** crown ether (Figure 41b), several structural conclusions can be formulated.[67] The distorted and unsymmetric nature of the cavity of **ImBn18C6** is confirmed by the large range of bond angles between 104 to 124°. This is due to the imidazole introducing sp^2 geometry into the cavity making it more rigid. This is confirmed by the two large bonds of angles 124° and 115° directly adjacent the imidazole. In comparison, classical crown ether are more symmetric and less rigid with bond angles all around 109°.

The coordination distances also provide an interesting comparison, confirming the preferential placement of the K^+ closer to the ether functionalities. The oxygen-K^+ contact directly adjacent the imidazole are long at 2.967 Å and 3.265 Å as demonstrated in Figure 41a. Whereas the other oxygen-K^+ contacts range between 2.730 and 2.835 Å are shorter demonstrating a preferential coordination environment. Comparing this to **18C6** the contact distances are more uniform all of which are close to 2.9 Å. This further enforces the asymmetric binding mode and the distortion caused by the imidazole.

Furthermore, there is a large contact distance of 3.265 Å for the coordination site adjacent H_b, meaning the proton is placed further away from the cavity. This potentially explains the smaller chemical shift change observed for these protons in the titrations with **ImBn18C6**.

4.3.3 Reporting K_a from Titration Experiments

Having gained a qualitative and structural understanding on the binding between the cationic guests and the imidazole crown ether macrocycles. Next steps were to extrapolate data from the chemical shifts to perform a fitting and obtain a regression

model, which allows to determine the K_a of each system. This gives an important quantitative variable explaining how the systems interact.

$$\mathbf{H} + \mathbf{G} \underset{}{\overset{K_a}{\rightleftharpoons}} \mathbf{HG} \qquad (6)$$

The overarching idea of getting a quantitative output from a supramolecular titration is to monitor a physical change (ΔY) through an analytical method such as UV-Vis, NMR, or fluorescence. This physical change which correlates to the proportion of the host-guest complex allows K_a calculation through mathematical modelling. For this project ^{1}H NMR was the chosen analytical method and therefore this physical change corresponds to the changing in chemical shift upon complexation ($\Delta Y = \Delta\delta$). [68]

$$\Delta Y \propto [HG] \qquad (7)$$

4.3.3.1 Relating Ka to the chemical shift pattern.

The direct quantitative output of an ^{1}H NMR titration is the K_a which measures the affinity between two interacting species in equilibrium. A stronger interaction between the two species means a greater proportion of complex relative to free species and therefore a higher K_a. For a simple 1:1 stoichiometry K_a is described by equation 8, where it is the ratio of bound complex concentration ($[HG]$) to unbound molecules ($[H][G]$) in solution.[69]

$$K_a = \frac{[HG]}{[H][G]} \qquad (8)$$

The concentrations of $[H]$, $[G]$ and $[HG]$ are not directly known. Therefore, using known mass balance relationships given by eq (9) and (10) where $[H]_0$ and $[G]_0$ are the initial concentrations, a substitution into eq (8) can be done to reduce the number of unknowns.

$$[H] = [H]_0 - [HG] \qquad (9)$$

$$[G] = [G]_0 - [HG] \qquad (10)$$

Substitution into equation (8) yields:

$$K_a = \frac{[HG]}{([H]_0 - [HG])([G]_0 - [HG])} \qquad (11)$$

Equation 11 can be expanded and then rearranged to give a function for $[HG]$ eq (12). This gives two unknown variables $[HG]$ and K_a.

$$[HG] = \frac{1}{2}\left\{\left([G]_0 + [H]_0 + \frac{1}{K_a}\right) - \sqrt{\left([G]_0 + [H]_0 + \frac{1}{K_a}\right)^2 - 4[H]_0[G]_0}\right\} \quad (12)$$

However, it is not possible to know the concentration of the complex $[HG]$ in solution. Instead, the specific chemical shift changes are related to the relative proportion of free and bound species. The observed chemical shift can be expressed as.

$$\delta_{obs} = \delta_H \frac{[H]}{[H]_0} + \delta_{HG} \frac{[HG]}{[H]_0} \quad (13)$$

Rearrangement of (13) by inputting (9) and (10) gives (14), which directly links the total chemical shift ($\Delta\delta$) to [*HG*].

$$\Delta\delta = \Delta\delta_{HG}\left(\frac{[HG]}{[H]_0}\right) \quad (14)$$

However, the main goal is to find the K_a value and therefore relate $\Delta\delta$ to K_a. Consequently, equation 12 becomes important which gives [*HG*] as a direct function of K_a and known total concentrations. This expression allows chemical shift changes ($\Delta\delta$) to be fitted directly as a function of K_a through substituting equation (12) into (14). This substitution yields two unknowns $\Delta\delta_{HG}$ and K_a, which are defined as the fitting parameters, meaning these values are varied to get a non-linear regression model to match the data from the titrations.[70]

The explanation above on K_a calculation from chemical shift patterns is for a simple 1:1 stoichiometry, as the binding explored during this work had this stoichiometry. A more thorough review of the equations and more complex stoichiometries is described in thorough detail by Thordarsson et al.[70]

4.3.3.2 Fitting on Titration Data to Report K_a.

The relationship between K_a and $\Delta\delta$ are demonstrated previously. However, tangibly getting to a numerical value for K_a is not, and this is done through a mathematical fitting. Essentially, the observed chemical shift changes ($\Delta\delta$) at various equivalents of guest are plotted on a graph and fitted, to generate a binding isotherm.

A non-linear fitting procedure is applied to model the titration experiment. The basis of the fitting performed is the relationship between the observable ($\Delta\delta$) and K_a, as demonstrated by (12) and (14).

During the fitting process K_a and $\Delta\delta_{HG}$ are treated as the fitting parameters, where $\Delta\delta_{HG}$ is the maximum chemical shift at full complexation. For the fitting process the model inputs various values for $\Delta\delta_{HG}$ and K_a within a realistic range, to get a calculated $\Delta\delta$ value for a specific equivalence. This is then compared to the experimental output ($\Delta\delta$) obtained through ^{1}H NMR titrations. The comparison will be made between the calculated and observed $\Delta\delta$ values, and the difference is quantified as the residual error.

The fitting algorithm iteratively adjusts values for K_a and $\Delta\delta_{HG}$ to get as close as possible to the experimental data by minimizing the residual error reflected by the residuals. This is repeated for each data point which is the $\Delta\delta$ at different equivalences, giving a regression model that follows the datapoints. Therefore, an optimal K_a value is obtained for the system when the corresponding regression model fits closely to the experimental data.

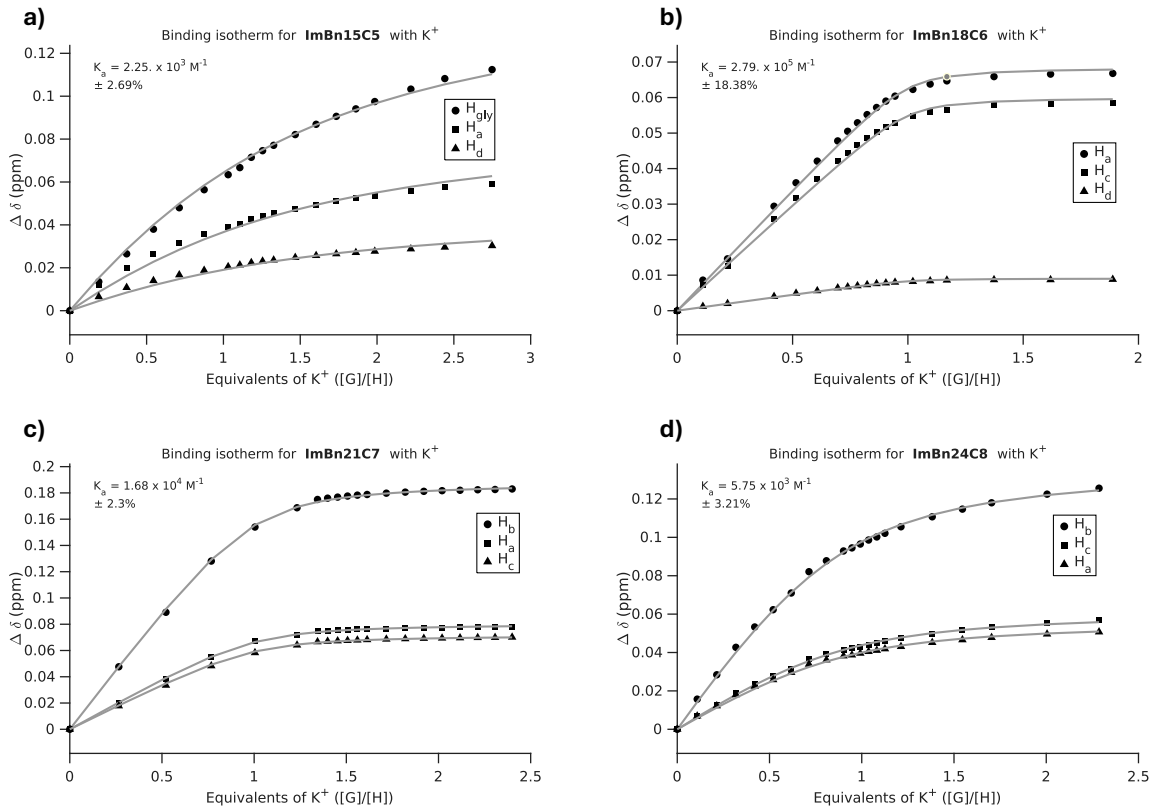

*Figure 42. Binding isotherms of a) **ImBn15C5** (0.54 mM), b) **ImBn18C6** (0.44 mM), c) **ImBn21C7** (1.5 mM), and d) **ImBn24C8** (1.4 mM) with K^+ from one titration trial in MeCN at 20°C. The associated K_a and the ±% error of the fitting to the data points is represented on the graphs.*

The experimental data obtained from the titrations were fit using bindfit on supramolecular.org (Figure 42). From each titration experiment the three protons which exhibit the largest and most consistent shift were selected. Then the absolute change in ppm for the three signals at different equivalences is input into the software. The software will then plot the data points and perform a Nedler and Mead fitting, outputting a K_a for the system, the fitting associated, and an error. Of note, the error given by the software is the percent error of the fit relative to the data points.

It is important to assess the fitting quality of the regression model to the data points. A poor fitting would lead to errors in the calculated K_a value and limit reproducibility. This assessment can be done visually by comparing the fitting to the data points ensuring the fitting follows the titration curve. Another indication of the quality of fitting is the fitting error output by the software.

When a preliminary fitting was done on each system, significant inaccuracies were observed. This led to large error values, poor fitting and significant variation of the K_a between trials. A possible reason for the error was the nominal concentrations for the solution. The presence of water in the sample and the error associated to measuring the samples could lead to significant differences in the nominal concentration versus the actual one. This can lead to big errors in the fitting and the reproducibility, as the equations derived to perform the fitting assumes the description of a real system. To understand whether the nominal concentration was indeed correct quantitative NMR (qNMR) analysis of each sample was performed using an internal standard of trimethoxybenzene added at the end of the titration. It was observed that there was a significant difference between the nominal concentration and the concentration calculated through qNMR (13-15%). Therefore, a correction factor was attributed to each system that reflected the difference in concentration.

Upon applying the correction factor to each system, the binding isotherms on Figure 42 were obtained. Visually, it is clear to see that all the fitting lines follows most of the data points on the binding isotherm. Furthermore, the overall error reported for each system was much smaller than previous, allowing the calculation of a reliable K_a value for each system.

Most concentrations used for the host give $K_a*[H_0]<35$, to ensure that the values obtained were reliable. Keeping $K_a*[H_0]$ low is important as it allows the observation of the evolution of the signal at various aliquots of the guest. Given this value is high it would mean a lot of complexation occurs even at small guest additions, giving poor curvature for the titration curve, leading to poor fitting. Therefore, a lower $K_a*[H_0]$ value gives more reliable values. Only for **ImBn18C6** titration with K^+ values higher than 35 were obtained, therefore more titrations of this system should be performed at lower concentrations.

4.3.4 K_a of Imidazole Macrocycles with K^+ and Na^+

From the binding isotherms constructed using bindfit the various K_a values for each system can be reported and compared. The software reports the K_a in units of M^{-1} as they are derived from concentration-based measurements. However, in Table 1 the K_a values are reported on a log scale to facilitate comparison across systems spanning several orders of magnitude. Furthermore, the logarithmic representation gives a better thermodynamic understanding of the system, as a large ten-fold increase in K_a corresponds to only a relatively small change in binding free energy (≈ 5.7 kJ mol^{-1}).

*Table 1. Final association constants (Log10(K_a)) for macrocycle complexation with K^+ and Na^+ in MeCN at 25°C with different spacer groups. Values are reported as the mean ± standard deviation when available. [a]Values for **18C6** were taken from literature.[2]*

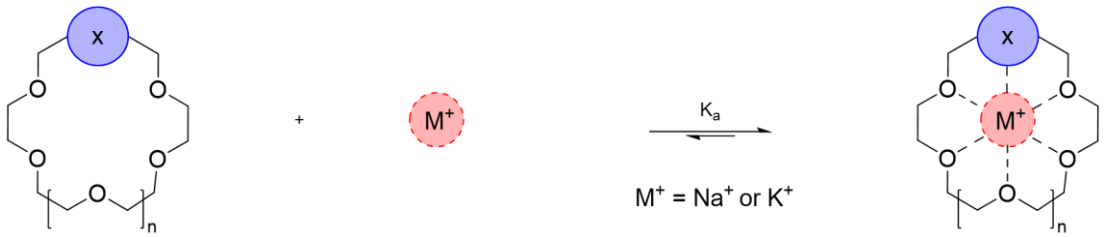

x	Macrocycle	$log_{10}(K_A)$ K^+	Na^+
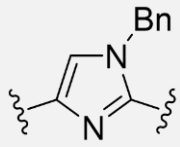	**ImBn15C5**	3.35±0.06	3.19±0.17
	ImBn18C6	5.41±0.05	4.67±0.05
	ImBn21C7	4.23±0.10	3.75±0.07
	ImBn24C8	3.53±0.42	3.23±0.24
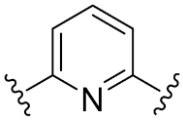	**Py18C6**	4.96±0.10	4.72±0.07
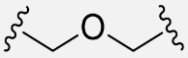	**18C6**	5.72[a]	4.71[a]

Table 1 summarizes the different K_a obtained for each cationic guest and the respective imidazole crown ethers. The K_a for **18C6** was found in literature and the K_a for the pyridine substituted crown ether was obtained by UV-vis titrations in the group in relation to a different project. The **Py18C6** crown ether has a structure analogous to the imidazole crown ether, replacing the imidazole moiety for a pyridine.

Standard deviations (SD) for the values obtained are also provided in Table 1. This is distinct from the fitting errors previously discussed. Rather the SD comes from comparing the log(K_a) value of each individual trial. The SD is indicative of the deviation of the data, for this investigation it is the variation of the data between trials. Most of the SD values are small and fall between 0.05 and 0.10, indicative of small variation and reproducible results.

Comparing the different imidazole crown ethers, there are trends on the binding that can be observed. Initially, it is clear to see that all the imidazole crown ethers bind K^+ better than Na^+. This is expected as the solvation energy for Na^+ is higher than for K^+, making de-solvation and complexation more enthalpically favourable for K^+. The **ImBn18C6** exhibits the best selectivity for K^+, binding it significantly stronger than Na^+. For the imidazole crown ethers, the general binding strength is as follows **ImBn18C6**>**ImBn21C7**>**ImBn24C8**≈**ImBn15C5** (Figure 43a). This is due to the cavity-

cation complementarity, **ImBn18C6** provides the cavity with the best size/geometry match for the studied cations. This allows the oxygen donors to be arranged optimally for strong binding. The binding behaviour observed for the imidazole crown ethers are similar to reported binding behaviour of classical crown ethers.

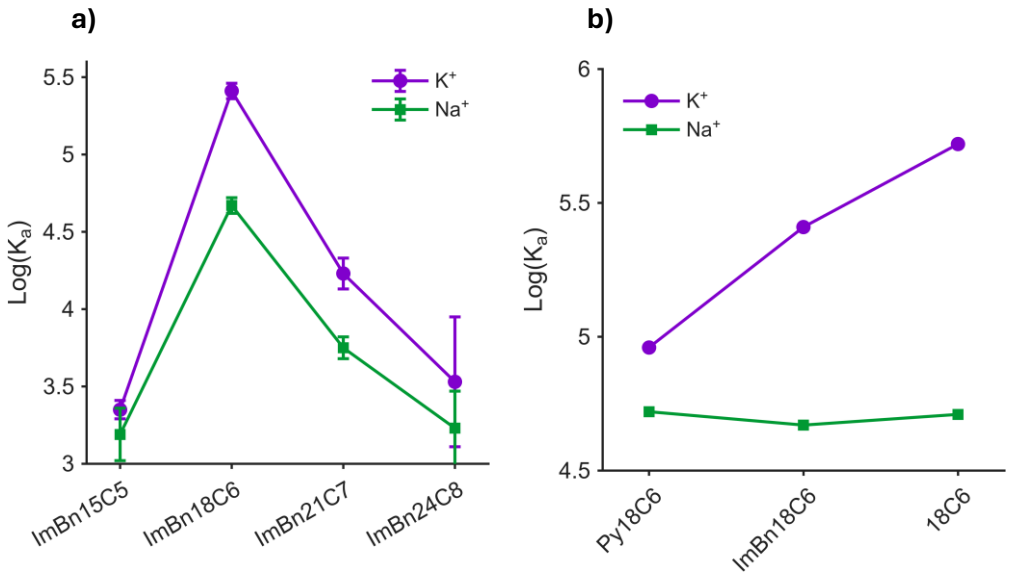

Figure 43. Graphical representation of the K_a values for the different crown ether derivatives in MeCN at 20°C. a) Comparison of K_a for imidazole crown ethers of different sizes with K^+ and Na^+. b) Comparison of K_a for different crown ether derivatives with K^+ and Na^+.

As expected, there are similarities for the binding between all the crown ether derivatives presented on Table 1, such as K^+ preference. However, there are certain differences between the different crown ether scaffolds, notably in the strength of binding. **18C6** binds K^+ the best followed by **ImBn18C6**, and then **Py18C6** (Figure 43b) highlighting the difference a substitution of a -CH_2O- group makes in the binding strength. **18C6** has an extra oxygen which is a hard donor as it is small, electronegative, and poorly polarizable, allowing it to interact strongly with alkali metals given size complementarity. Whereas both **ImBn18C6** and **Py18C6** replace the oxygen donor with a nitrogen. However, the imidazole fragment is more electron rich than the pyridine one, allowing stronger interaction with the cation. The variation of the donor group is most likely the main factor that leads to the patterns observed. However, there are other considerations that may contribute to differences in binding such as solvation and cavity geometry.

4.4 Imidazole Macrocycles for Pseudorotaxanes.

While imidazole incorporation led to alkali metal binding properties similar to traditional crown ethers. However, the enhanced basicity of the imidazole should lead to stronger interactions with ammonium ions, where hydrogen bonding is expected to play a more dominant role.[71] This prompted us to study the interaction with secondary ammonium ions. Given the value of crown ethers for the synthesis of mechanically interlocked architectures, binding of these ions is particularly interesting for the formation of

pseudorotaxanes. These are structures where a secondary ammonium ion is threaded, like an axle, through the macrocycle.

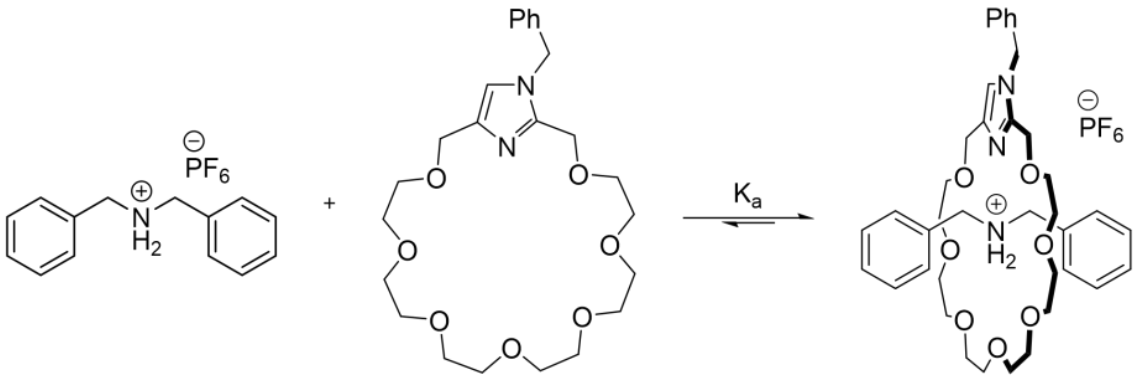

*Figure 44. **ImBn24C8** pseudorotaxane formation with **DBA**.*

Dibenzylammonium hexafluorophosphate, (**DBA·HPF$_6$**) was selected as the model axle as it is well known benchmark which forms threaded pseudorotaxane complexes with various crown ethers. This interaction arises from the protonated ammonium center forming hydrogen bonds with the heteroatoms within the macrocyclic cavity and the overall positive charge is stabilized by ion-dipole interactions. Furthermore, the two benzyl groups provide a linear axle that allows threading through the crown ether cavity. As a result, **DBA·HPF$_6$** forms a reversible yet relatively stable threaded host-guest complex with appropriately sized crown ethers.[72] These features make **DBA·HPF$_6$** a suitable axle for pseudorotaxane formation with **ImBn24C8**.

For a comparison dibenzo-24-crown-8 (**DB24C8**) and a pyridine crown ether (**Py24C8**) were explored for pseudorotaxanes using the same axle. This facilitated the effect of basicity on binding for each macrocycle, as it increases in the order **DB24C8**<**Py24C8**<**ImBn24C8**.

Pseudorotaxane formation was also attempted with **ImBn21C7**. Only minor changes in the ^{1}H NMR spectrum were observed, suggesting acid base interactions between the acidic proton on **DBA** and the basic nitrogen of **ImBn21C7**. The lack of significant complexation-induced shifts indicates that pseudorotaxane formation is unlikely. This suggests that the steric bulk imposed by the benzyl substituents on the axle is too significant to allow threading through macrocycles smaller than **24C8**.[73]

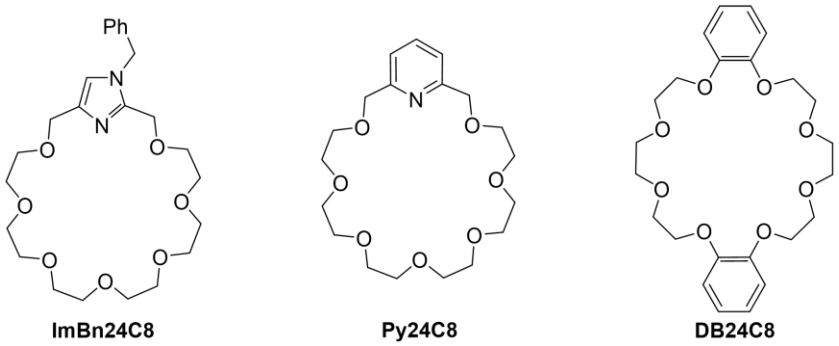

Figure 45. Different crown ethers that were used in the pseudorotaxane system.

Pseudorotaxanes were formed by adding **DBA.HPF$_6$** to a solution of **ImBn24C8** in a 1:1 ratio forming **DBA·HPF$_6$⊂ImBn24C8.** After the system reached equilibrium an ^{1}H NMR was recorded at 20°C in MeCN to examine the interaction between the **DBA.HPF$_6$** axle and **ImBn24C8**. The same was repeated for the other crown ether analogues. To ensure equilibrium was reached a second ^{1}H NMR was recorded 24h later for all systems, no change to the spectra would indicate equilibrium being reached.

An important indication for pseudorotaxane formation is the change in coupling behaviour of the benzylic CH_2 protons of **DBA**. They appear as singlet around 4.25 ppm when uncomplexed (uc) (Figure 48), due to the adjacent ammonium protons exchanging rapidly with the medium, averaging out the coupling. However, when the macrocycle is added to solution the exchange rate is much lower, owing to the hydrogen bonding between the ammonium protons and the coordination sites. This is visible in the spectra as the benzylic CH_2 protons became a second order multiplet. The splitting pattern of the benzylic protons of **DBA.HPF$_6$** upon pseudorotaxane formation with **Py24C8** or **DB24C8** doublet of doublets. However, when the macrocycle **ImBn24C8** is used the apparent splitting pattern for the benzylic protons becomes a more complex ddd-type splitting (Figure 48). The reason for this is the inherent asymmetry of the 2,4-functionalized imidazole within the crown ether, that leads to a directionality of the ring as shown in Figure 46. Therefore, the benzylic CH_2 protons on **DBA** become diastereotopic as if we consider the substitution of either C-H, it would generate not only a chiral center, but also a planar chirality in the molecule.

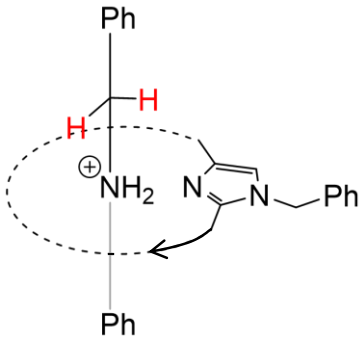

Figure 46. Directionality imposed by the imidazole on the benzylic protons.

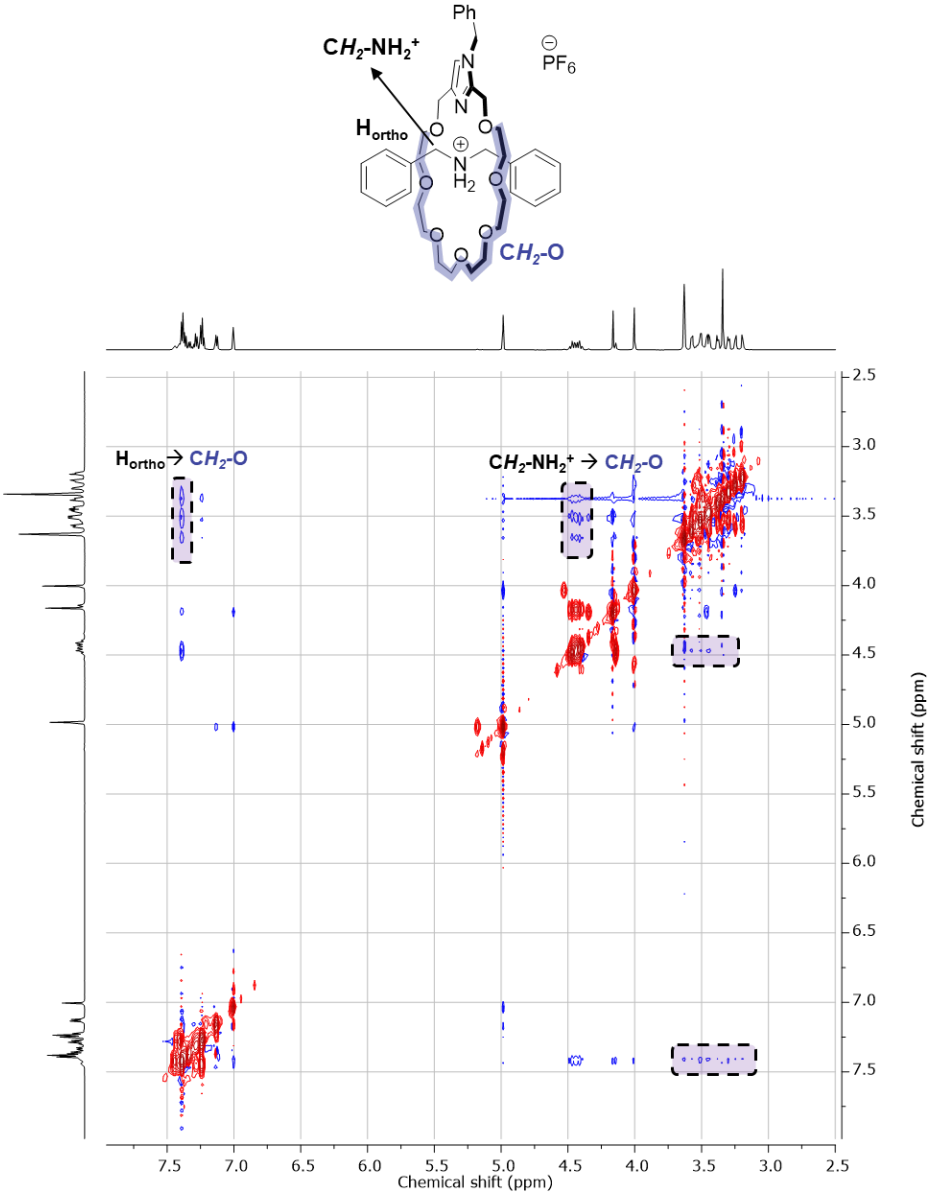

*Figure 47. ^{1}H-^{1}H NOESY spectrum in for a 10 mM 1:1 mixture of **ImBn24C8** and **DBA·HPF$_6$** in MeCN at 20°C. EXSY correlations are in red and NOESY correlations in blue. Important NOESY correlations are highlighted.*

To further prove pseudorotaxane formation ^{1}H-^{1}H NOESY studies were performed. Significant cross peaks between the ortho and benzylic protons of the **DBA** and ether groups of **ImBn24C8** were observed, demonstrating close spatial proximity of the groups (Figure 47). Finally, an HRMS was run on the sample, and the desired m/z values that correspond to the 1:1 complex were observed. All of this gives good evidence of the threading of the axle through the macrocycle cavity to form the pseudorotaxane.

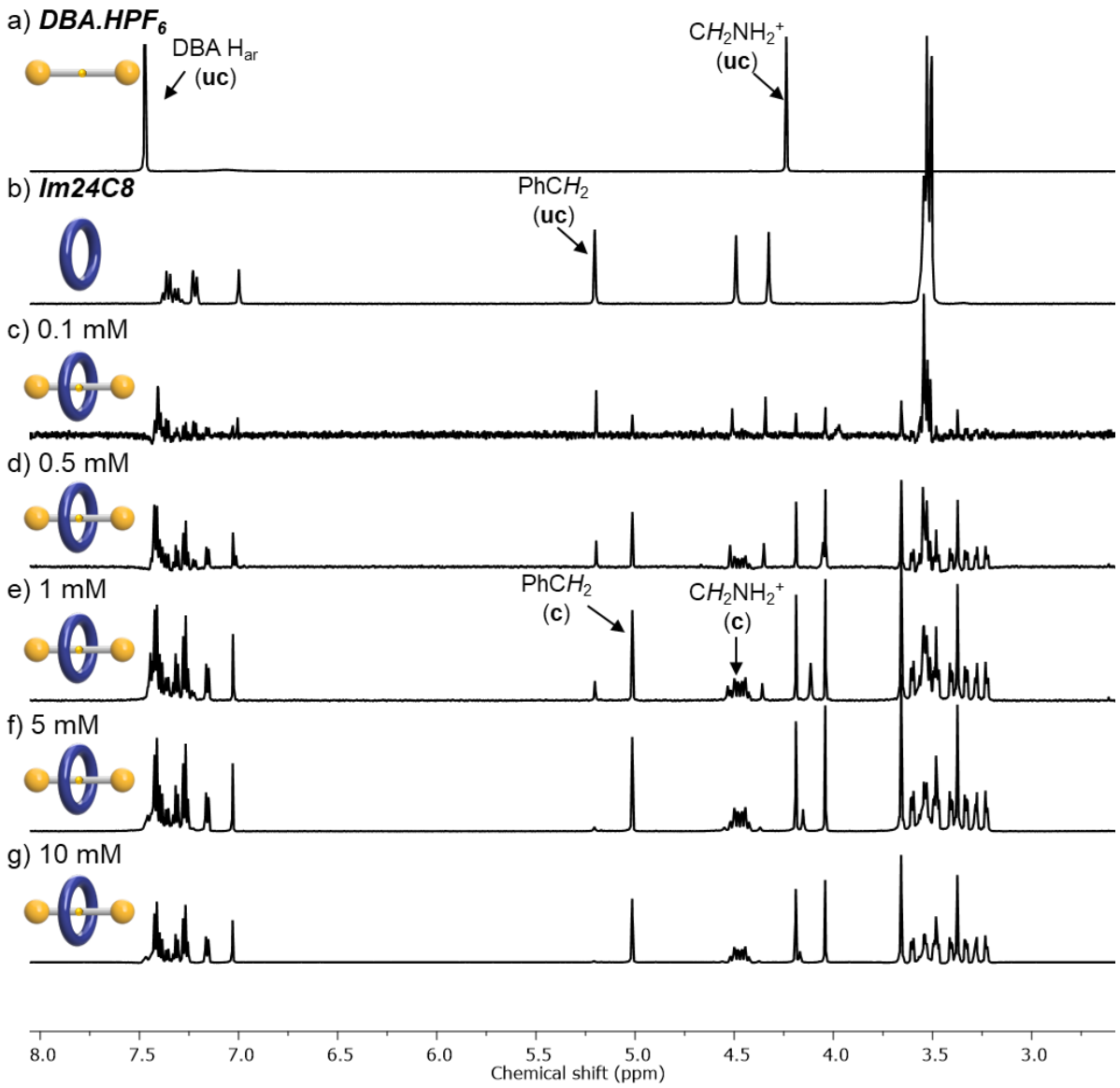

*Figure 48. Partial ^{1}H NMR spectra showing the formation of the **DBA.HPF$_6$⊂ImBn24C8** pseudorotaxane at different concentrations. a) ^{1}H NMR spectra of only **DBA·HPF$_6$**. b) ^{1}H NMR spectra of only **ImBn24C8**. c-g) ^{1}H NMR spectra of a 1:1 mixture of **ImBn24C8** and **DBA·HPF$_6$** at various concentrations in MeCN at 20°C.*

The interaction between the axle and each crown ether derivatives were quantified by reporting the K_a value (Table 2). Slow exchange of the system is observed from the separate resonances for complexed and uncomplexed species (Figure 48). This is because the exchange between complexed and uncomplexed forms is slow compared to the ^{1}H NMR chemical shift timescale. The resonances for the new species were consistent with a 1:1 complex, which is also indicative of pseudorotaxane formation.

As the system is in equilibrium, changing the concentration leads to systematic variation of the degree of complexation and therefore variation in the relative signal intensities. This systematic variation allows the estimation of the K_a through the single-point method. In this method the integrals of the free and complexed species are used to calculate the

concentration of each species in solution.[74] Then these values are used to calculate K_a using 1:1 equilibrium equations presented previously, equations 8-10.

The high K_a value for **DBA·HPF$_6$⊂ImBn24C8** can be seen qualitatively from the ^{1}H NMR spectra, as at a concentration of 5 mM or higher mostly complexed species were observed. In contrast, at this concentration range **DBA·HPF$_6$⊂Py24C8** and **DBA·HPF$_6$⊂DB24C8** systems show complexed and uncomplexed species. Only upon dilution (0.1-1 mM) of the **DBA·HPF$_6$⊂ImBn24C8** system were the peaks for the free and complexed species sufficiently resolved to allow reliable K_a determination.

*Table 2. Association constants (K_a) in M^{-1} for pseudorotaxane formation between **DBA** and various crown ether derivatives.*

Macrocycle	K_a (M^{-1})
DB24C8	347±23
Py24C8	1961±434
ImBn24C8	(1.1±0.3) ×10^4

Table 2 summarizes the calculated K_a value for each pseudorotaxane system explored and the standard deviation. The calculated K_a value of 1.1 × 10^4 M^{-1} for the imidazole crown ether was significantly higher than the other derivatives. This shows that the basicity and the strong hydrogen bond acceptor capabilities of the imidazole group facilitate a strong association. The K_a for **DBA·HPF$_6$⊂ImBn24C8** is among the highest reported K_a for pseudorotaxane formation between a crown ether and a secondary ammonium ion under these conditions.[75] Overall, the pseudorotaxane studies show that the incorporation of an imidazole within a crown ether creates a directional and strong binding. These properties can have important downstream applications when constructing more complex mechanical molecules. For instance, the high association constant can be important to synthesize rotaxanes at a high yield through a capping strategy.

5 Conclusion

The aim of this work was to synthesize a previously unreported imidazole-containing crown ethers and to investigate their binding properties. Developing novel crown ether scaffolds is important as structural modifications can influence binding behaviour such as selectivity, affinity and responsiveness. Such tunable properties can be used for novel applications such as molecular recognition, design of molecular switches and molecular machines.

First a synthetic route was demonstrated to provide access to four imidazole crown ether derivatives varying in cavity size. Cheap and commercially available building blocks are used to get to the imidazole diol (**3**) intermediate in a three-step process with a 36% overall yield. The diol (**3**) was an important intermediate as it could be applied to synthesize other diverse imidazole-based macrocycles through Williamson ether synthesis. A reaction between the functionalized imidazole and polyethylene glycol chains under dilute conditions yielded the final macrocycles. **ImBn15C5, ImBn18C6, ImBn21C7,** and **ImBn24C8** were synthesized through five steps and an overall yield between 2% and 13%.

Following successful synthesis, ^{1}H NMR titrations were performed to get a better understanding of cation binding by the macrocycles. Titrations were performed for each macrocycle with K^+ and Na^+. Most protons within the binding cavity of the macrocycles exhibited a downfield shift consistent with the deshielding due to cation binding. However, the benzylic proton experienced consistent downfield shifts, this was tentatively attributed to the conformational rearrangement occurring upon cation binding. A solid-state crystal structure of **ImBn18C6** complexing K^+ was obtained, which demonstrated the binding. The crystal structure confirmed 1:1 complex and showed the distortion induced by the imidazole.

Using the results obtained from NMR titrations, the association constants were determined, allowing a quantitative comparison of the binding strength. The K_a were determined from nonlinear fitting of the ^{1}H NMR titration data. K_a values could be compared, and it was also compared to reported values of other crown ether derivatives. It was observed that the imidazole crown ethers had similar binding properties to classical crown ethers, notably binding K^+ better than Na^+ and **ImBn18C6** demonstrating the best affinity. However, compared to classical crown ethers the affinity of imidazole crown ethers was slightly lower for alkali metals.

Beyond, alkali metal binding, the presence of an imidazole within the macrocyclic cavity introduces a basic element and a strong hydrogen bond acceptor. This property was used to coordinate secondary ammonium ions to form pseudorotaxanes and exceptionally high K_a values (10^4 M^{-1}) were obtained for the imidazole macrocycles. This is among the highest reported in literature for pseudorotaxane formation under similar conditions, showing the potential of imidazole containing crown ethers for the synthesis of more complex mechanically interlocked architectures.

There were some limitations in the presented work. For the synthetic route the limited solubility of the imidazole diester (**2**) in toluene may have contributed to the decrease in yield. A solvent screen could have increased the yield. The purification of the macrocycles was also challenging due to streaking on the solid phase during column chromatography. Furthermore, the similar Rf values between the desired intramolecular cyclized product and the intermolecular byproduct further complicated purification. The

clean ^{1}H NMR spectra of the crude mixture for some of the reactions, suggests that a lot of product loss occurred during purification. Additionally, the deprotection of the benzyl group, while successful, requires further optimization to improve the yield. A final limitation was for concentrations used for the **ImBn18C6** K^+ titrations, as the K_a*[H_0] values were around 100. This meant that the data was not as reliable as desired due to the poor curvature obtained for the binding isotherms. Therefore, using more dilute concentrations would lead to better data, however the magnitude of binding for **ImBn18C6** with K^+ was unexpected.

6 Perspectives

The significant number of extensions to the work shows the applicability of the crown ethers in other investigations, further enforcing the merit of the work.

A possible perspective for this work is the deprotection of the imidazole, which introduces new properties to the crown ether. This deprotection was attempted during this work. However, due to the poor yields of the reaction the deprotected derivatives were not explored further. Nevertheless, reactivity was achieved demonstrating that obtaining the deprotected derivatives through hydrogenation was possible, but more optimizations must be done for it to be a viable route.

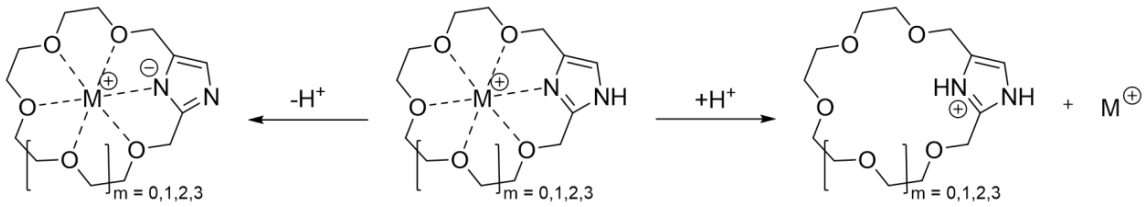

Figure 49. Protonation behaviour following deprotection and the effects on binding.

Given an optimal condition is found to reduce the imidazole, this would lead to the introduction of an active N-H site. This change could lead to the modulation of the guest association with the host via protonation and deprotonation as demonstrated in Figure 49. Furthermore, the active N-H site introduces a strong H-bonding site. Also, upon deprotection the tautomerization of the imidazole can occur, giving it chimeric properties. This means depending on the guest it can act as an H-bond donor or acceptor. All of this could lead to important applications in molecular switches, ion transport, and sensor.

Another interesting application would be to explore the coordination of the imidazole crown ethers with transition metals. As detailed previously a nitrogen is a softer donor than oxygen making it more suitable for transition metal coordination. Nitrogen is also more directional, less electronegative and donates electron density more readily.[58] This donation by nitrogen leads to better orbital overlap with transition metals, giving more

covalent type bonding, which can lead to stronger binding. Therefore, it would be pertinent to explore these systems for transition metals such as Cu^{2+}, Zn^{2+}, Ni^{2+} or Co^{2+}. This could lead to novel binding modes, which could have downstream applications in host-guest chemistry.

Associated to the previous perspective is applying the synthesized imidazole crown ethers to mimic enzyme active sites. An imidazole is a relevant group in biological systems, especially in metalloproteins. A lot of these proteins incorporate an imidazole motif to bind a copper center, leading to strong complexation.[77]

Interestingly, this is related to the origin of this project where attempts were made to mimic LPMOs. To this end mimic an imidazole crown ether was needed for a rotaxane based model of the LPMO active site. Generally, biological metal coordination results from different functional groups being arranged in a precise fashion by the protein scaffold. Using small molecule systems to mimic the coordination requires a linker between each group, leading to rigidity. Whereas using a rotaxane like structure would lead to more conformational freedom mimicking the protein scaffold better. Therefore, the design of an imidazole macrocycle can have important applications in mimicking biological mechanisms (Figure 50).

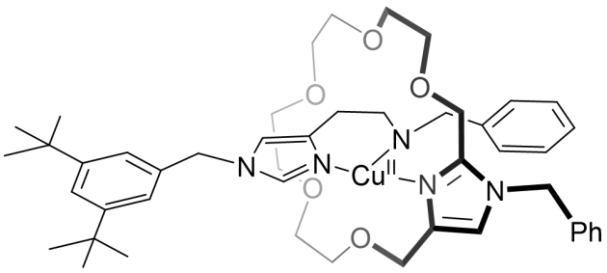

Figure 50. Possible use of the imidazole crown ether to mimic the LPMO active site.

References

(1) Qi, Z.; Qin, Y.; Wang, J.; Zhao, M.; Yu, Z.; Xu, Q.; Nie, H.; Yan, Q.; Ge, Y. The Aqueous Supramolecular Chemistry of Crown Ethers. *Front. Chem.* **2023**, *11*. https://doi.org/10.3389/fchem.2023.1119240.

(2) Izatt, R. M.; Bradshaw, J. S.; Nielsen, S. A.; Lamb, J. D.; Christensen, J. J.; Sen, D. Thermodynamic and Kinetic Data for Cation-Macrocycle Interaction. *Chem. Rev.* **1985**, *85* (4), 271–339. https://doi.org/10.1021/cr00068a003.

(3) Sakuma, R.; Hirata, K.; Lisy, J. M.; Fujii, M.; Ishiuchi, S. Unbuckling the 18-Crown-6 Ether Belt Around Metal Ions: Forging the Connection to the Condensed Phase. *J. Am. Chem. Soc.* **2025**, *147* (1), 45–50. https://doi.org/10.1021/jacs.4c12036.

(4) Das, P. P.; Srivastava, A. K. SYNTHESIS AND APPLICATIONS OF FUNCTIONALIZED CROWN ETHERS. In *IIP Series*; Khan, Dr. A. H., Shukla, Dr. M., Karunakaran, Dr. M., Sahu, Dr. S., Jacob, Dr. G. A., S., Dr. S., Jadhav, Dr. S. B., Dey, B., Chelike, D. K., Das, Dr. S., M, Dr. S. G., Chaudhuri, A., Desai, Dr. N. D., Kamble, Dr. G. S., Sharma, Dr. J., Sarvalkar, P. D., Nandi, S. S., Dash, S., Nagpal, Prof. Dr. A., Eds.; Iterative International Publishers (IIP), 2022; Vol. 2, pp 1–29. https://doi.org/10.58532/V2BS12P1CH1.

(5) Nakamura, K.; Nishiyama, S.; Tsuruya, S.; Masai, M. Oxidation of Catechol with KMnO4 by Using Crown Ethers as Phase Transfer Catalysts. *J. Mol. Catal.* **1994**, *93* (2), 195–210. https://doi.org/10.1016/0304-5102(94)00074-3.

(6) Xue, M.; Yang, Y.; Chi, X.; Yan, X.; Huang, F. Development of Pseudorotaxanes and Rotaxanes: From Synthesis to Stimuli-Responsive Motions to Applications. *Chem. Rev.* **2015**, *115* (15), 7398–7501. https://doi.org/10.1021/cr5005869.

(7) Di Stefano, S.; Capocasa, G.; Mandolini, L. Supramolecular Catalysts Featuring Crown Ethers as Recognition Units. *Eur. J. Org. Chem.* **2020**, *2020* (23), 3340–3350. https://doi.org/10.1002/ejoc.201901914.

(8) Liu, J.; Zhang, X.; Lu, X.; Li, Q.; Xue, Z.; Zhang, Q.; Wu, G.; Xia, W. Review on Extraction and Separation of Valuable Metal Ions from Aqueous Solution by Crown Ether. *Chin. J. Chem. Eng.* **2025**, *85*, 217–227. https://doi.org/10.1016/j.cjche.2025.02.027.

(9) Amano, S.; Fielden, S. D. P.; Leigh, D. A. A Catalysis-Driven Artificial Molecular Pump. *Nature* **2021**, *594* (7864), 529–534. https://doi.org/10.1038/s41586-021-03575-3.

(10) Pedersen, C. J. The Discovery of Crown Ethers (Noble Lecture). *Angew. Chem. Int. Ed. Engl.* **1988**, *27* (8), 1021–1027. https://doi.org/10.1002/anie.198810211.

(11) Pedersen, C. J. Cyclic Polyethers and Their Complexes with Metal Salts. *J. Am. Chem. Soc.* **1967**, *89* (10), 2495–2496. https://doi.org/10.1021/ja00986a052.

(12) Gibson, H. W.; Wang, H.; Bonrad, K.; Jones, J. W.; Slebodnick, C.; Zackharov, L. N.; Rheingold, A. L.; Habenicht, B.; Lobue, P.; Ratliff, A. E. Regioselective Routes to Disubstituted Dibenzo Crown Ethers and Their Complexations. *Org. Biomol. Chem.* **2005**, *3* (11), 2114–2121. https://doi.org/10.1039/B503072M.

(13) Pedersen, C. J. Cyclic Polyethers and Their Complexes with Metal Salts. *J. Am. Chem. Soc.* **1967**, *89* (26), 7017–7036. https://doi.org/10.1021/ja01002a035.

(14) Ouelette, R. J.; Rawn, J. D. Ethers and Epoxides. In *Organic Chemistry Study Guide*; 2015; pp 277–297. https://doi.org/10.1016/B978-0-12-801889-7.00016-9.

(15) Pedersen, C. J. Macrocyclic Polyethers: Dibenzo-18-Crown-6 Polyether and Dicyclohexyl-18-Crown-6 Polyether. In *Organic Syntheses*; John Wiley & Sons, Ltd, 2003; pp 66–66. https://doi.org/10.1002/0471264180.os052.13.

(16) Ruggli, P. Über Einen Ring Mit Dreifacher Bindung. *Justus Liebigs Ann. Chem.* **1912**, *392* (1), 92–100. https://doi.org/10.1002/jlac.19123920106.

(17) Methoden Der Organischen Chemie (Houben-Weyl). 4th Ed. Vol. 4, Part 2. Allgemeine Chemische Methoden. B. Helferich. *J. Am. Pharm. Assoc.* **1955**, *44* (6), 385–385. https://doi.org/10.1002/jps.3030440630.

(18) Gokel, G. W.; Negin, S.; Cantwell, R. Crown Ethers. In *Comprehensive Supramolecular Chemistry II*; Elsevier, 2017; pp 3–48. https://doi.org/10.1016/B978-0-12-409547-2.12519-3.

(19) Sivaram, S. The Ziegler Catalysts: Serendipity or Systematic Research? *Resonance* **2017**, *22* (11), 985–1006. https://doi.org/10.1007/s12045-017-0567-x.

(20) Gokel, G. W. Cation Binding by Crown Ethers. In *Comprehensive Supramolecular Chemistry II*; Elsevier, 2017; pp 203–216. https://doi.org/10.1016/B978-0-12-409547-2.05615-8.

(21) Busch, D. H. Structural Definition of Chemical Templates and the Prediction of New and Unusual Materials. In *The Pedersen Memorial Issue*; Izatt, R. M., Bradshaw, J. S., Eds.; Springer Netherlands: Dordrecht, 1992; pp 389–395. https://doi.org/10.1007/978-94-011-2532-1_25.

(22) Kanagaraj, K.; Alagesan, M.; Inoue, Y.; Yang, C. Solvation Effects in Supramolecular Chemistry. In *Comprehensive Supramolecular Chemistry II*; Elsevier, 2017; pp 11–60. https://doi.org/10.1016/B978-0-12-409547-2.12481-3.

(23) Atkins, P. W.; De Paula, J.; Keeler, J. *Atkins' Physical Chemistry*, Eleventh edition.; Oxford University Press: Oxford, United Kingdom ; New York, NY, 2018.

(24) Buckingham, A. D.; Del Bene, J. E.; McDowell, S. A. C. The Hydrogen Bond. *Chem. Phys. Lett.* **2008**, *463* (1), 1–10. https://doi.org/10.1016/j.cplett.2008.06.060.

(25) Hancock, R. D. A Molecular Mechanics Study of the Selectivity of Crown Ethers for Metal Ions on the Basis of Their Size. *J. Incl. Phenom. Mol. Recognit. Chem.* **1994**, *17* (1), 63–80. https://doi.org/10.1007/BF00708001.

(26) Izatt, R. M.; Bradshaw, J. S.; Nielsen, S. A.; Lamb, J. D.; Christensen, J. J.; Sen, D. Thermodynamic and Kinetic Data for Cation-Macrocycle Interaction. *Chem. Rev.* **1985**, *85* (4), 271–339. https://doi.org/10.1021/cr00068a003.

(27) Nasri, F. A Review of the Thermodynamics of Complexation of Crown Ethers With Metal Ion. *J. Adv. Environ. Health Res.* **2022**, *10*, 263–272. https://doi.org/10.32598/JAEHR.10.4.1218.

(28) Kuo, P.-L.; Miki, M.; Ikeda, I.; Okahara, M. New Synthesis of N-Alkyl Monoaza Crown Ethers. *Tetrahedron Lett.* **1978**, *19* (44), 4273–4276. https://doi.org/10.1016/S0040-4039(01)95200-1.

(29) Schultz, R. A.; Dishong, D. M.; Gokel, G. W. Crown-Cation Complex Effects. 15. Lariat Ethers. 4. Chain Length and Ring Size Effects in Macrocyclic Polyethers Having Neutral Donor Groups on Flexible Arms. *J. Am. Chem. Soc.* **1982**, *104* (2), 625–626. https://doi.org/10.1021/ja00366a047.

(30) Arnold, K. A.; Viscariello, A. M.; Kim, M.; Gandour, R. D.; Fronczek, F. R.; Gokel, G. W. 4,13-Diaza-18-Crown-6 Derivatives Having Pi-Donor-Group-Sidearms: Correlation of Thermodynamics and Solid State Structures. *Tetrahedron Lett.* **1988**, *29* (25), 3025–3028. https://doi.org/10.1016/0040-4039(88)85076-7.

(31) Gokel, M. R.; McKeever, M.; Meisel, J. W.; Negin, S.; Patel, M. B.; Yin, S.; Gokel, G. W. Crown Ethers Having Side Arms: A Diverse and Versatile Supramolecular Chemistry. *J. Coord. Chem.* **2021**, *74* (1–3), 14–39. https://doi.org/10.1080/00958972.2021.1878352.

(32) Liu, Y.; Han, J.-R.; Duan, Z.-Y.; Zhang, H.-Y. Synthesis of Double-Armed Benzo-15-Crown-5 and Their Complexation Thermodynamics with Alkali Cations. *J. Incl. Phenom. Macrocycl. Chem. - J INCL PHENOM MACROCYCL CHEM* **2005**, *52*, 229–235. https://doi.org/10.1007/s10847-004-7241-0.

(33) Choi, C. M.; Heo, J.; Kim, N. J. Binding Selectivity of Dibenzo-18-Crown-6 for Alkali Metal Cations in Aqueous Solution: A Density Functional Theory Study Using a Continuum Solvation Model. *Chem. Cent. J.* **2012**, *6*, 84. https://doi.org/10.1186/1752-153X-6-84.

(34) Expert, chem. Production of Macrocyclic Polyether Benzo-15-Crown-5 and Its Functional Derivatives. *Orient. J. Chem.* **2017**, *33* (4), 1689–1697.

(35) Stoddart, J. F. Mechanically Interlocked Molecules (MIMs)—Molecular Shuttles, Switches, and Machines (Nobel Lecture). *Angew. Chem. Int. Ed.* **2017**, *56* (37), 11094–11125. https://doi.org/10.1002/anie.201703216.

(36) Sluysmans, D.; Stoddart, J. F. The Burgeoning of Mechanically Interlocked Molecules in Chemistry. *Trends Chem.* **2019**, *1* (2), 185–197. https://doi.org/10.1016/j.trechm.2019.02.013.

(37) Harrison, I. Thomas.; Harrison, Shuyen. Synthesis of a Stable Complex of a Macrocycle and a Threaded Chain. *J. Am. Chem. Soc.* **1967**, *89* (22), 5723–5724. https://doi.org/10.1021/ja00998a052.

(38) Kwamen, C.; Niemeyer, J. Functional Rotaxanes in Catalysis. *Chem. Weinh. Bergstr. Ger.* **2021**, *27* (1), 175–186. https://doi.org/10.1002/chem.202002876.

(39) *Stilbene-Cross-Linked Pillar[5]arene-Based Polymer for Efficient Iodine Vapor Capture and Adsorption from Water | ACS Applied Polymer Materials*. https://pubs.acs.org/doi/10.1021/acsapm.4c00073 (accessed 2026-05-26).

(40) Li, X.-L.; Niu, K.-K.; Wang, F.-D.; Yao, X.-Y.; Liu, H.; Yu, S.; Xing, L.-B. A Photosensitive Cationic Macrocycle Based on Triphenylamine as Photocatalysts for Selective Photooxidation of Phosphines, Styrenes, and Hydroazobenzenes. *ACS Sustain. Chem. Eng.* **2024**, *12* (10), 4236–4244. https://doi.org/10.1021/acssuschemeng.3c08325.

(41) Wu, Y.; Yang, J.; Zhuang, S.-Y.; Yu, S.-B.; Zong, Y.; Liu, Y.-Y.; Wu, G.; Qi, Q.-Y.; Wang, H.; Tian, J.; Zhou, W.; Ma, D.; Zhang, D.-W.; Li, Z.-T. Macrocycles and Acyclic Cucurbit[n]Urils as Pseudo[2]Catenane Partners for Long-Acting Neuromuscular Blocks and Rapid Reversal In Vivo. *J. Med. Chem.* **2024**, *67* (3), 2176–2187. https://doi.org/10.1021/acs.jmedchem.3c02110.

(42) Liu, G.; Tian, C.; Fan, X.; Dang, Y.; Qin, J.; Liu, L.; Cao, Z.; Jiang, S. Dual-Stimulus-Driven Dynamically Controllable [3]Rotaxane with Tunable Organic Room-Temperature Phosphorescence. *Org. Lett.* **2023**, *25* (48), 8761–8765. https://doi.org/10.1021/acs.orglett.3c03804.

(43) Alene, D. Y.; Srinivasadesikan, V.; Lin, M.-C.; Chung, W.-S. Construction of Mechanically Interlocked Fluorescence Photoswitchable [2]Rotaxane with Aggregation-Induced Emission and Molecular Shuttling Behaviors. *J. Org. Chem.* **2023**, *88* (9), 5530–5542. https://doi.org/10.1021/acs.joc.3c00077.

(44) Thibeault, D.; Morin, J.-F. Recent Advances in the Synthesis of Ammonium-Based Rotaxanes. *Molecules* **2010**, *15* (5), 3709–3730. https://doi.org/10.3390/molecules15053709.

(45) Saura, S., A. Synthesis of 'Impossible' Rotaxanes. *Chem. – Eur. J.* **2024**, *30* (19), e202304025. https://doi.org/10.1002/chem.202304025.

(46) Chiu, C.-W.; Lai, C.-C.; Chiu, S.-H. "Threading-Followed-by-Swelling": A New Protocol for Rotaxane Synthesis. *J. Am. Chem. Soc.* **2007**, *129* (12), 3500–3501. https://doi.org/10.1021/ja069362i.

(47) Iwamoto, H.; Yawata, Y.; Fukazawa, Y.; Haino, T. Highly Efficient Synthesis of [3]Rotaxane Assisted by Preorganisation of Pseudorotaxane Using Bis(Crown Ether)s. *Supramol. Chem.* **2010**, *22*, 815–826. https://doi.org/10.1080/10610278.2010.514611.

(48) Fielden, S. D. P. Crown Ether Active Template Synthesis of Rotaxanes. *ChemSystemsChem* **2024**, *6* (2), e202300048. https://doi.org/10.1002/syst.202300048.

(49) Sakata, Y.; Ogura, T.; Akine, S. Efficient Formation of [3]Pseudorotaxane Based on Cooperative Complexation of Dibenzo-24-Crown-8 with Diphenylviologen Axle. *Chem. Commun.* **2020**, *56* (62), 8735–8738. https://doi.org/10.1039/D0CC03131C.

(50) Peñaranda-Navarro, R.; Collados-Salmeron, M.; Carrilero-Flores, E.; Saura-Sanmartin, A. Molecular Release by the Rotaxane and Pseudorotaxane Approach. *Chem. – Eur. J.* **2025**, *31* (23), e202500350. https://doi.org/10.1002/chem.202500350.

(51) J.Bruns, C.; Stoddart, J. F. Molecular Switches and Machines with Mechanical Bonds. In *The Nature of the Mechanical Bond*; John Wiley & Sons, Ltd, 2016; pp 555–733. https://doi.org/10.1002/9781119044123.ch6.

(52) Weber, E.; Vögtle, F. Selective Inclusion of Alcohols with a New Pyridino Crown. *Angew. Chem. Int. Ed. Engl.* **1980**, *19* (12), 1030–1032. https://doi.org/10.1002/anie.198010301.

(53) Redd, J. T. Y.; Bradshaw, J. S.; Huszthy, P.; Izatt, R. M. Synthesis and Complexation Properties of Pyrimidine-Derived Crown Ether Ligands. *J. Heterocycl. Chem.* **1998**. https://doi.org/10.1002/jhet.5570350101.

(54) Song, H.-C.; Bradshaw, J.; Chen, Y.-W.; Xue, G.-P.; Li, W.-M.; Krakowiak, K.; Savage, P.; Xu, Z.-L.; Izatt, R. Synthesis of New Crown Ethers Containing Appended Pyridine, 10-

Hydroxybenzoquinoline, 8-Hydroxyquinoline and 2-Amino-1-Hydroxybiphenyl Sidearms. *Supramol. Chem.* **2002**, *14*, 263–269. https://doi.org/10.1080/10610270290026176.

(55) Li, Y.; Echegoyen, L.; Martinez-Diaz, M. V.; De Mendoza, J. Enantiometric Recognition of Organic Ammonium Salts by Chiral Dialkyl-Substituted Triazole-18-Crown-6-Ligands. *J. Org. Chem.* **1991**. https://doi.org/10.1021/jo00013a022.

(56) Staveren, C.; den hertog, H.; Reinhoudt, D.; Uiterwijk, J.; Kruise, L.; Harkema, S. Syntheses and Crystal Structures of 'Encapsulated' Guanidinium Complexes of 27-Membered Macrocyclic Ligands. *J Chem Soc Chem Commun* **1984**, 1409–1411. https://doi.org/10.1039/C39840001409.

(57) Binauld, S.; Hawker, C. J.; Fleury, E.; Drockenmuller, E. A Modular Approach to Functionalized and Expanded Crown Ether Based Macrocycles Using Click Chemistry. *Angew. Chem. Int. Ed.* **2009**, *48* (36), 6654–6658. https://doi.org/10.1002/anie.200903156.

(58) Pearson, R. G. Hard and Soft Acids and Bases. *J. Am. Chem. Soc.* **1963**, *85* (22), 3533–3539. https://doi.org/10.1021/ja00905a001.

(59) Zimmerman, S. C.; Cramer, K. D.; Galan, A. A. Synthesis of 2,4(5)-Bis(Hydroxymethyl)Imidazoles and 2,4(5)-Bis[(2-Hydroxyethoxy)Methyl]Imidazoles. Precursors of 2,4(5)-Connected Imidazole Crown Ethers. *J. Org. Chem.* **1989**, *54* (6), 1256–1264. https://doi.org/10.1021/jo00267a008.

(60) Wagner-Wysiecka, E.; Jamrógiewicz, M.; Fonari, M. S.; Biernat, J. F. Azomacrocyclic Derivatives of Imidazole: Synthesis, Structure, and Metal Ion Complexation Properties. *Tetrahedron* **2007**, *63* (21), 4414–4421. https://doi.org/10.1016/j.tet.2007.03.095.

(61) Llinàs, M. C.; Farran, J.; Capparelli, M. V.; Anguera, G.; Sánchez-García, D.; Teixidó, J.; Borrós, S. Synthesis and Anion Binding Studies of a New Crown Ether Containing 2,2'-Biimidazole. *Tetrahedron Lett.* **2014**, *55* (33), 4667–4670. https://doi.org/10.1016/j.tetlet.2014.06.072.

(62) Wagner-Wysiecka, E.; Luboch, E.; Kowalczyk, M.; Biernat, J. F. Chromogenic Macrocyclic Derivatives of Azoles—Synthesis and Properties. *Tetrahedron* **2003**, *59* (24), 4415–4420. https://doi.org/10.1016/S0040-4020(03)00618-5.

(63) Zimmerman, S. C.; Cramer, K. D. Stereoelectronic Effects at Carboxylate: A Syn-Oriented Model for the Histidine-Aspartate Couple in Enzymes. *J. Am. Chem. Soc.* **1988**, *110* (17), 5906–5908. https://doi.org/10.1021/ja00225a056.

(64) Galiński, B.; Wagner-Wysiecka, E. Macrocyclic Derivatives of Imidazole as Chromoionophores for Bismuth(III)/Lead(II) Pair. *Sens. Actuators B Chem.* **2024**, *399*, 134798. https://doi.org/10.1016/j.snb.2023.134798.

(65) Branco, P. S.; Prabhakar, S.; Lobo, A. M.; Williams, D. J. Reactions of Hydroxylamines with Ethyl Cyanoformate. Preparation of Aminonitrones and Their Synthetic Applications. *Tetrahedron* **1992**, *48* (30), 6335–6360. https://doi.org/10.1016/S0040-4020(01)88224-7.

(66) Xiao, T.; Wang, J.; Shen, Y.; Bao, C.; Li, Z.-Y.; Sun, X.-Q.; Wang, L. Preparation of a Fixed-Tetraphenylethylene Motif Bridged Ditopic Benzo-21-Crown-7 and Its Application for Constructing AIE Supramolecular Polymers. *Chin. Chem. Lett.* **2021**, *32* (4), 1377–1380. https://doi.org/10.1016/j.cclet.2020.10.037.

(67) Groom, C.; Bruno, I.; Lightfoot, M.; Ward, S. The Cambridge Structural Database. *Acta Crystallogr. Sect. B* **2016**, *72*, 171–179. https://doi.org/10.1107/S2052520616003954.

(68) Moaven, S.; Griend, D. A. V.; W. Johnson, D.; D. Pluth, M. Expanding the Toolbox for Supramolecular Chemistry: Probing Host–Guest Interactions and Binding with in Situ FTIR Spectroscopy. *Chem. Sci.* **2025**, *16* (23), 10282–10288. https://doi.org/10.1039/D5SC01329A.

(69) Pastor, A.; Martínez-Viviente, E. NMR Spectroscopy in Coordination Supramolecular Chemistry: A Unique and Powerful Methodology. *Coord. Chem. Rev.* **2008**, *252* (21), 2314–2345. https://doi.org/10.1016/j.ccr.2008.01.025.

(70) Thordarson, P. Determining Association Constants from Titration Experiments in Supramolecular Chemistry. *Chem. Soc. Rev.* **2011**, *40* (3), 1305–1323. https://doi.org/10.1039/C0CS00062K.

(71) J, S. R.; B, M. R. Interactions of Histidine and Other Imidazole Derivatives with Transition Metal Ions in Chemical and Biological Systems. *Chem Rev* **1974**, *74* (4), 471–517.

(72) Dasgupta, S.; Wu, J. Formation of [2]Rotaxanes by Encircling [20], [21] and [22]Crown Ethers onto the Dibenzylammonium Dumbbell. *Chem. Sci.* **2012**, *3* (2), 425–432. https://doi.org/10.1039/C1SC00613D.

(73) Tokunaga, Y.; Yoshioka, M.; Nakamura, T.; Goda, T.; Nakata, R.; Kakuchi, S.; Shimomura, Y. Do Dibenzo[22–30]Crown Ethers Bind Secondary Ammonium Ions to Form Pseudorotaxanes? *Bull. Chem. Soc. Jpn.* **2007**, *80* (7), 1377–1382. https://doi.org/10.1246/bcsj.80.1377.

(74) Adrian, J. C. Jr.; Wilcox, C. S. Chemistry of Synthetic Receptors and Functional Group Arrays. 15. The Effects of Added Water on Thermodynamic Aspects of Hydrogen Bond Based Molecular Recognition in Chloroform. *J. Am. Chem. Soc.* **1991**, *113* (2), 678–680. https://doi.org/10.1021/ja00002a048.

(75) Chang, T. *et al. Ammonium Ion Binding with Pyridine-Containing Crown Ethers*. *Org. Lett.* **2**, 2947–2950 (2000)..

(76) Li, Z.; Bhowmik, S.; Sagresti, L.; Brancato, G.; Smith, M.; Benson, D. E.; Li, P.; Merz, K. M. Jr. Simulating Metal-Imidazole Complexes. *J. Chem. Theory Comput.* **2024**, *20* (15), 6706–6716. https://doi.org/10.1021/acs.jctc.4c00581.

Supporting Information

The full SI is only provided in the electronic version.

General Information

All commercial reagents and solvents were obtained from Sigma-Aldrich, Acros Organics, BLDpharm or Fluorochem, and were used as purchased without further purification unless otherwise stated.

Dry solvents were obtained by standard procedures according to D. D. Perrin and D. R. Perrin, Purification of Laboratory Chemicals. Tetrahydrofuran was purified by distillation from benzophenone ketyl radical. Dichloromethane, toluene, trimethylamine, N,N-diisopropylethylamine and trimethylsilyl chloride were purified by distillation from calcium hydride.

Analytical thin layer chromatography (TLC) were carried out on Merck Millipore F254 silica gel 60 plates (210-270 µm thickness, aluminium supported) and on Merck Millipore neutral aluminium oxide F_{254} plates (200 µm thickness, aluminium supported). The plates were visualized using ultra-violet light (254 nm), KMnO4 or I2. Flash column chromatography was carried out on ROCC silica gel 60Å (230-400 Mesh).

Proton nuclear magnetic resonance (^{1}H NMR) spectra were recorded using JEOL JNM-ECZL600G (600 MHz) or NM-70020R4S1 (400 MHz) spectrometers. Carbon nuclear magnetic resonance (^{13}C NMR) spectra were recorded using JEOL JNM-ECZL600G (150 MHz) or NM-70020R4S1 (400 MHz) spectrometers. Chemical shifts (δ) are reported in parts per million (ppm) relative to residual solvent peaks: ^{1}H ($CDCl_3$ δppm = 7.26, DMSO-d_6 δppm = 2.50, D_2O δppm = 4.79, CD_3CN δppm = 1.94), ^{13}C (DMSO-d_6 δppm = 39.5, $CDCl_3$ δppm =77.16, CD_3CN δppm = 118.26). Coupling constants are reported in Hertz (Hz). Splitting patterns are designed as: s (singlet), d (doublet), t (triplet), q (quartet) and m (multiplet). Deuterated solvents were purchased from Eurisotop.

Mass spectra were recorded by the Mass Spectrometry Service of the “asm” platform from the Institute of Condensed Matter and Nanosciences (IMCN) at UCLouvain, using Q-Tof Waters Synapt XS spectrometers with a Thermo Orbitrap Exactive device. The values are given in Dalton.

UV/Visible experiments were performed on a VWR UV-1600PC Scanning Spectrophotometer equipped with Deuterium/Tungsten Halogen Lamp.

Synthesis

Synthesis of (Z)-1-amino-N-benzyl-2-ethoxy-2-oxoethan-1-imine oxide **(1)**

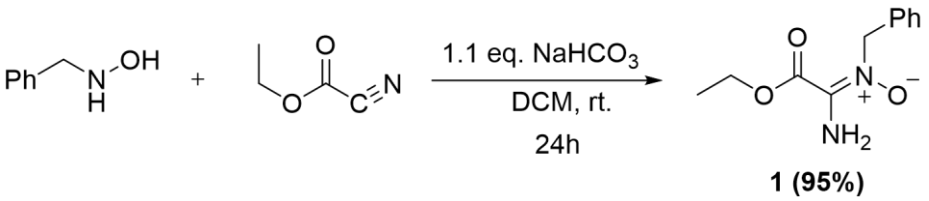

1 (95%)

A flame dried round bottom flask was loaded with N-benzylhydroxylamine (7.09 g, 44.4 mmol, 1.1 eq.) and sodium bicarbonate (3.73 g, 44.4 mmol, 1.1 eq.) under Ar. Dry DCM (200 mL) was added and the mixture was allowed to stir for 30 min at room temperature. Then ethyl carbonocyanidate (4 g, 40.4 mmol, 1 eq.) was added and the reaction mixture was allowed to stir overnight. The reaction was then filtered, and the solvent was removed via rotary evaporation, obtaining **1**(8.5 g, 95%) as a yellow oil which was used without further purification.

^{1}HNMR (400 MHz, CHLOROFORM-*D*) δ 7.48 – 7.27 (m, 6H), 5.50 (s, 2H), 4.37 (q, *J* = 7.1 Hz, 2H), 1.37 (t, *J* = 7.2 Hz,3H).

HRMS (ESI) m/z: $[M + H]^+$ calcd for $C_{11}H_{15}N_2O_3^+$ 223.1077; found 223.1078

Synthesis of 2-ethyl 4-methyl 1-benzyl-1H-imidazole-2,4-dicarboxylate **(2)**

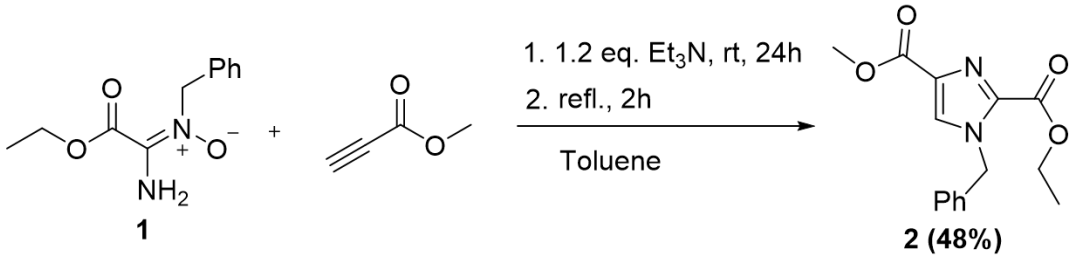

2 (48%)

Compound **1** (4.5 g, 20.2 mmol, 1 eq.) was charged into a round bottom flask and dissolved in toluene (400 mL). Triethylamine (2.46 g, 24.3 mmol, 1.2 eq.) was added and the reaction was placed under Ar atmosphere and allowed to stir for 30 min at room temperature. Methyl propiolate (2.04 g, 24.3 mmol, 1.2 eq.) was added and the reaction was allowed to stir overnight at room temperature. The reaction was then heated to reflux for 2 hours and then the solvent was removed via rotary evaporation. The product as purified via column chromatography (EtOAc:Hexane, 60:40) followed by a recrystallisation using hot Et_2O, affording **2**(2.8 g, 20.2 mmol, 48%) as a white crystalline powder.

^{1}H NMR (400 MHz, CHLOROFORM-D) δ 7.68 (s, 1H), 7.38 – 7.31 (m, 3H), 7.24 – 7.17 (m, 2H), 5.63 (s, 2H), 4.41 (q, J = 7.1 Hz, 2H), 3.88 (s, 3H), 1.39 (t, J = 7.1 Hz, 3H).

^{13}C NMR (101 MHz, CHLOROFORM-*D*) δ 162.70, 159.09, 137.19, 135.24, 133.39, 130.01, 129.26, 128.75, 127.97, 62.17, 52.51, 52.07, 14.36.

HRMS (ESI) m/z: $[M + H]^+$ calcd for $C_{15}H_{17}N_2O_4^+$ 289.1183; found 289.1184

Synthesis of (1-benzyl-1H-imidazole-2,4-diyl)dimethanol **(3)**

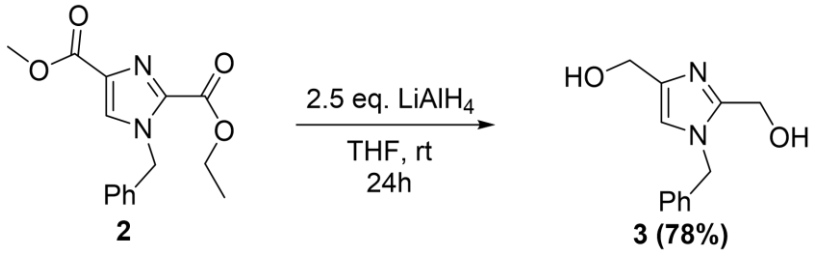

2 **3 (78%)**

Compound **2** (0.95 g, 3.3 mmol, 1 eq.) was dissolved in dry THF (65 mL) and loaded into a flame dried round bottom flask under Ar. Then $LiAlH_4$ (313 mg, 8.2 mmol, 2.5 eq.) was added slowly at 0 degrees. Following the addition the reaction was allowed to stir at room temperature overnight. The reaction was quenched with water, and the reaction mixture was filtered. The solvent was evaporated via rotary evaporation. Then 30 mL of water was added, and the product was extracted with 4x50 mL chloroform:isopropanol (3:1). The organic layers were collected and dried with Na_2SO_4, filtered and the solvent was evaporated using rotary evaporation. The product was purified by silica gel column chromatography (MeOH/DCM 1:9). Affording **3** as a brown oil. (562 mg, 2.57 mmol, 78%).

^{1}H NMR (400 MHz, CHLOROFORM-*D*) δ 7.37 – 7.30 (m, 3H), 7.14 (d, *J* = 7.1 Hz, 2H), 6.81 (s, 1H), 5.14 (s, 2H), 4.62 (s, 2H), 4.53 (s, 2H).

^{13}C NMR (101 MHz, CHLOROFORM-*D*) δ 148.01, 140.26, 136.08, 129.11, 128.62, 128.32, 127.43, 118.26, 57.64, 55.89, 49.83.

HRMS (ESI) m/z: $[M + H]^+$ calcd for $C_{12}H_{15}N_2O_2^+$ 219.1128; found 219.1136

Synthesis of 1-benzyl-2,4-bis(chloromethyl)-1H-imidazol-3-ium **(4)**

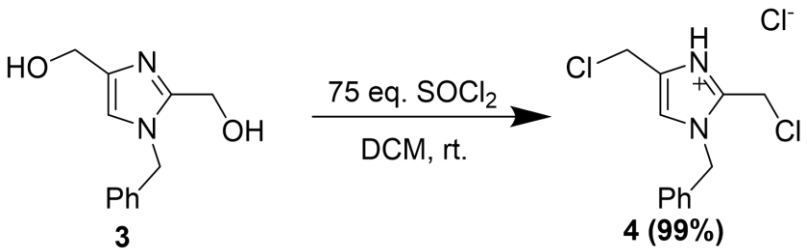

3 **4 (99%)**

Compound **3** (207 mg, 0.95 mmol, 1 Eq) was dissolved in 15 mL of dry DCM and loaded into a flame dried round bottom flask under Ar. Then $SOCl_2$ (8.48 g, 71.3 mmol, 75 eq.) was slowly added at 0 degrees. The reaction was left stirring overnight at room temperature. The reaction mixture was poured over ice and extracted with 3x40 mL

chloroform:isopropanol (3:1), affording **4** (276 mg, 0.95 mmol, 99%) as a dark oil. The product was used without further purification.

^{1}H NMR (400 MHz, DMSO-D_6) δ 7.38 – 7.26 (m, 6H), 5.28 (s, 2H), 4.93 (s, 2H), 4.65 (s, 2H).

HRMS (ESI) m/z: $[M + H]^+$ calcd for $C_{12}H_{13}Cl_2N_2^+$ 255.0450; found 255.0450

Cyclization General Procedure A

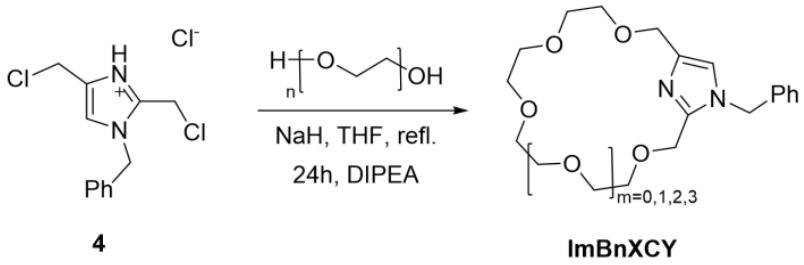

4 **ImBnXCY**

A tricol round bottom flask was flame dried and placed under Ar, dry THF (0.005M) and NaH (4 eq) was added. The mixture was heated to reflux. **4** (1 eq) was dissolved in dry THF (0.025-0.05 mM) along with DIPEA (1 Eq). Another solution of the corresponding polythethylene glycol (1 Eq) was dissolved in dry THF (0.025-0.05M). The same concentration was made for both solutions, while diluting as much as the set up permitted. Both solutions were added slowly and simultaneously over 3h using a syringe pump. The reaction was left to stir at reflux overnight. The reaction was then quenched with 20 mL of water and filtered. The solvent was evaporated using rotary evaporation. Then, 150 mL of chloroform was added, and the product was extracted using 3x100 mL 1M HCl. The aqueous phases were gathered and basified to pH 13 using 6M NaOH. Then the product was extracted using 3x150 mL CHCl3. The organic phases were gathered and evaporated using rotary evaporation to yield the crude product.

*Synthesis of **ImBn15C5** (m = 0)*

(Z)-benzyl-11H-3,6,9,12-tetraoxa-1(2,4)-imidazolacyclotridecaphane **ImBn15C5** (n=0)(330 mg, 1.13 mmol, 1 eq.) was prepared according to the general procedure A by creating a solution of **4** and DIPEA (146 mg, 1.13 mmol, 1 eq.) in 20 mL of THF (0.056 mM). The second solution used was a triethylene glycol (170 mg, 1.13 mmol, 1 eq.) in 20 mL of THF (0.056 mM). The product was purified using consecutive column chromatography (Neutral alumina, MeOH/DCM 3:97, then neutral alumina MeOH/DCM 1:99) affording product **5** (22 mg, 0.066 mmol, 6%) as a clear oil.

^{1}H NMR (400 MHz, ACETONITRILE-D3) δ 7.37 – 7.19 (m, 5H), 6.96 (s, 1H), 5.13 (s, 2H), 4.49 (s, 2H), 4.25 (s, 2H), 3.62 (t, J = 5.9 Hz, 2H), 3.52 (dd, J = 5.8, 3.3 Hz, 2H), 3.41 – 3.29 (m, 4H), 3.26 (dd, J = 5.8, 3.3 Hz, 2H), 3.19 (t, J = 5.9 Hz, 2H).

^{13}C NMR (101 MHz, ACETONITRILE-D_3) δ 146.67, 138.59, 138.29, 129.69, 128.80, 128.60, 121.50, 118.33, 70.83, 70.43, 70.05, 70.01, 67.82, 65.90, 65.14, 50.09.

HRMS (ESI$^+$) m/z: $[M + H]^+$ calcd for $C_{18}H_{25}N_2O_4$, 333.1809; found, 333.1810

*Synthesis of **ImBn18C6** (m = 1)*

(Z)-benzyl-11H-3,6,9,12,15-pentaoxa-1(2,4)-imidazolacyclohexadecaphane **Imn18C6** (n=1)(200 mg, 0.69 mmol, 1 eq.) was prepared according to general procedure A by creating a solution of **4** and DIPEA (89 mg, 0.69 mmol, 1 eq.) in 20 mL of THF (0.034 mM). The second solution used was a tetraethylene glycol (133 mg, 0.69 mmol, 1 eq.) in 20 mL of THF (0.034 mM). The product was purified using dry neutral alumina column chromatography (MeOH/DCM 2:98), affording product **6** (92 mg, 0.24 mmol, 36%) as an orange oil.

^{1}H NMR (600 MHz, ACETONITRILE-D_3) δ 7.36 – 7.18 (m, 4H), 6.94 (s, 1H), 5.13 (s, 2H), 4.46 (s, 2H), 4.26 (s, 2H), 3.57 – 3.41 (m, 16H).

^{13}C NMR (101 MHz, ACETONITRILE-D_3) δ 145.81, 138.72, 138.30, 129.74, 128.79, 128.43, 121.02, 118.37, 71.07, 71.05, 70.98, 70.92, 70.32, 69.99, 69.27, 66.32, 64.52, 50.14.

HRMS (ESI^+) m/z: $[M + H]^+$ calcd for $C_{20}H_{29}N_2O_5$, 377.2071; found, 377.2074.

*Synthesis of **ImBn21C7** (m = 2)*

(Z)-benzyl-11H-3,6,9,12,15,18-hexaoxa-1(2,4)-imidazolacyclononadecaphane **ImBn21C7** (n=2) (153 mg, 0.52 mmol, 1 eq.) was prepared according to general procedure A by creating a solution of **4** and DIPEA (67.8 mg, 0.52 mmol, 1 eq.) in 20 mL of THF (0.026 mM). The second solution used was a pentaethylene glycol (133 mg, 0.69 mmol, 1 eq.) in 20 mL of THF (0.026 mM). The product was purified using consecutive column chromatography (Neutral alumina, MeOH/DCM 3:97, then neutral alumina MeOH/DCM 1:99) affording product **7** (48 mg, 0.11 mmol, 22%) as a yellow oil.

^{1}H NMR (400 MHz, ACETONITRILE-D_3) δ 7.53 – 7.15 (m, 4H), 6.96 (s, 1H), 5.15 (s, 2H), 4.44 (d, J = 1.0 Hz, 2H), 4.26 (s, 2H), 3.67 – 3.33 (m, 20H).

^{13}C NMR (101 MHz, ACETONITRILE-D_3) δ 145.56, 138.59, 138.28, 129.76, 128.81, 128.48, 121.24, 118.35, 71.40, 71.33, 71.26, 71.22, 71.18, 71.16, 71.14, 70.73, 69.83, 69.66, 66.65, 64.97, 50.26.

HRMS ($APCI^+$) m/z: $[M + H]^+$ calcd for $C_{22}H_{33}N_2O_6$, 421.2333; found, 421.2341

*Synthesis of **ImBn24C8** (m = 3)*

(Z)-benzyl-11H-3,6,9,12,15,18,21-heptaoxa-1(2,4)-imidazolacyclodocosaphane **ImBn24C8** (n=3)(300 mg, 1.03 mmol, 1 eq.) was prepared according to general procedure A by creating a solution of **4** and DIPEA (0.132 mg, 1.03 mmol, 1 eq.) in 20 mL of THF (0.05 mM). The second solution used was a hexaethylene glycol (290 mg, 1.03

mmol, 1 eq.) in 20 mL of THF (0.05 mM). The product was purified using consecutive column chromatography (Neutral alumina, MeOH/DCM 3:97, then neutral alumina MeOH/DCM 2:98) affording product **8** (72 mg, 0.155 mmol, 15%) as a clear oil.

^{1}H NMR (400 MHz, ACETONITRILE-D_3) δ 7.36 – 7.25 (m, 3H), 7.19 (d, J = 7.4 Hz, 2H), 6.97 (s, 1H), 5.18 (s, 2H), 4.46 (s, 2H), 4.30 (s, 2H), 3.53 – 3.47 (m, 24H).

^{13}C NMR (101 MHz, ACETONITRILE-D_3) δ 129.74, 128.71, 128.43, 121.18, 118.34, 71.43, 71.39, 71.33, 71.27, 71.03, 70.18, 69.88, 67.14, 65.51, 50.23.

HRMS (ESI$^+$) m/z: $[M + H]^+$ calcd for $C_{24}H_{37}N_2O_7$, 465.25953; found, 465.26014

Titrations

To perform titrations two stocks solutions were prepared. One of the solutions was created by precisely measuring out a mass of the host and dissolving it in CD_3CN at concentrations ranging from 0.072 mM to 1.71 mM, depending on the size of the crown ether. Subsequently, a guest solution was made by measuring the solid amount of guest separately and dissolving the solid using liquid from the host stock solution in a separate container, to mitigate dilution errors. The guest stock solution was made to be approximately ten times more concentrated that the host with the concentration ranging between 0.524 mM to 21.4 mM. The small masses at the milligram level of the host and guest were measured using a precision scale. However, to ensure the nominal concentration matched the experimental concentration, quantitative NMR measurements were performed using 1,3,5-trimethoxybenzene as an internal standard. The host concentrations were subsequently corrected based on these measurements.

For each titration, care was taken to ensure that $[H_0]*K_A$ was mostly less than 100 (see table S1) to maximize the information content of the titration curve, as recommended by Thordarson for systems with high K_A values.[1] Addition of the guest stock solution was done using Hamilton® syringes or calibrated micropipettes. The minimum added volume was 2.5 µL. After each addition, the solution was homogenized using a vortex mixer or mixing with the micropipette.

The binding isotherms were fit to a 1:1 binding model using the different resonances or the wavelength exhibiting the maximum of absorbance, with the BindFit program available at https://supramolecular.org.[1,2] The chosen resonances for ^1H NMR titrations were those exhibiting a large and consistent chemical shift change, while also remaining well isolated. For improved accuracy, each titration was repeated at least three times; the reported errors correspond to the standard deviation of the K_A values obtained from each independent trials between systems.

NMR titrations SI

ImBn15C5 *with* $NaPF_6$

Trial 1

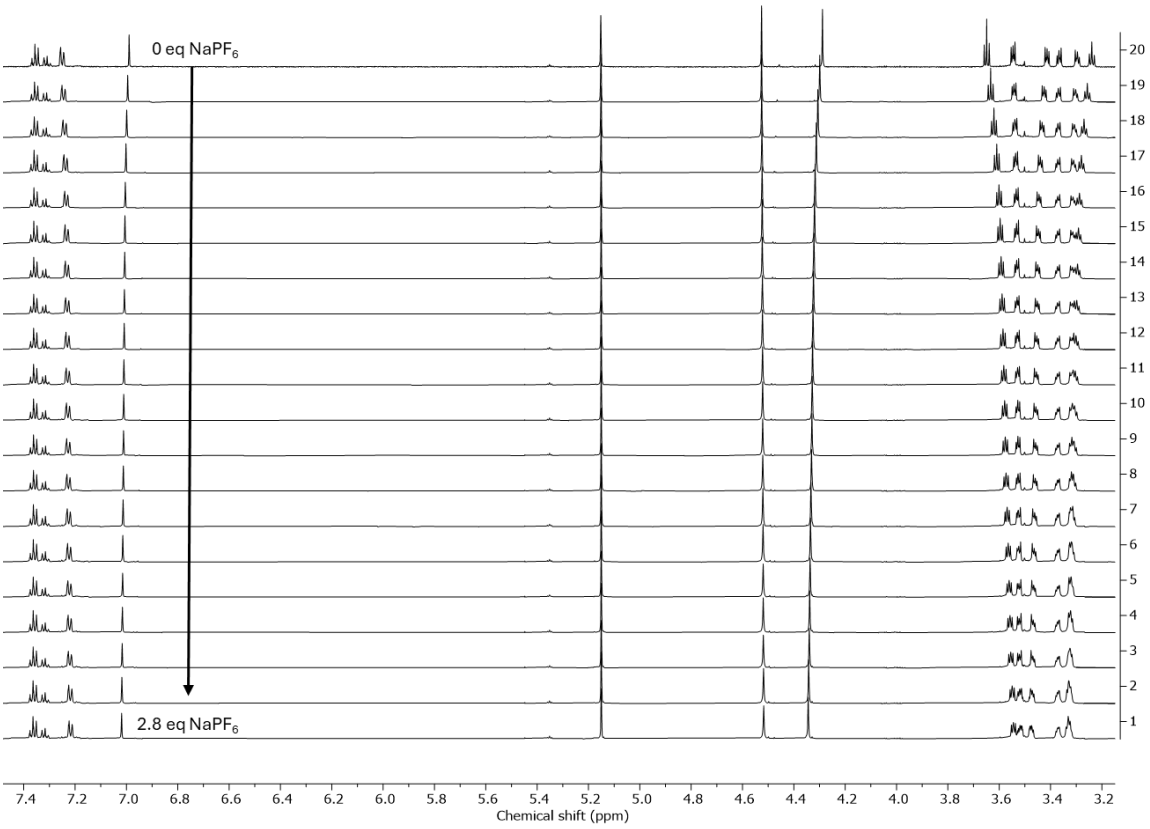

Figure S1. Stacked ^{1}H NMR spectrum with the increasing addition of the guest $NaPF_6$ from 0 to 2.8 equivalents, host concentration [**ImBn15C5**] = 0.551 mM in CD_3CN at 20°C

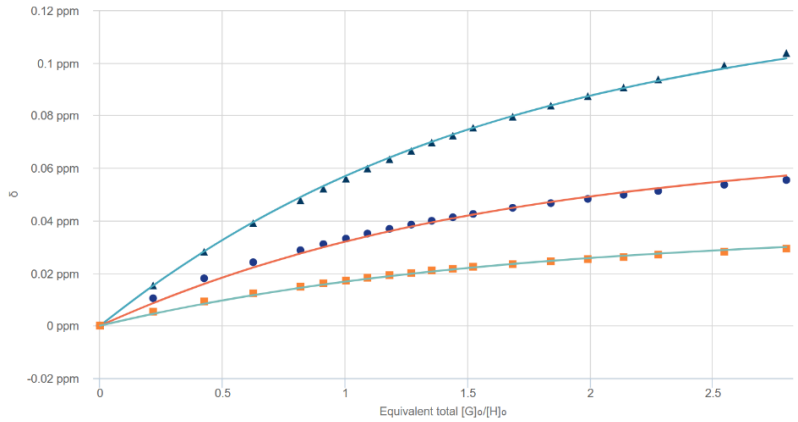

Figure S2. Fitted titration data on bindfit for a K_a of 1762.06 M^{-1} and fitting error of ± 1.2498 %

Trial 2

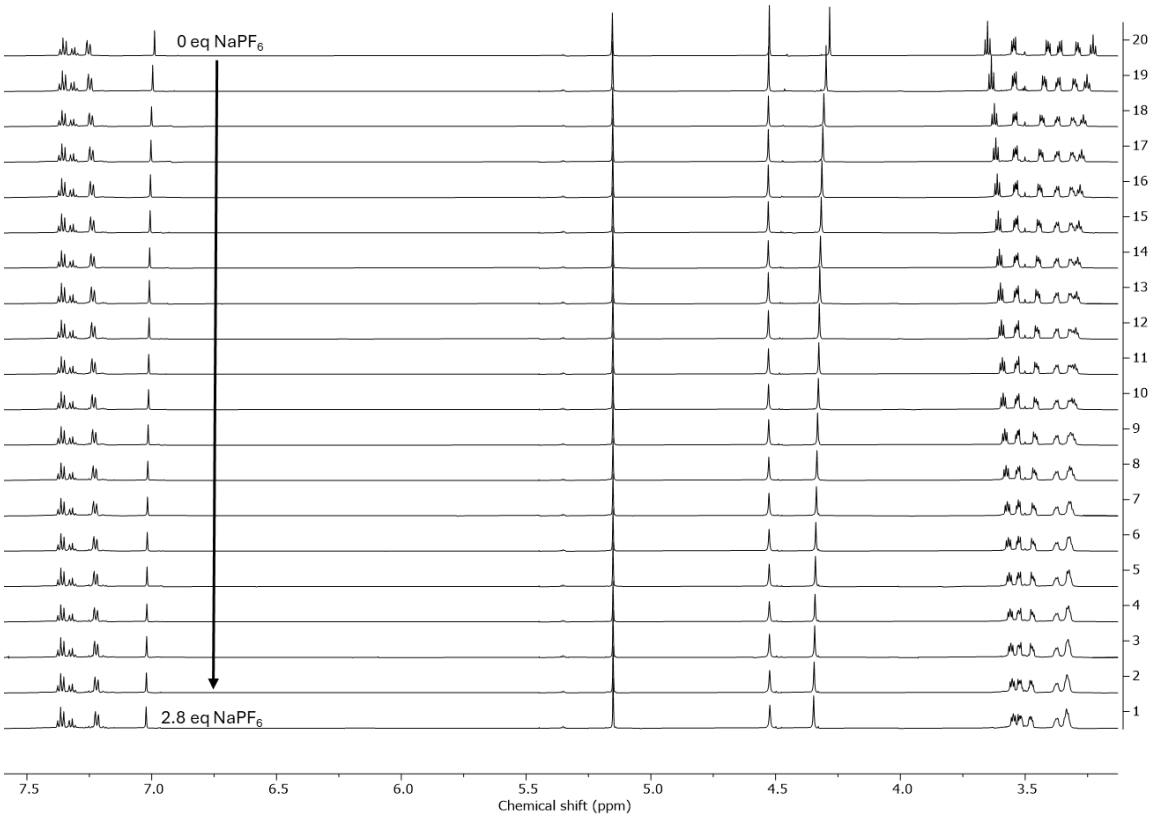

Figure S3. Stacked ^{1}H NMR spectrum with the increasing addition of the guest $NaPF_6$ from 0 to 2.8 equivalents, host concentration [**ImBn15C5**] = 0.551 mM in CD_3CN at 20°C

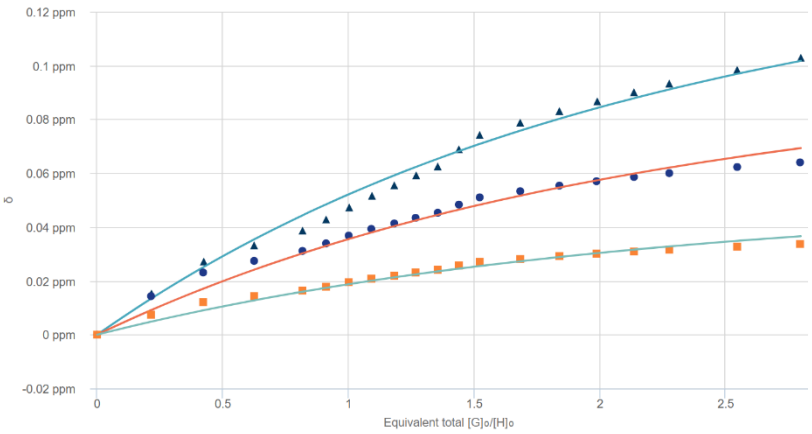

Figure S4. Fitted titration data on bindfit for a K_a of 1003.65 M^{-1} and fitting error of ± 2.8990%

Trial 3

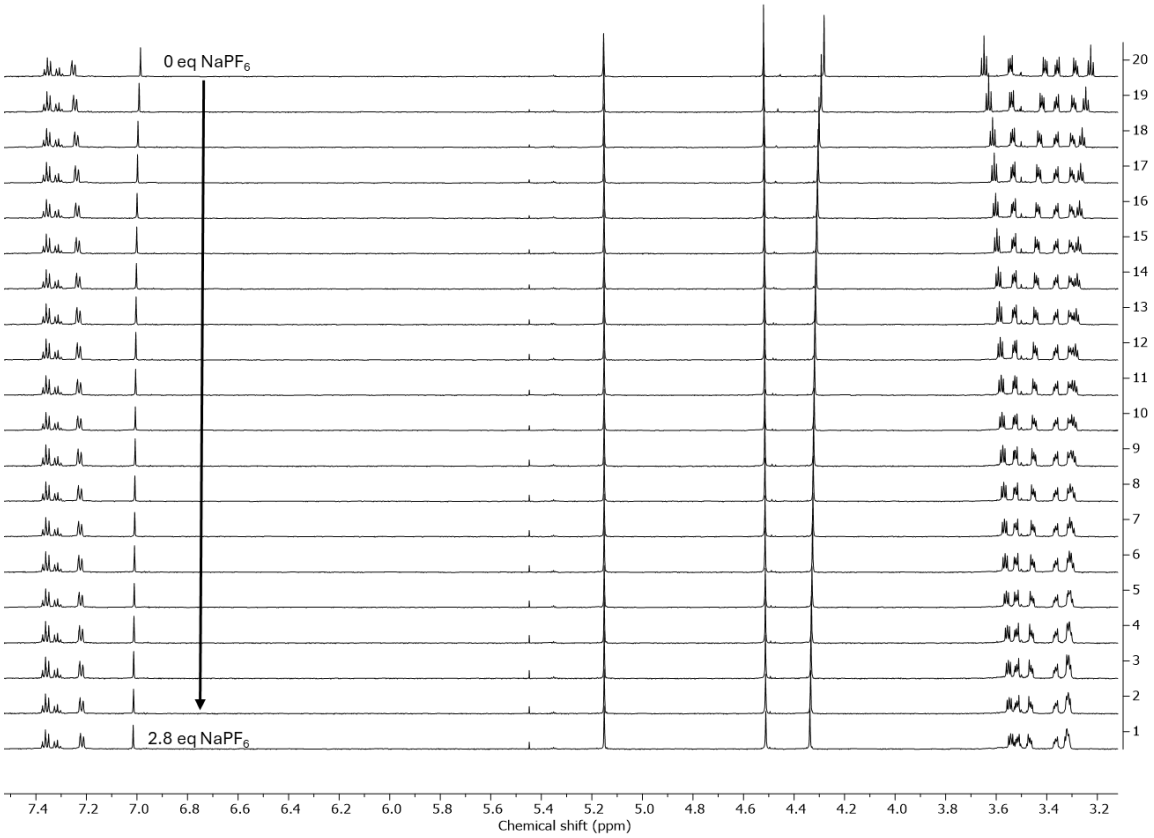

Figure S5. Stacked ^{1}H NMR spectrum with the increasing addition of the guest $NaPF_6$ from 0 to 2.79 equivalents, host concentration [**ImBn15C5**] = 0.483 mM in CD_3CN at 20°C

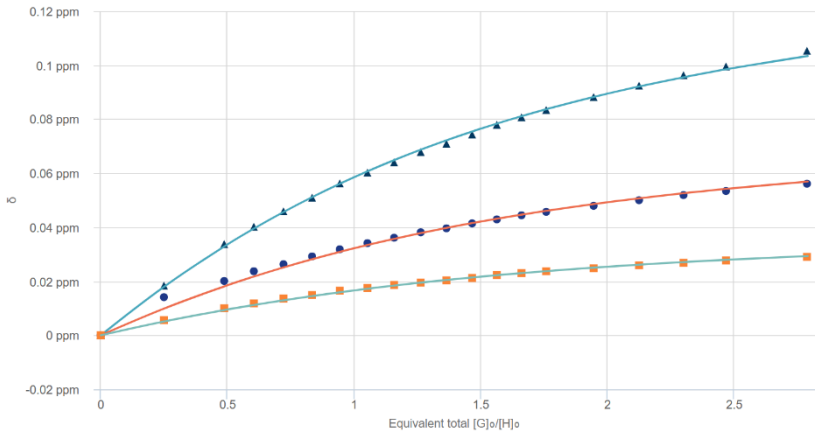

Figure S6. Fitted titration data on bindfit for a K_a of 2148.62 M^{-1} and fitting error of ± 1.3295%

ImBn15C5 with KPF_6

Trial 1

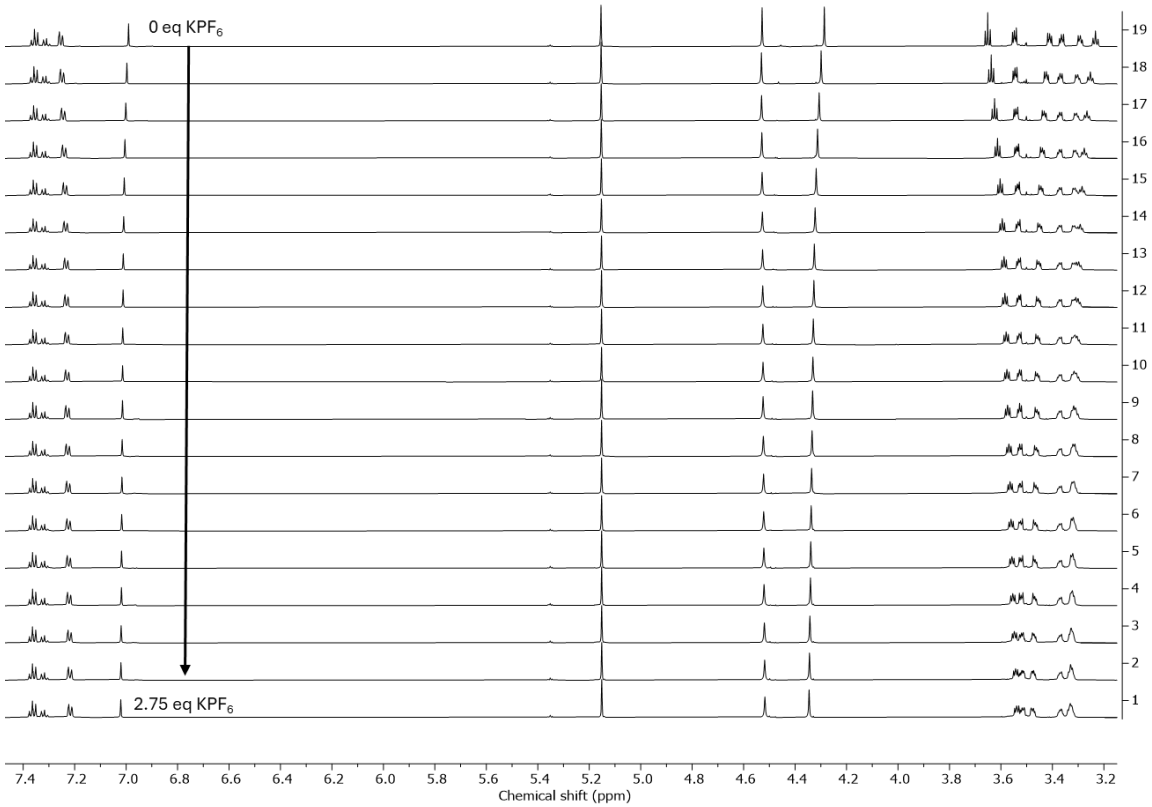

Figure S7. Stacked ^{1}H NMR spectrum with the increasing addition of the guest KPF_6 from 0 to 2.75 equivalents, host concentration [**ImBn15C5**] = 0.545 mM in CD_3CN at 20°C

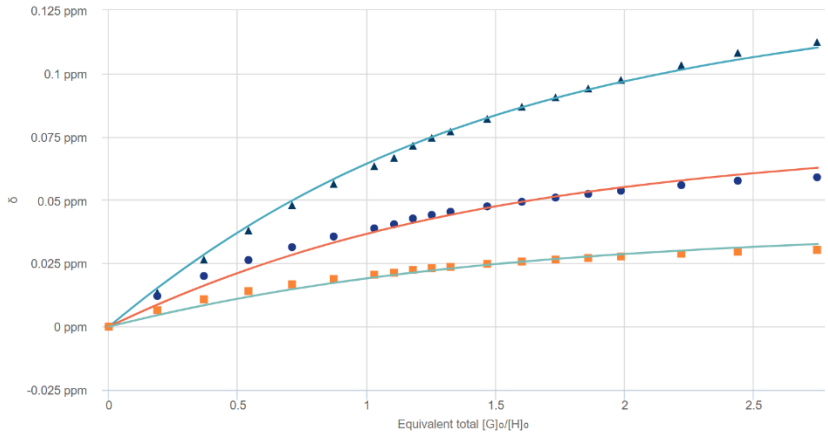

Figure S8. Fitted titration data on bindfit for a K_a of 2253.41 M^{-1} and fitting error of ± 2.6860 %

Trial 2

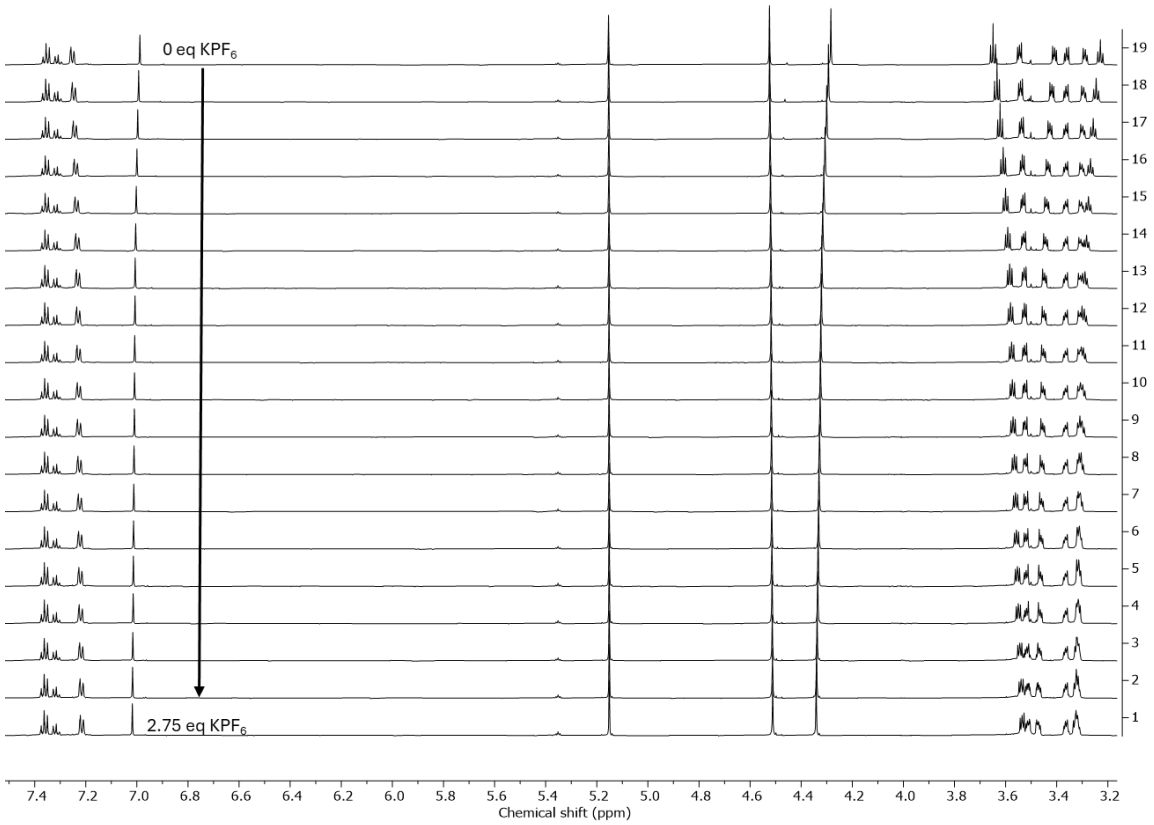

Figure S9. Stacked ^{1}H NMR spectrum with the increasing addition of the guest KPF_6 from 0 to 2.75 equivalents, host concentration [**ImBn15C5**] = 0.545 mM in CD_3CN at 20°C

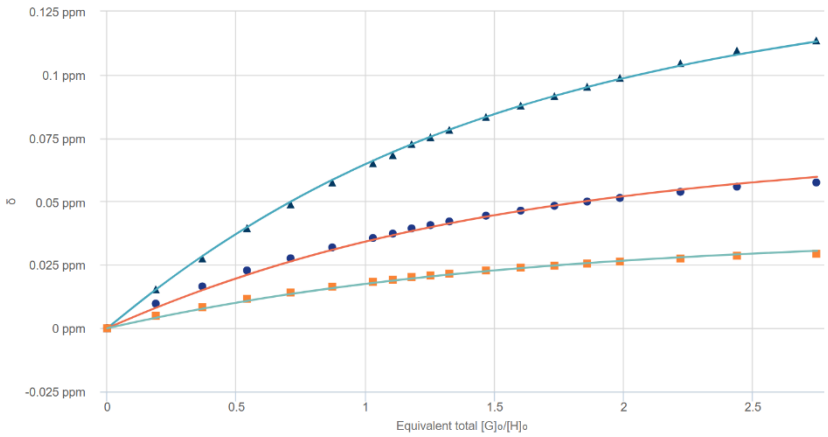

Figure S10. Fitted titration data on bindfit for a K_a of 1971.64 M^{-1} and fitting error of ± 1.1707 %

Trial 3

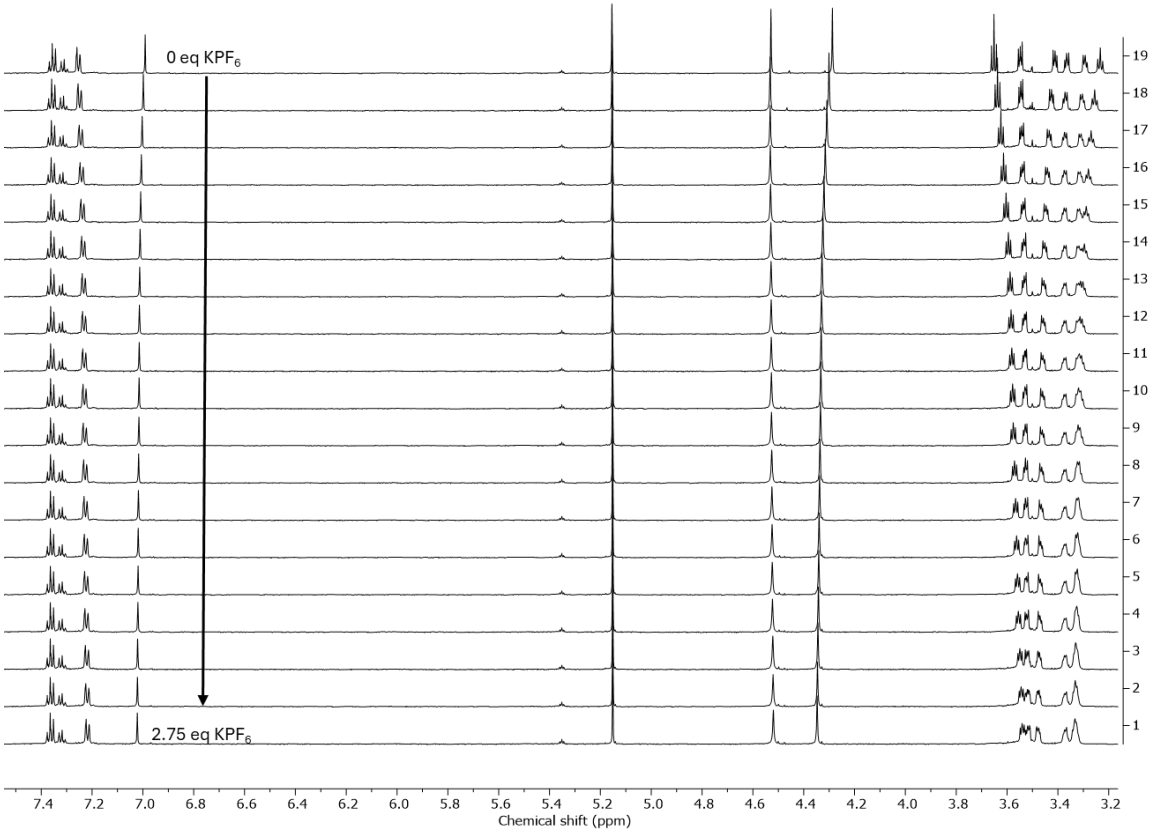

Figure S11. Stacked ^{1}H NMR spectrum with the increasing addition of the guest KPF_6 from 0 to 2.75 equivalents, host concentration [**ImBn15C5**] = 0.545 mM in CD_3CN at 20°C

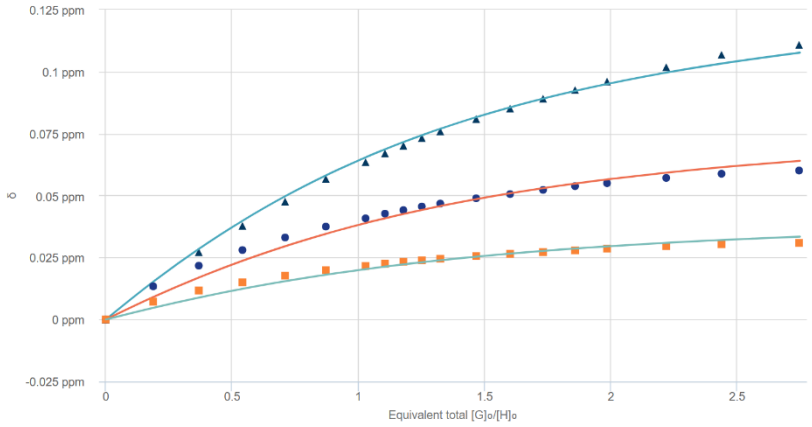

Figure S12. Fitted titration data on bindfit for a K_a of 2571.28 M^{-1} and fitting error of ± 3.2763 %

ImBn18C6 with $NaPF_6$

Trial 1

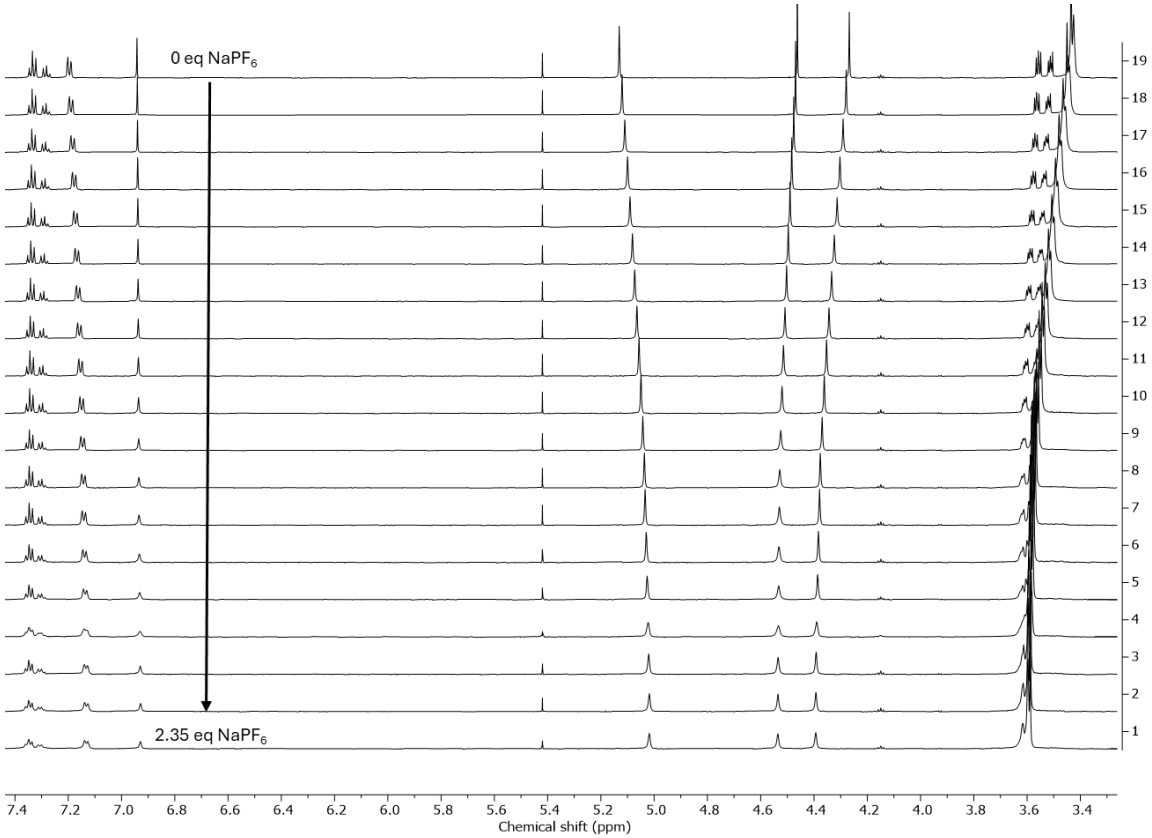

Figure S13. Stacked ^{1}H NMR spectrum with the increasing addition of the guest $NaPF_6$ from 0 to 2.35 equivalents, host concentration [**ImBn18C6**] = 0.448 mM in CD_3CN at 20°C

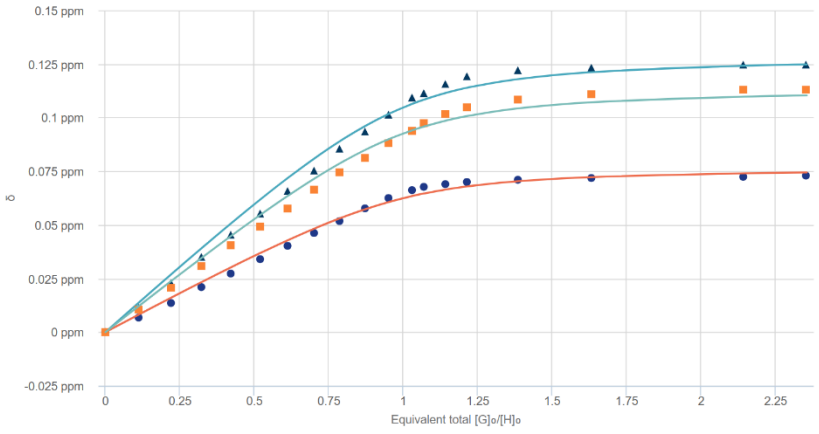

Figure S14. Fitted titration data on bindfit for a K_a of 52730.25 M^{-1} and fitting error of ± 15.1613%

Trial 2

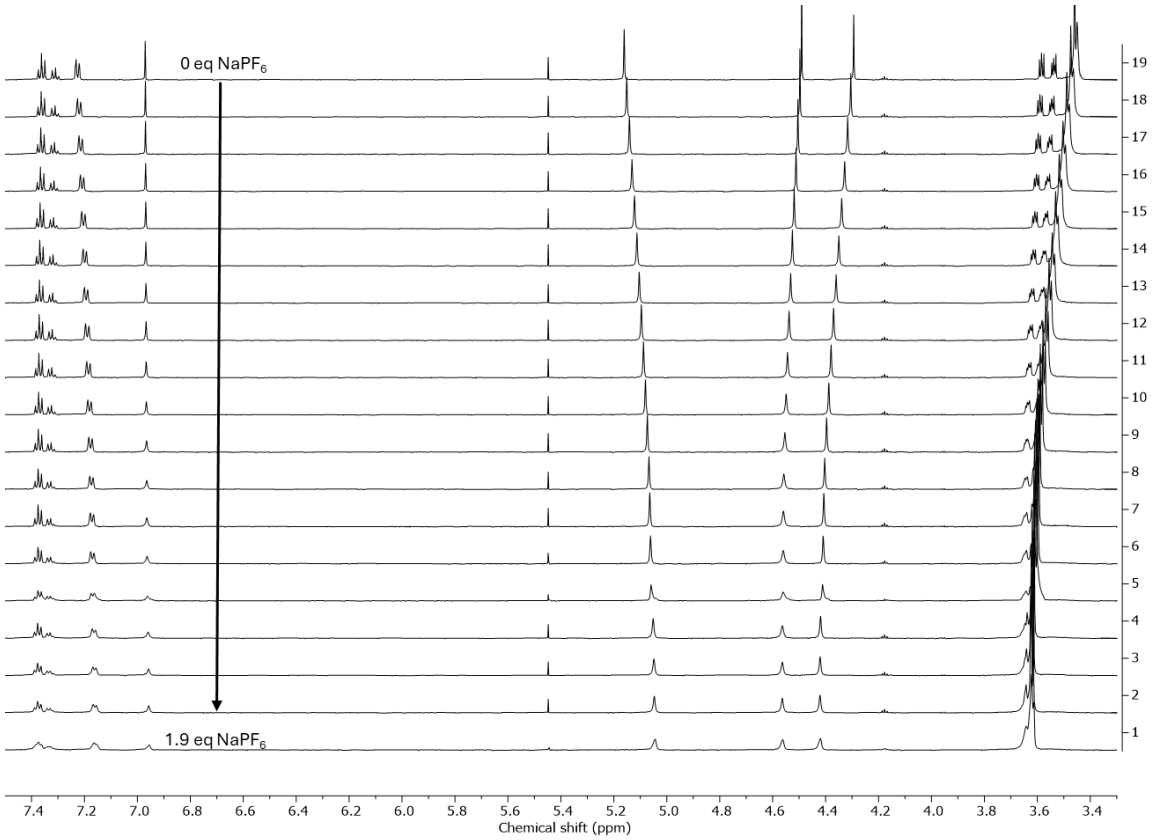

Figure S15. Stacked ^{1}H NMR spectrum with the increasing addition of the guest $NaPF_6$ from 0 to 1.9 equivalents, host concentration [**ImBn18C6**] = 0.448 mM in CD_3CN at 20°C

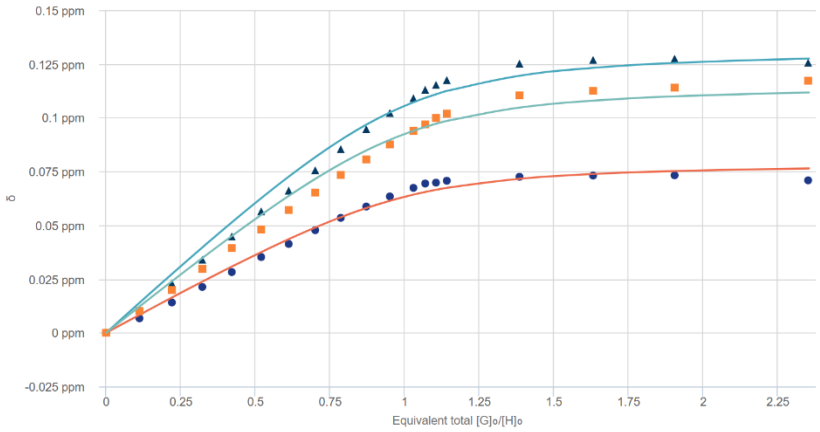

Figure S16. Fitted titration data on bindfit for a K_a of 43804.23 M^{-1} and fitting error of ± 15.8534 %

Trial 3

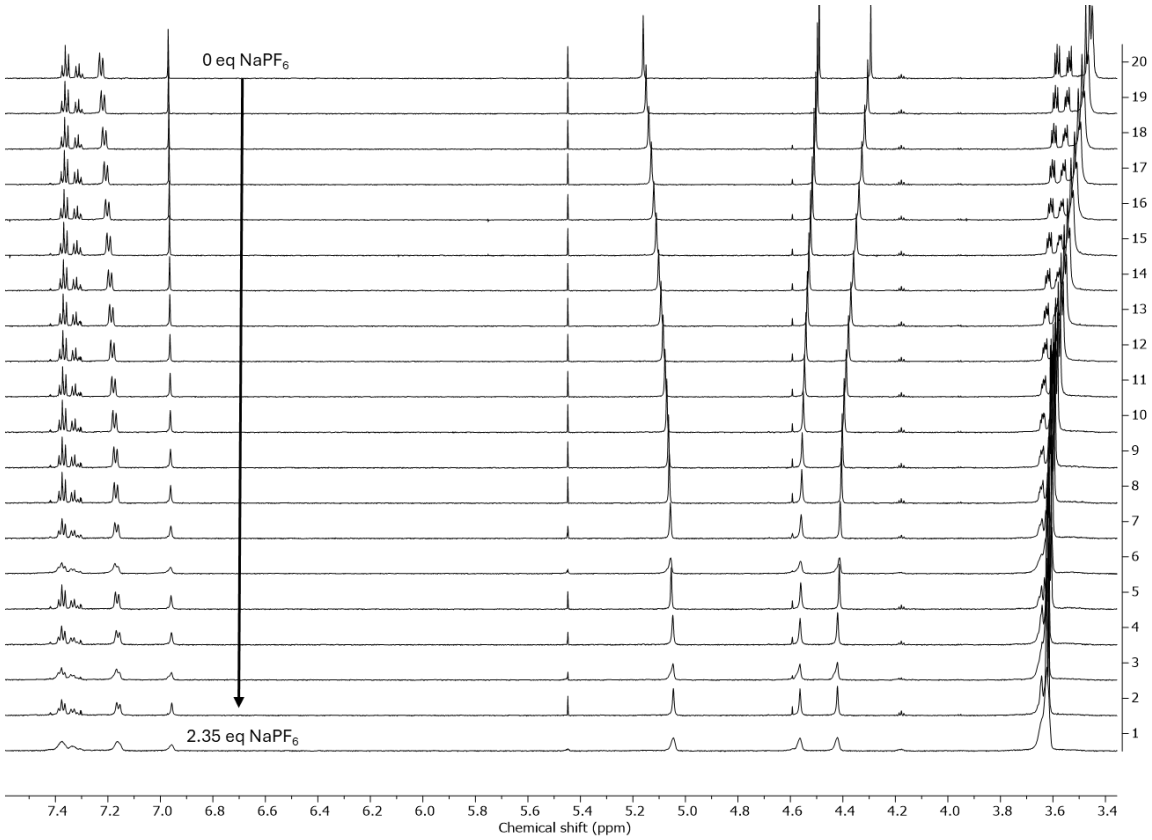

Figure S17 Stacked ^{1}H NMR spectrum with the increasing addition of the guest from 0 to 2.35 equivalents, host concentration [**ImBn18C6**] = 0.448 mM in CD_3CN at 20°C

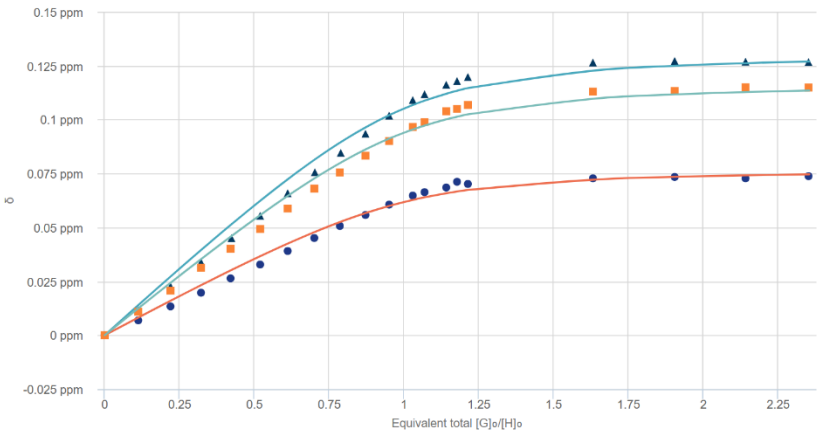

Figure S18. Fitted titration data on bindfit for a K_a of 44056.85 M^{-1} and fitting error of ± 14.0172 %

ImBn18C6 *with* KPF_6

Trial 1

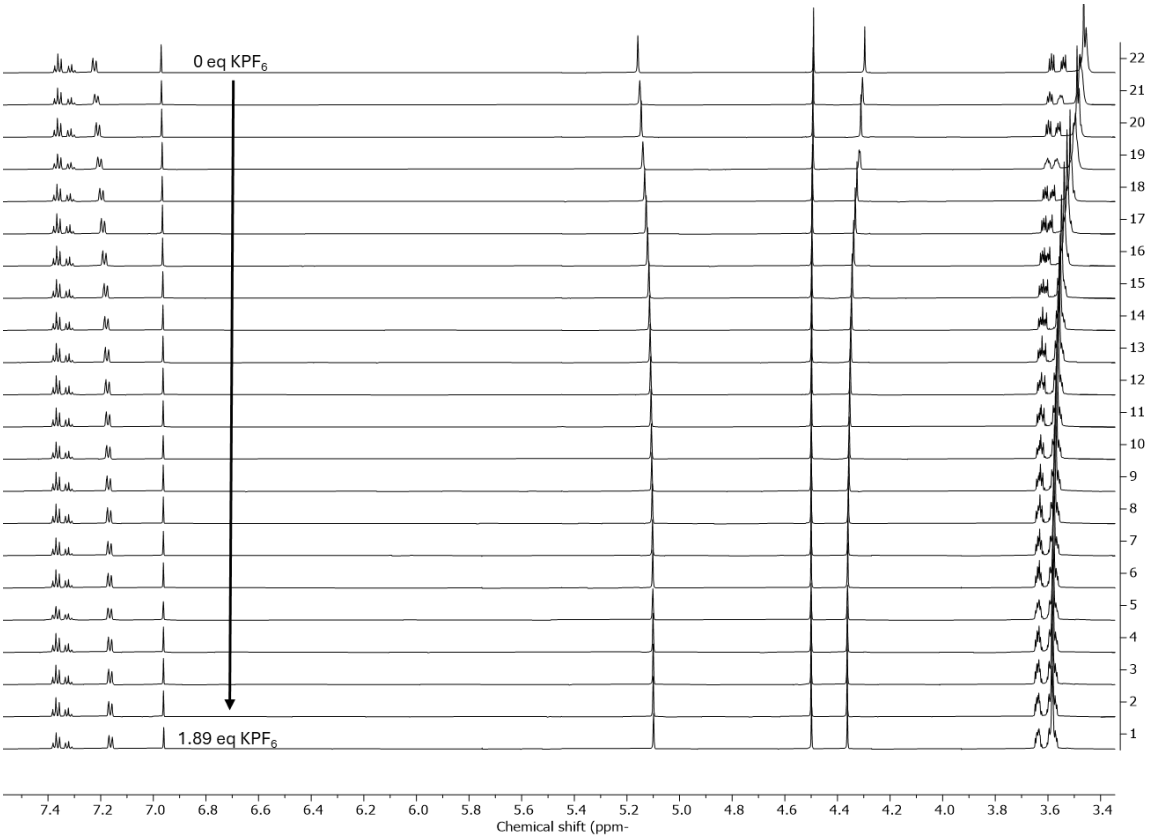

Figure S19. Stacked ^{1}H NMR spectrum with the increasing addition of the guest KPF_6 from 0 to 1.89 equivalents, host concentration [**ImBn18C6**] = 0.43 mM in CD_3CN at 20°C

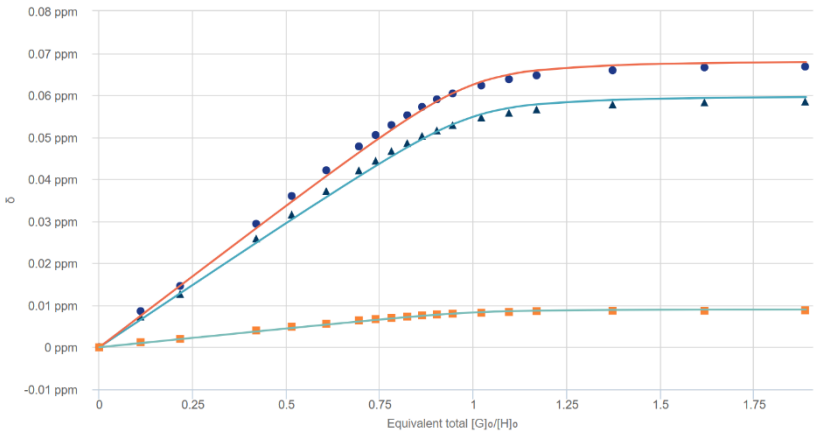

Figure S20. Fitted titration data on bindfit for a K_a of 278890.67 M^{-1} and fitting error of ± 18.3770 %

Trial 2

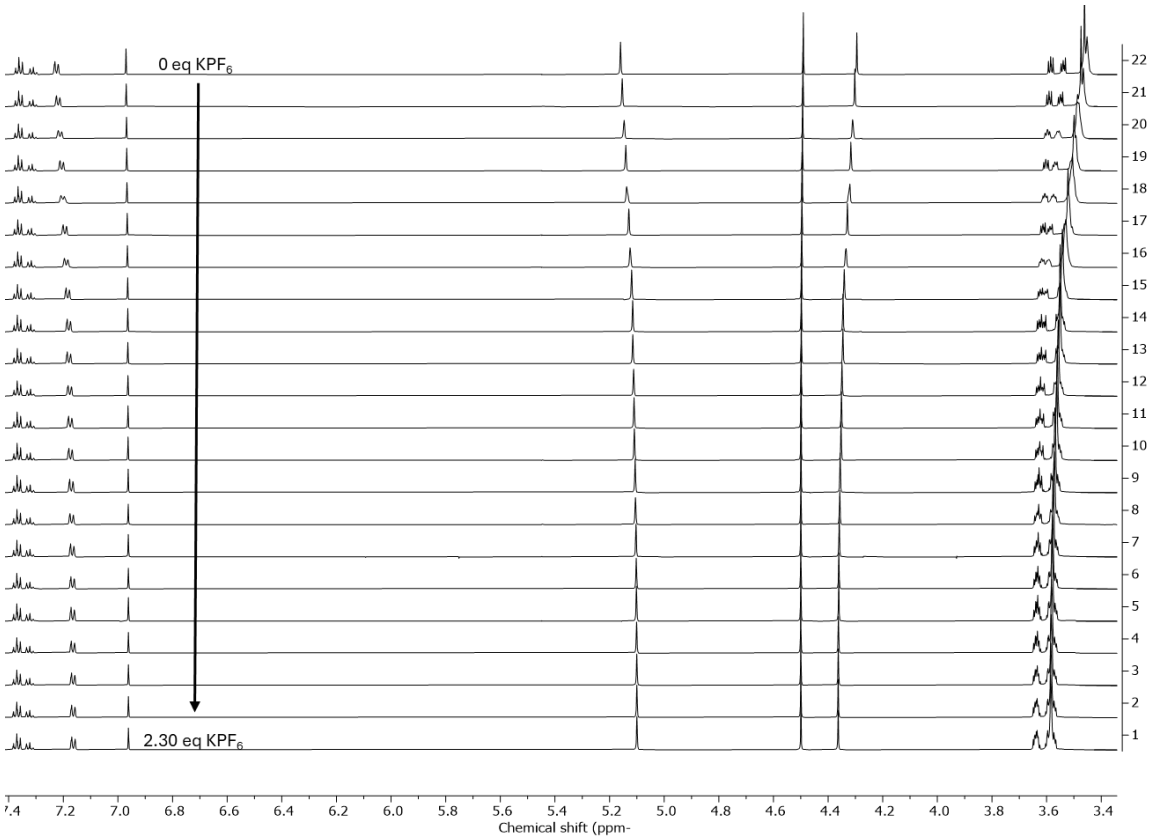

Figure S21. Stacked ^{1}H NMR spectrum with the increasing addition of the guest KPF_6 from 0 to 2.3 equivalents, host concentration [**ImBn18C6**] = 0.44 mM in CD_3CN at 20°C

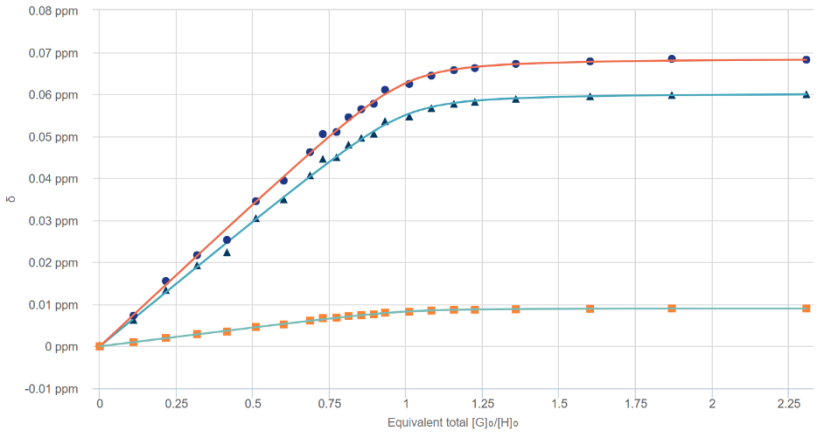

Figure S22. Fitted titration data on bindfit for a K_a of 275891.25 M^{-1} and fitting error of ± 13.7487 %

Trial 3

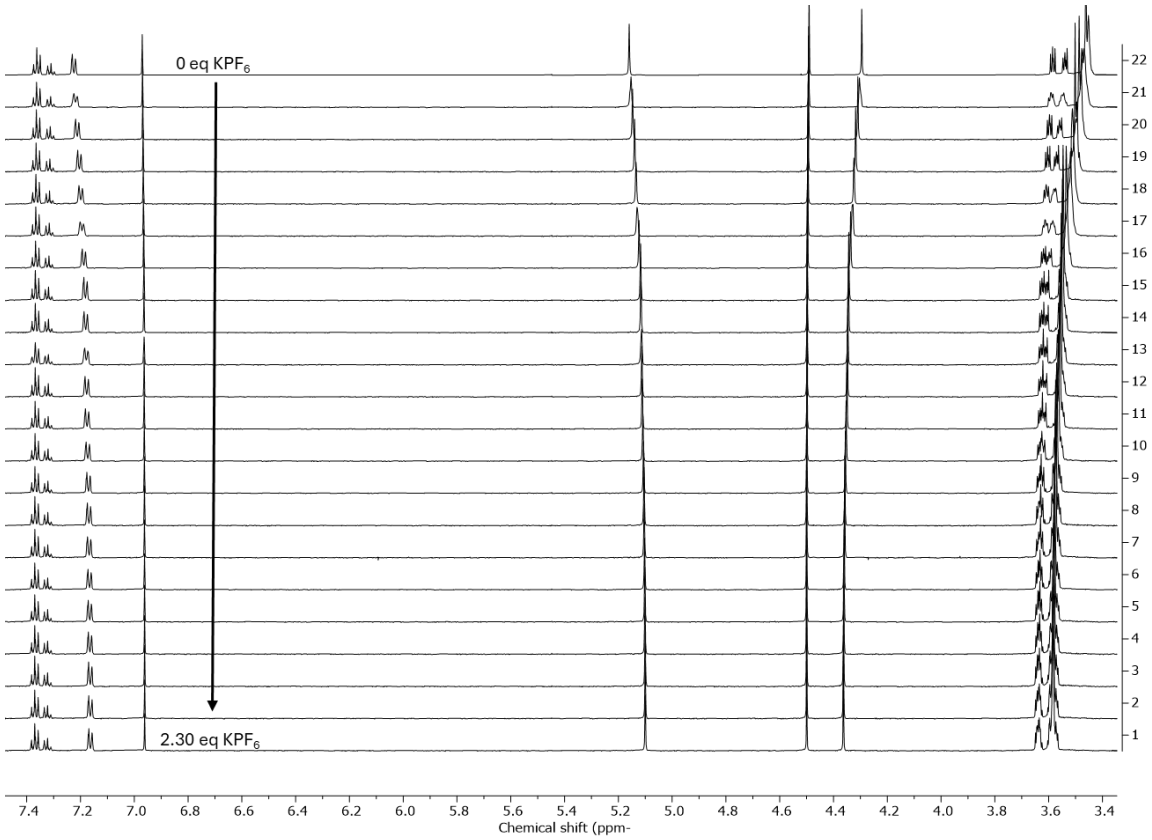

Figure S23. Stacked ^{1}H NMR spectrum with the increasing addition of the guest KPF_6 from 0 to 2.34 equivalents, host concentration [**ImBn18C6**] = 0.44 mM in CD_3CN at 20°C

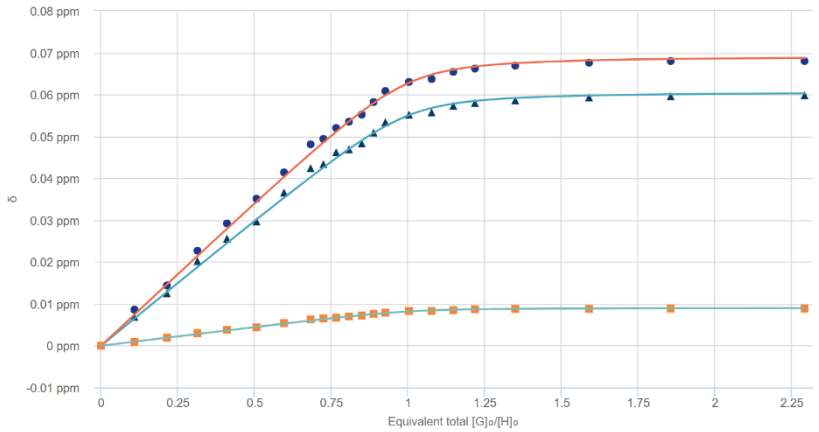

Figure S24. Fitted titration data on bindfit for a K_a of 228136.41 M^{-1} and fitting error of ± 12.9551 %

ImBn21C7 with $NaPF_6$

Trial 1

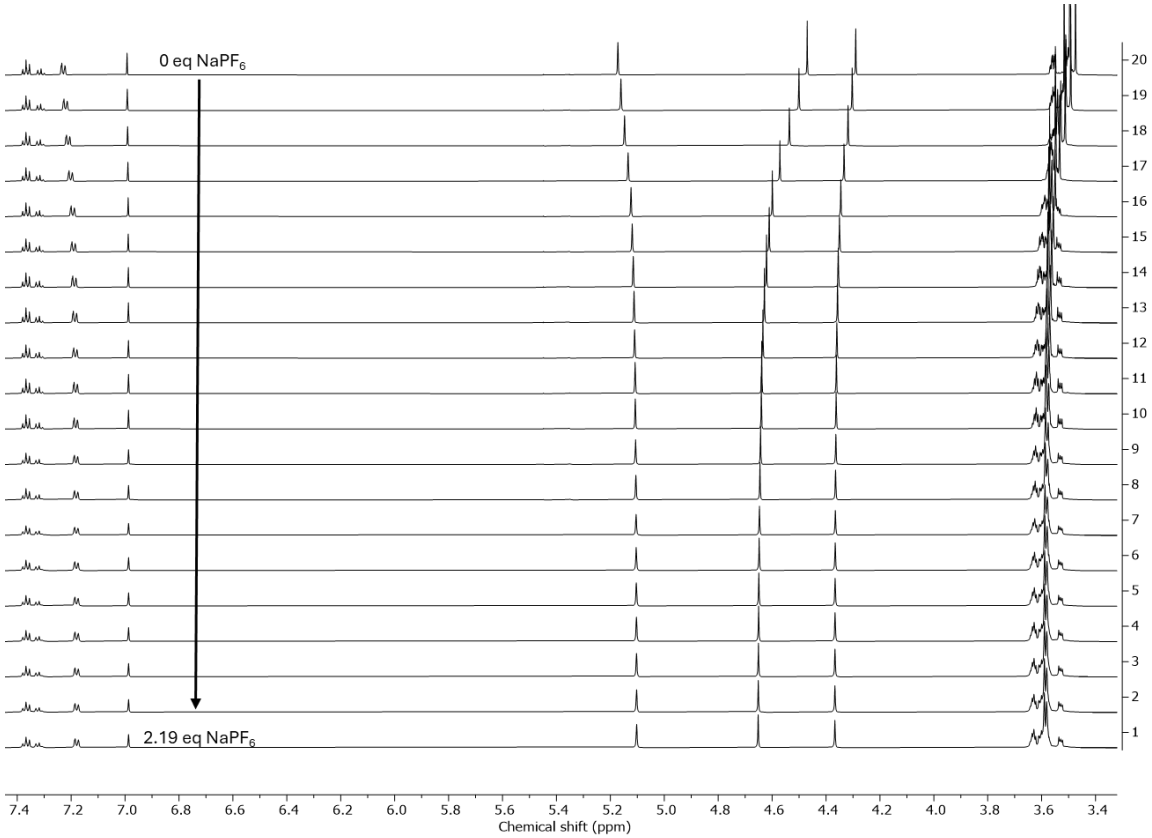

Figure S25. Stacked ^{1}H NMR spectrum with the increasing addition of the guest $NaPF_6$ from 0 to 2.19 equivalents, host concentration [**ImBn21C7**] = 1.71 mM in CD_3CN at 20°C

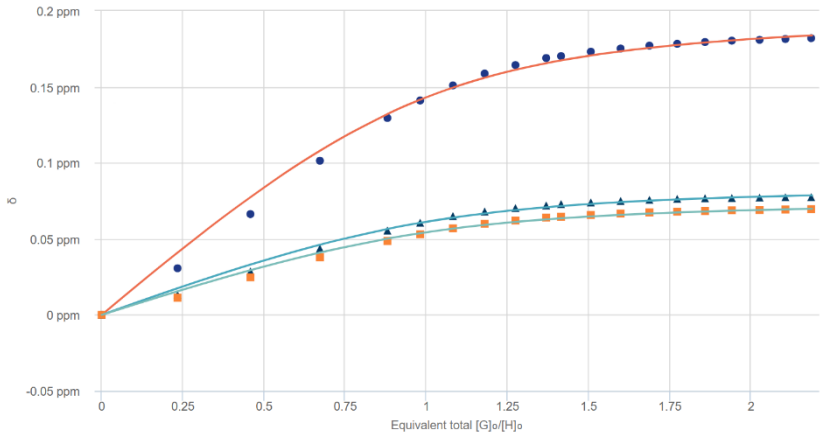

Figure S26. Fitted titration data on bindfit for a K_a of 5102.23 M^{-1} and fitting error of ± 5.9554 %

Trial 2

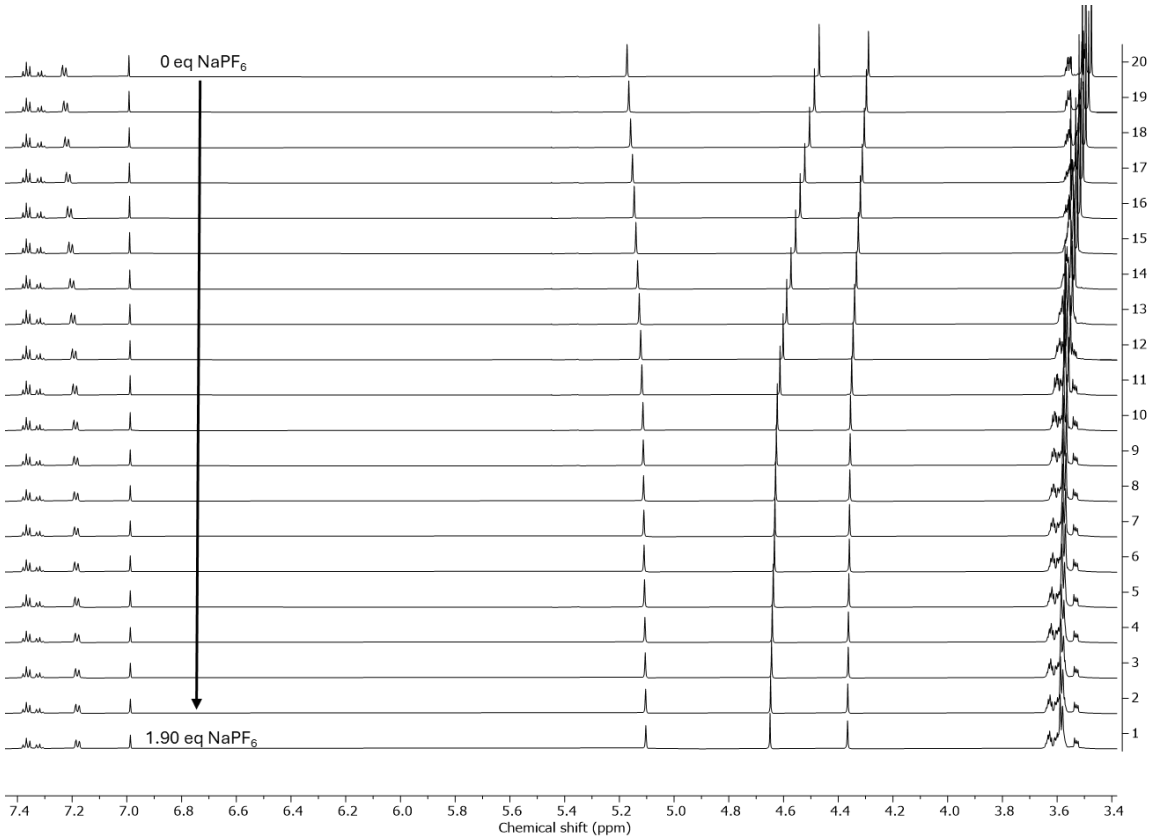

Figure S27. Stacked ^{1}H NMR spectrum with the increasing addition of the guest $NaPF_6$ from 0 to 1.9 equivalents, host concentration [**ImBn21C7**] = 1.71 mM in CD_3CN at 20°C

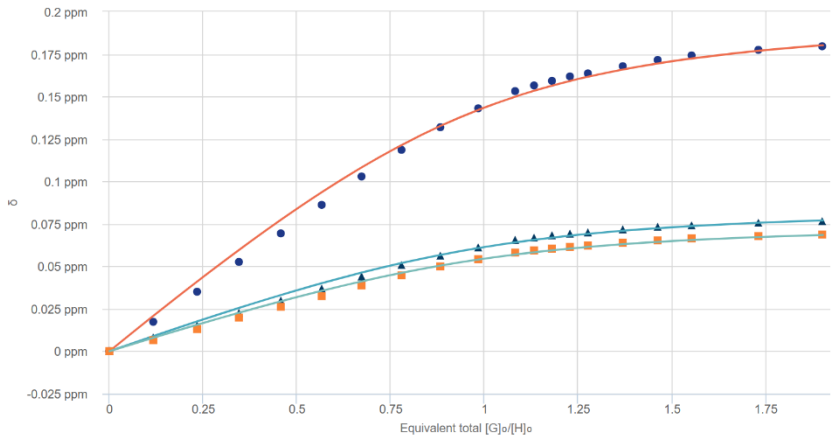

Figure S28. Fitted titration data on bindfit for a K_a of 5182.56 M^{-1} and fitting error of ± 5.7702 %

Trial 3

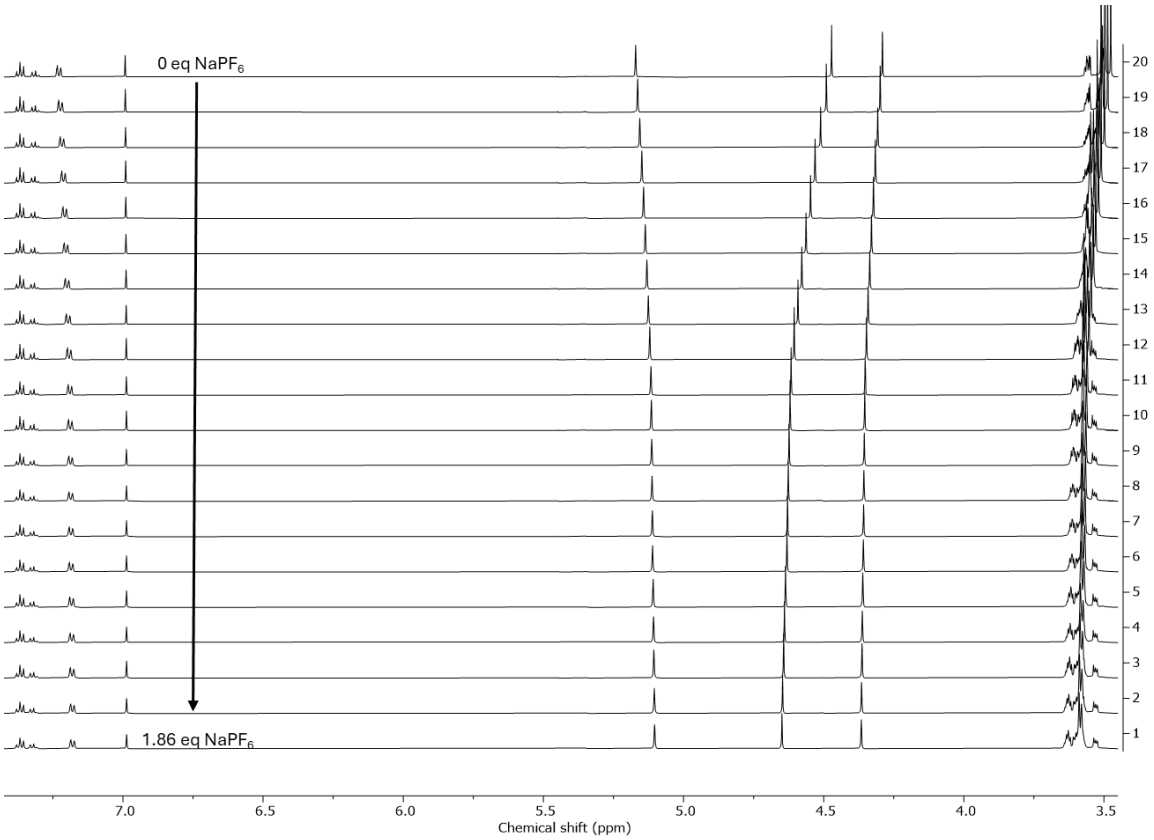

Figure S29. Stacked ^{1}H NMR spectrum with the increasing addition of the guest $NaPF_6$ from 0 to 1.86 equivalents, host concentration [**ImBn21C7**] = 1.71 mM in CD_3CN at 20°C

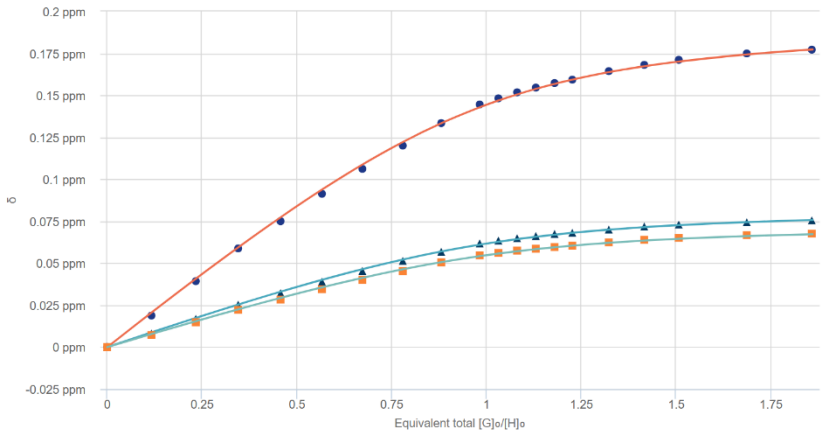

Figure S30. Fitted titration data on bindfit for a K_a of 6741.53 M^{-1} and fitting error of ± 2.3757 %

ImBn21C7 with KPF_6

Trial 1

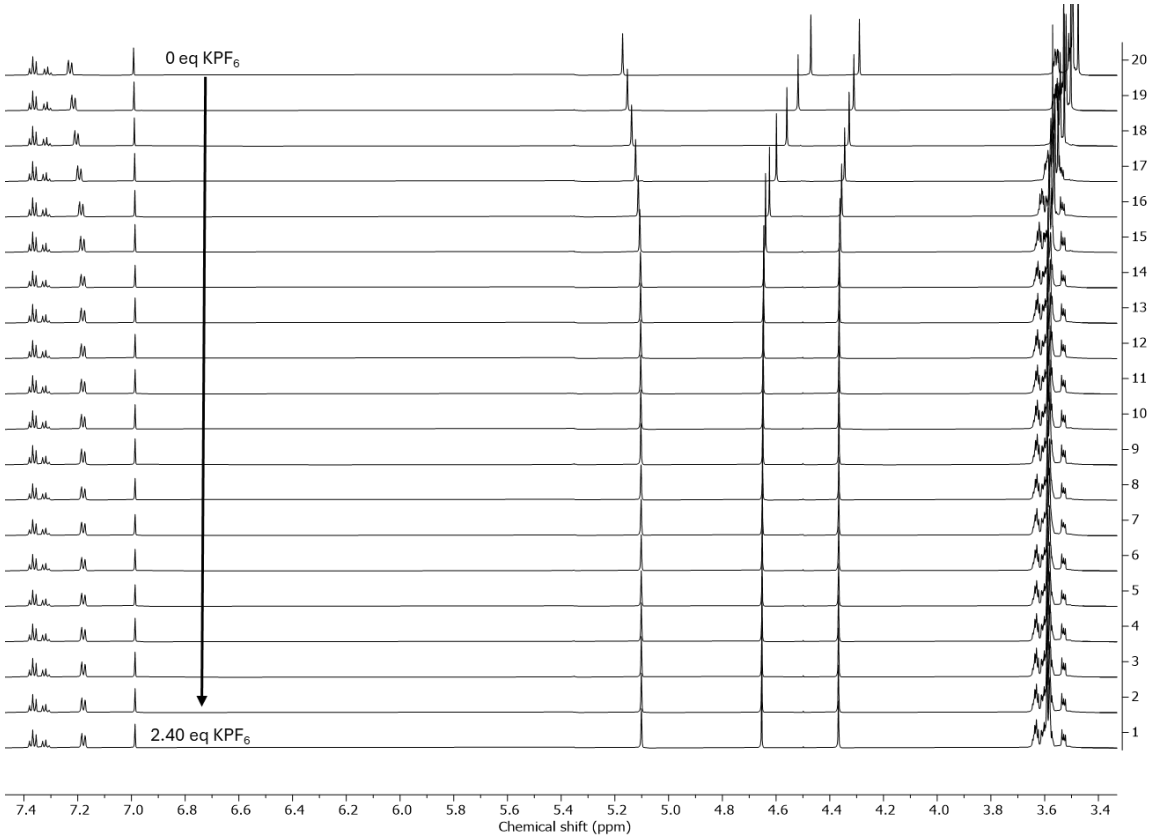

Figure S31. Stacked ^{1}H NMR spectrum with the increasing addition of the guest KPF_6 from 0 to 2.4 equivalents, host concentration [**ImBn21C7**] = 0.551 mM in CD_3CN at 20°C

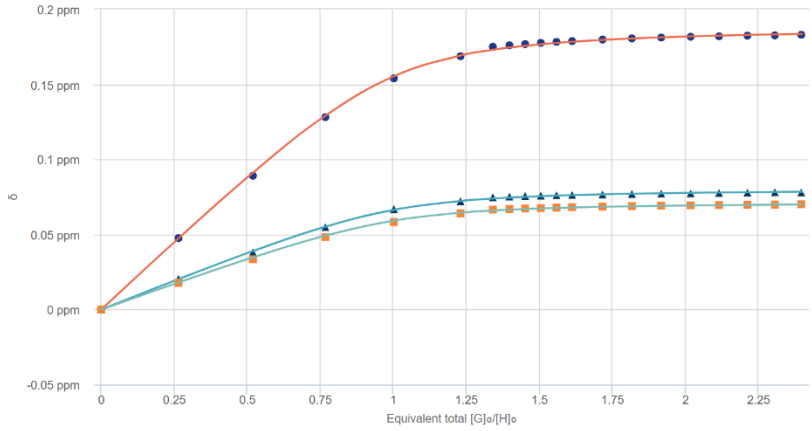

Figure S32. Fitted titration data on bindfit for a K_a of 16844.44 M^{-1} and fitting error of ± 3.2089 %

Trial 2

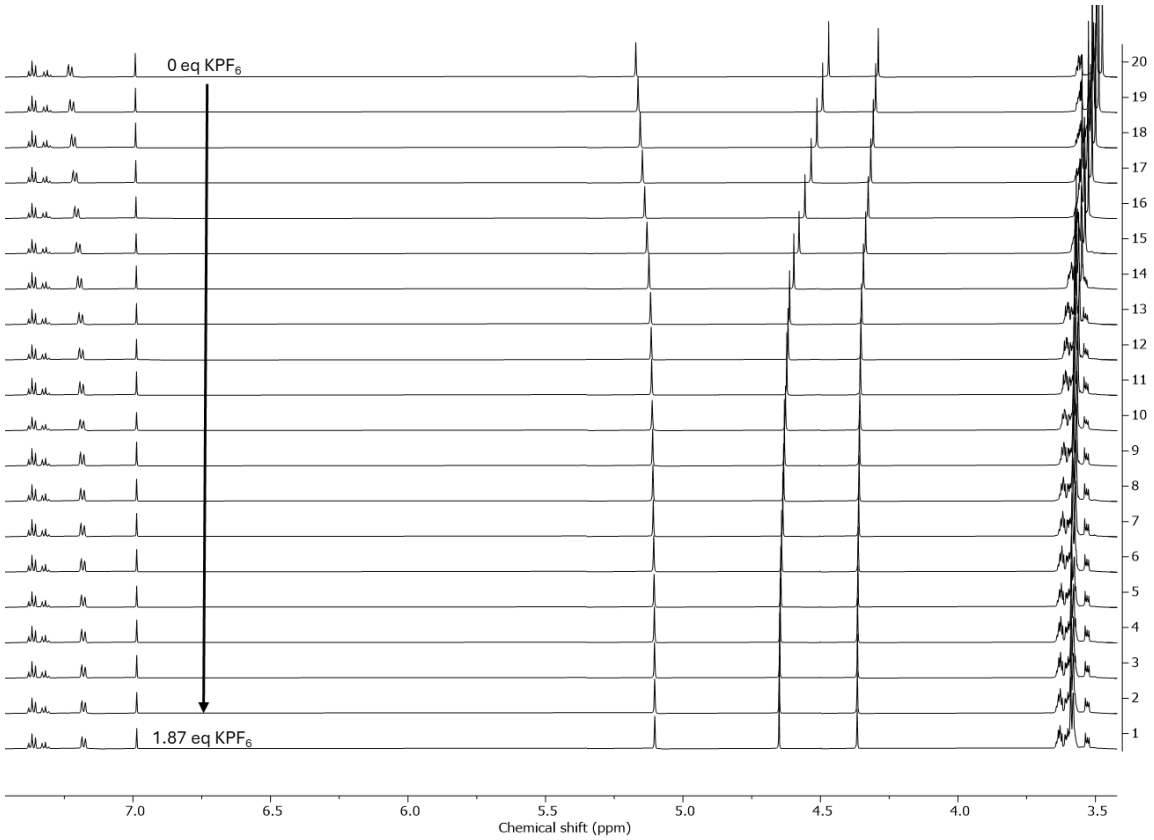

Figure S33. Stacked ^{1}H NMR spectrum with the increasing addition of the guest KPF_6 from 0 to 1.87 equivalents, host concentration [**ImBn21C7**] = 1.57 mM in CD_3CN at 20°C

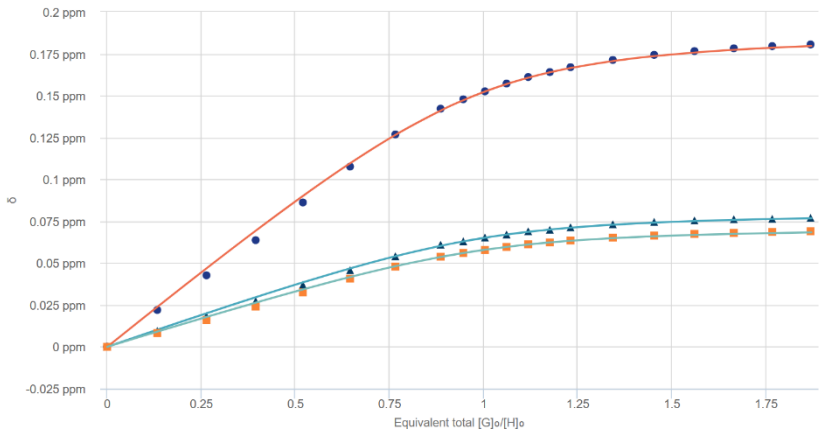

Figure S34. Fitted titration data on bindfit for a K_a of 13630.92 M^{-1} and fitting error of ± 4.7834 %

Trial 3

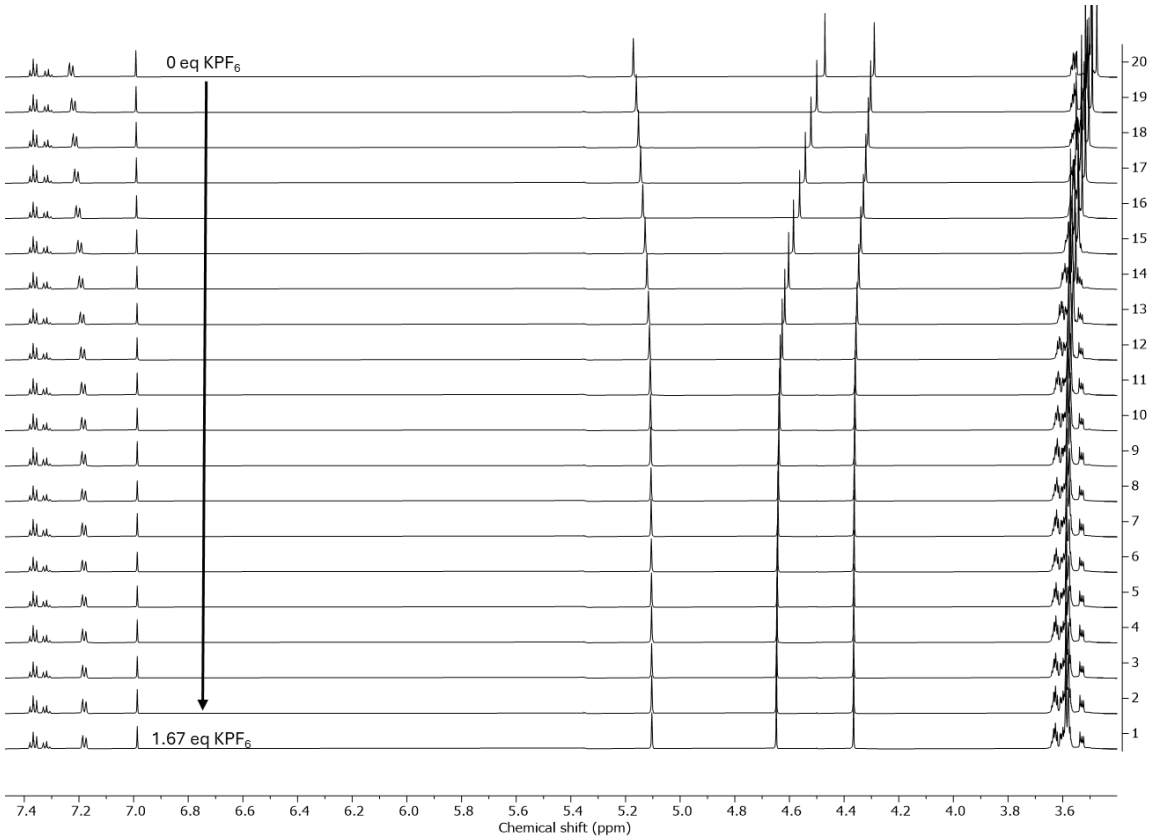

Figure S35. Stacked ^{1}H NMR spectrum with the increasing addition of the guest KPF_6 from 0 to 1.67 equivalents, host concentration [**ImBn21C7**] = 1.57 mM in CD_3CN at 20°C

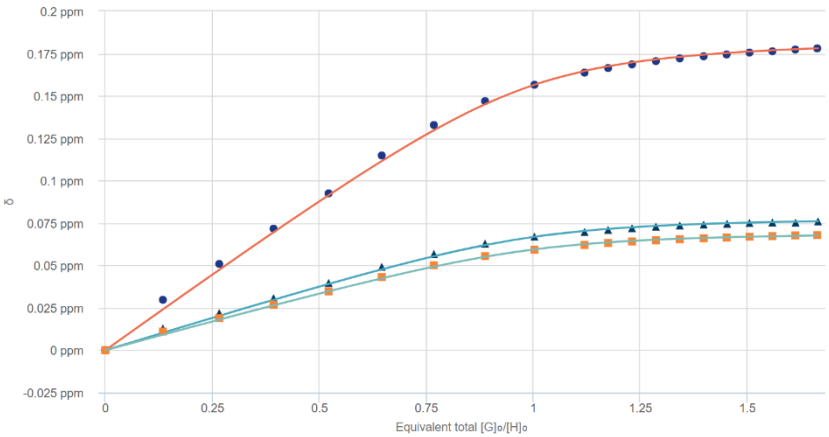

Figure S36. Fitted titration data on bindfit for a K_a of 21794.69 M^{-1} and fitting error of ± 6.1215 %

ImBn24C8 with $NaPF_6$

Trial 1

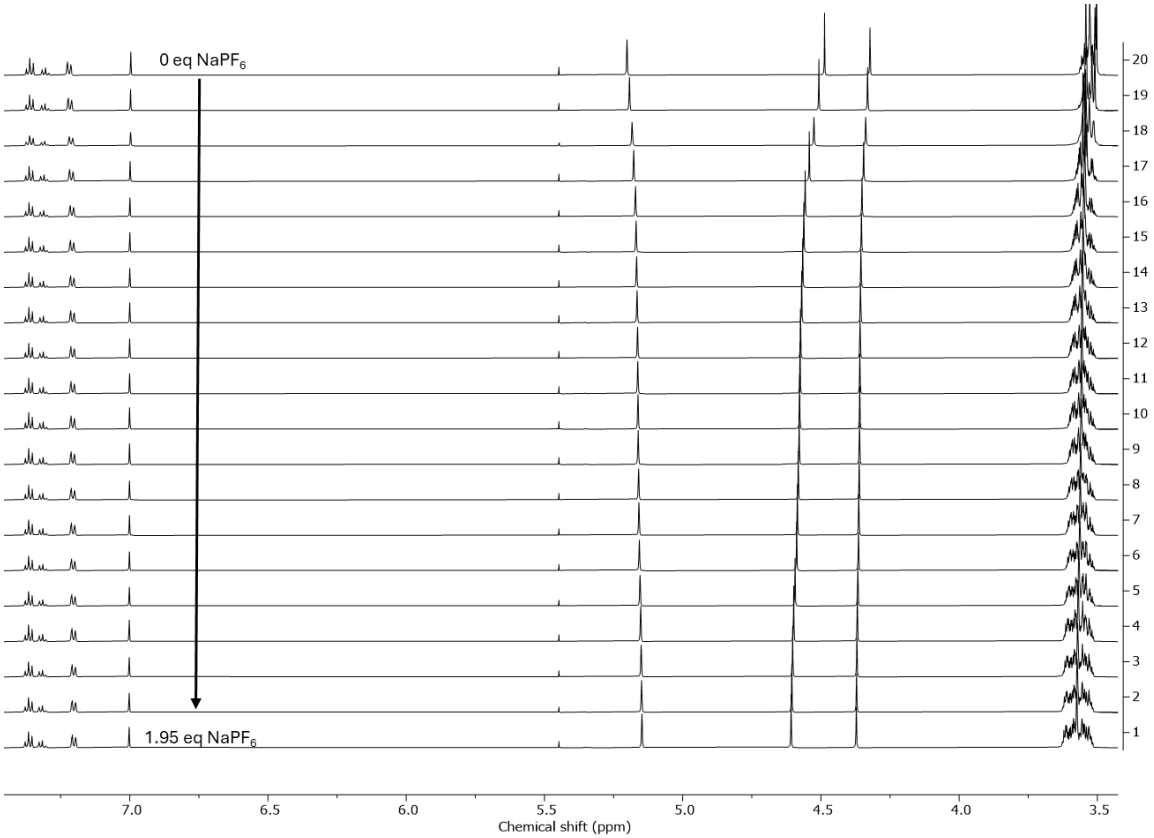

Figure S37. Stacked ^{1}H NMR spectrum with the increasing addition of the guest $NaPF_6$ from 0 to 1.95 equivalents, host concentration [**ImBn24C8**] = 1.41 mM in CD_3CN at 20°C

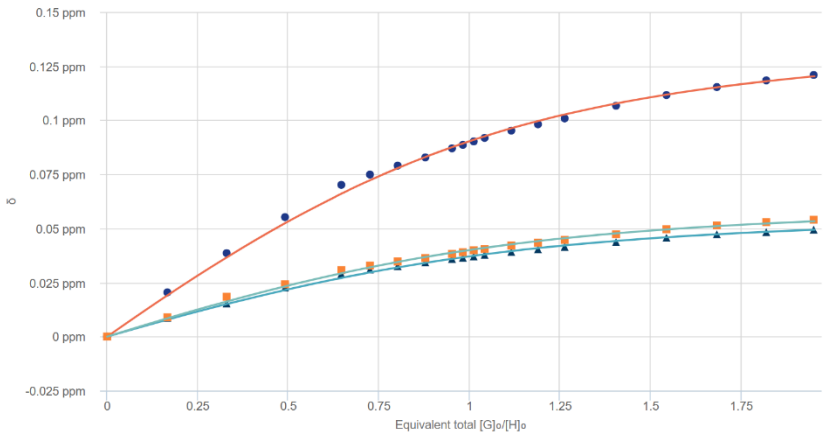

Figure S38. Fitted titration data on bindfit for a K_a of 3166.44 M^{-1} and fitting error of ± 2.3786 %

Trial 2

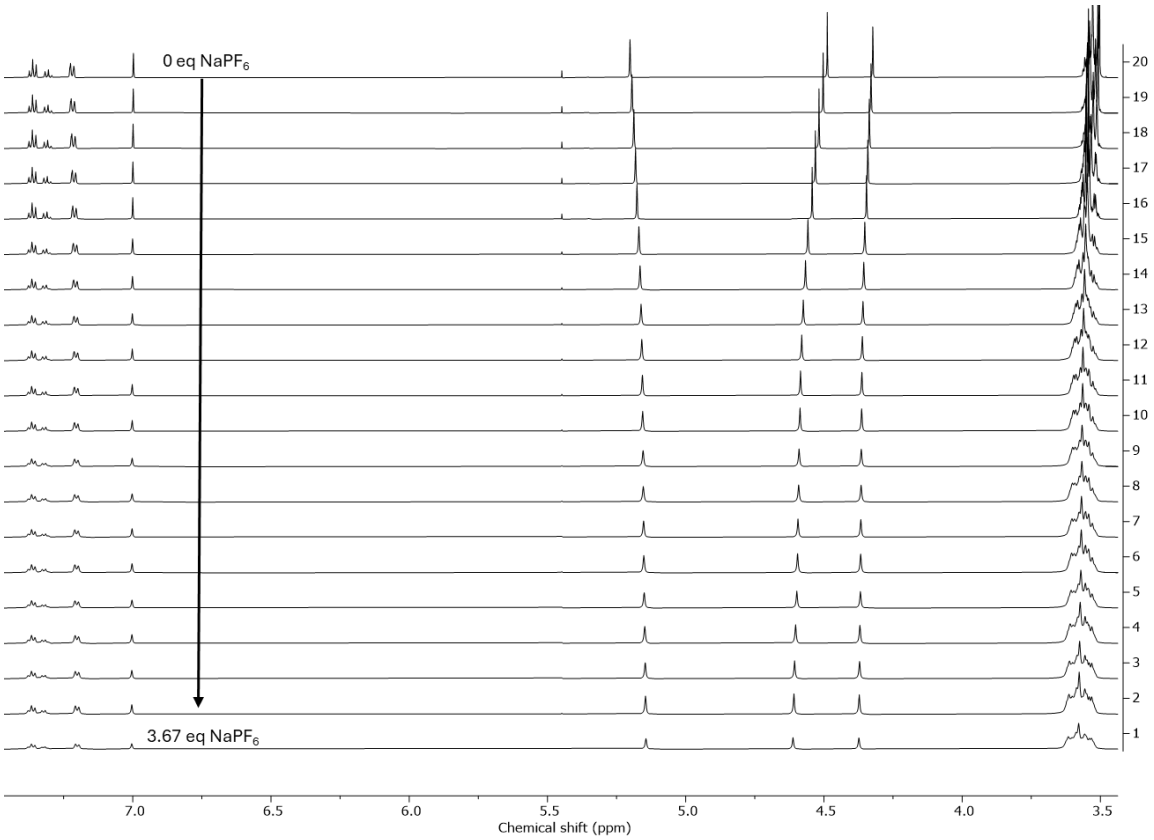

Figure S39. Stacked ^{1}H NMR spectrum with the increasing addition of the guest $NaPF_6$ from 0 to 3.67 equivalents, host concentration [**ImBn24C8**] = 0.70 mM in CD_3CN at 20°C

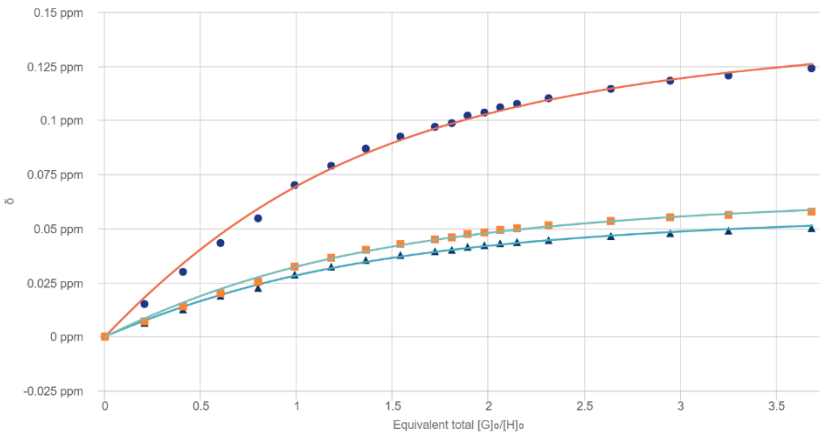

Figure S40. Fitted titration data on bindfit for a K_a of 2066.53 M^{-1} and fitting error of ± 2.1705 %

Trial 3

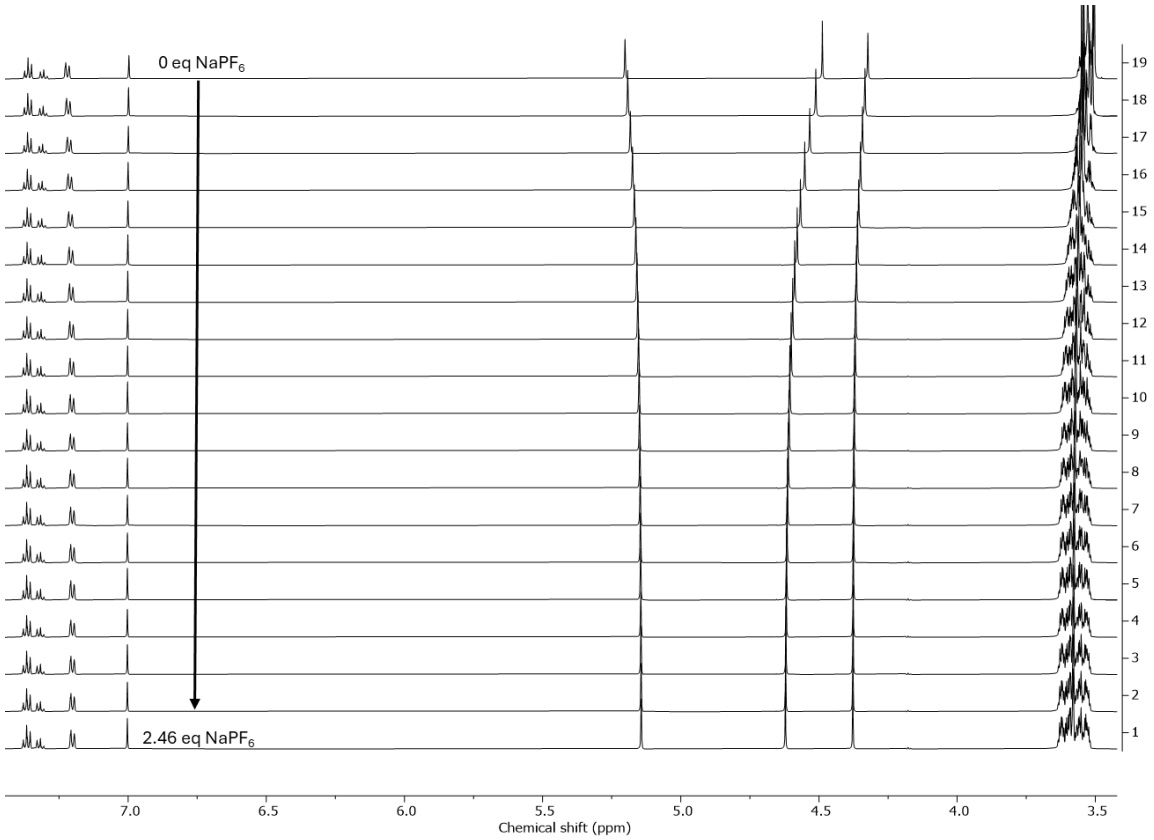

Figure S41. Stacked ^{1}H NMR spectrum with the increasing addition of the guest $NaPF_6$ from 0 to 2.46 equivalents, host concentration [**ImBn24C8**] = 1.48 mM in CD_3CN at 20°C

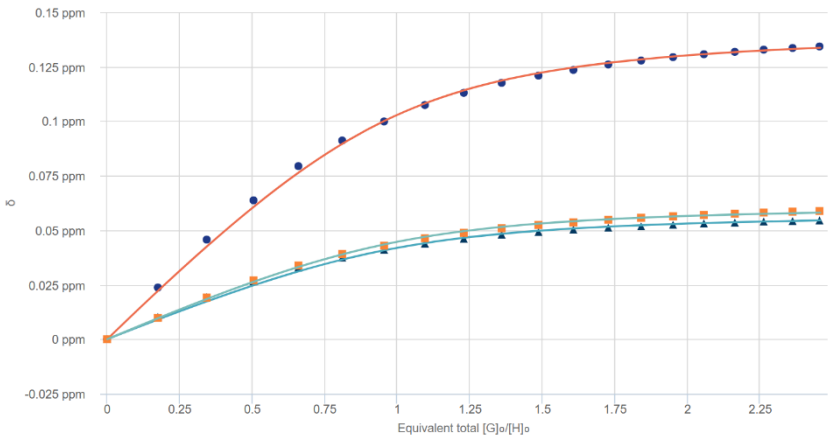

Figure S42. Fitted titration data on bindfit for a K_a of 6066.63 M^{-1} and fitting error of ± 3.2722 %

ImBn24C8 with KPF_6

Trial 1

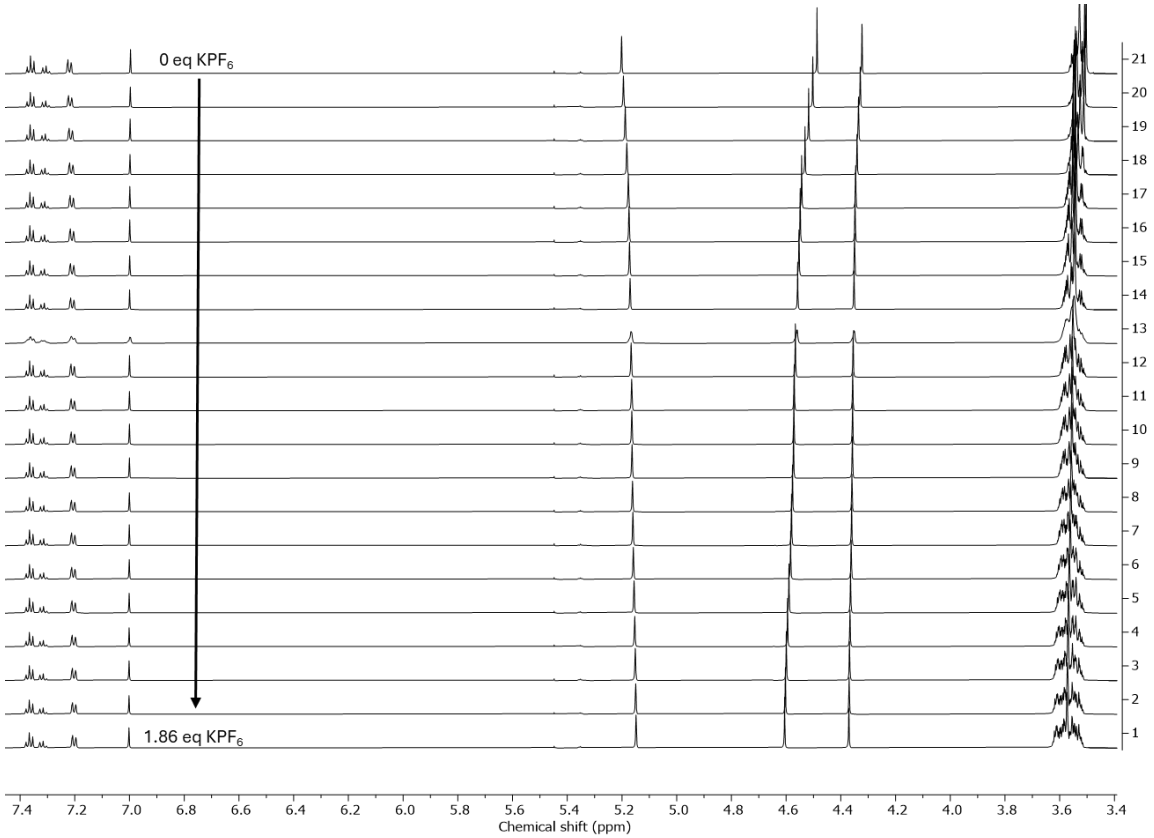

Figure S43. Stacked ^{1}H NMR spectrum with the increasing addition of the guest KPF_6 from 0 to 1.86 equivalents, host concentration [**ImBn24C8**] = 1.61 mM in CD_3CN at 20°C

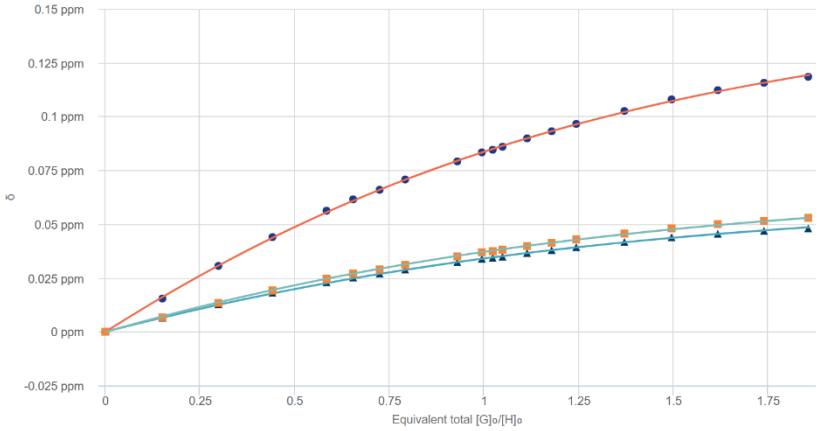

Figure S44. Fitted titration data on bindfit for a K_a of 1095.28 M^{-1} and fitting error of ± 0.4413 %

Trial 2

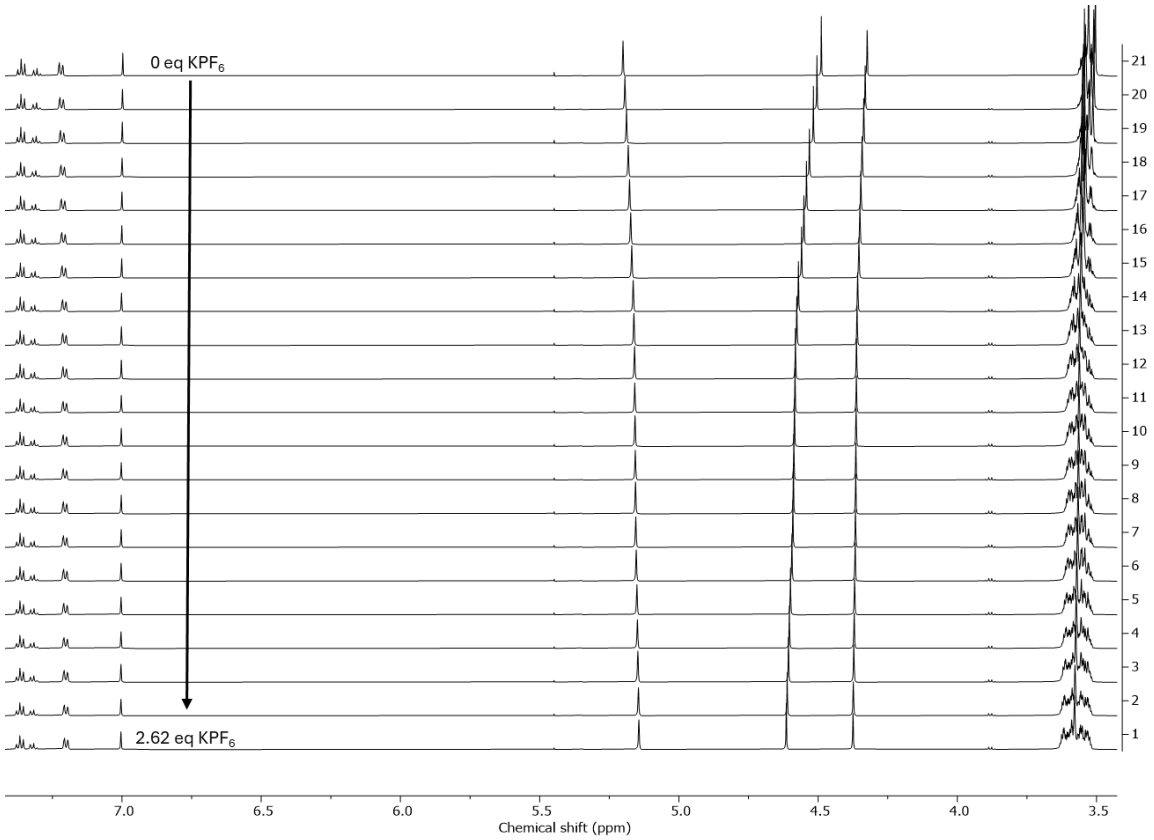

Figure S45. Stacked ^{1}H NMR spectrum with the increasing addition of the guest KPF_6 from 0 to 2.62 equivalents, host concentration [**ImBn24C8**] = 0.98 mM in CD_3CN at 20°C

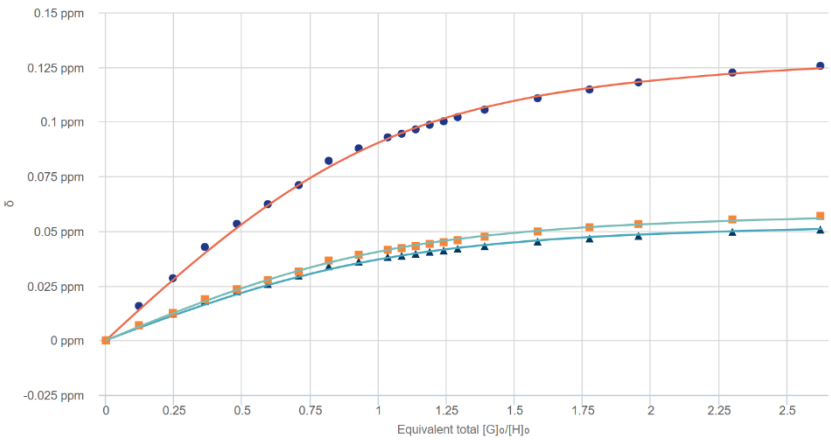

Figure S46. Fitted titration data on bindfit for a K_a of 5749.64 M^{-1} and fitting error of ± 2.2975 %

Trial 3

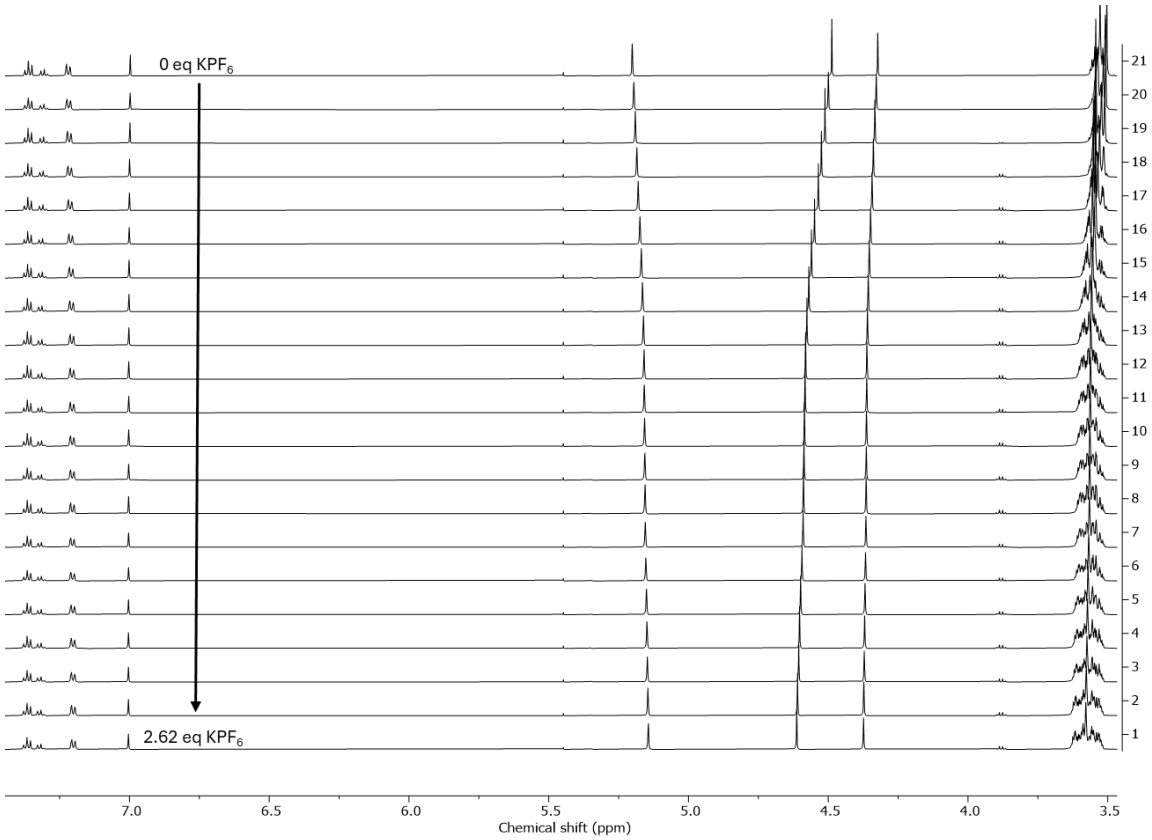

Figure S47. Stacked ^{1}H NMR spectrum with the increasing addition of the guest KPF_6 from 0 to 2.62 equivalents, host concentration [**ImBn24C8**] = 0.98 mM in CD_3CN at 20°C

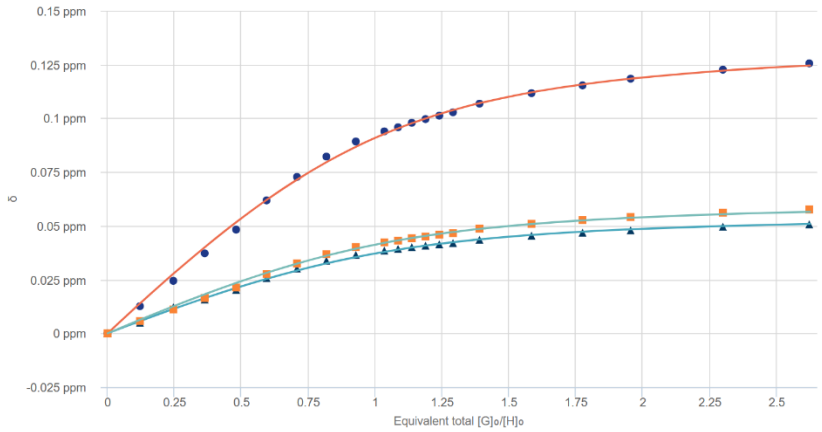

Figure S48. Fitted titration data on bindfit for a K_a of 5992.80 M^{-1} and fitting error of ± 2.9172 %

K_A*C_0	*ImBn15C5*		*ImBn18C6*		*ImBn21C7*		*ImBn24C8*		*Py18C6*	
	Na^+	*K^+*	*Na^+*	*K^+*	*Na^+*	*K^+*	*Na^+*	*K^+*	*Na^+*	*K^+*
T1	*0.97*	*1.22*	*23.62*	*119.9*	*8.72*	*26.45*	*4.46*	*1.54*	*0.98*	*1.65*
T2	*0.55*	*1.07*	*19.10*	*121.4*	*8.86*	*21.40*	*1.44*	*5.63*	*0.99*	*2.46*
T3	*1.03*	*1.40*	*19.73*	*100.4*	*11.5*	*34.21*	*8.97*	*5.87*	*1.23*	*1.70*

Table S1 – Values of K_A*C_0 for all the titrations.

The titrations of ImBn18C6 should have been performed again at lower dilutions as the values are above 100 which led to less reliable data.

Pseudorotaxane formation

The association constant (K_A) of the different pseudorotaxane systems was calculated using the single point method. Each ^1H NMR analysis was performed approximately 10 minutes after solution preparation. The spectra did not change after 24h, indicating that the equilibrium is reached rapidly. For improved accuracy, the relaxation delay for each ^1H NMR experiment was set at 30s with 16 scans acquired. The reported errors represent the standard deviation of the different K_A values obtained from these concentrations. For the **ImBn24C8** + **DBA.HPF$_6$** system, two K_A values were obtained at concentrations of 0.5 mM and 1 mM, giving 10688 M^{-1} and 22474 M^{-1} respectively. Due to the limitation of the single point method, we can only state with confidence that K_A > 10000. The higher concentration solutions could not be used to determine K_A as the signal to noise ratio was insufficient to allow reliable integration of the signals.

Im21C7 and DBA.HPF$_6$

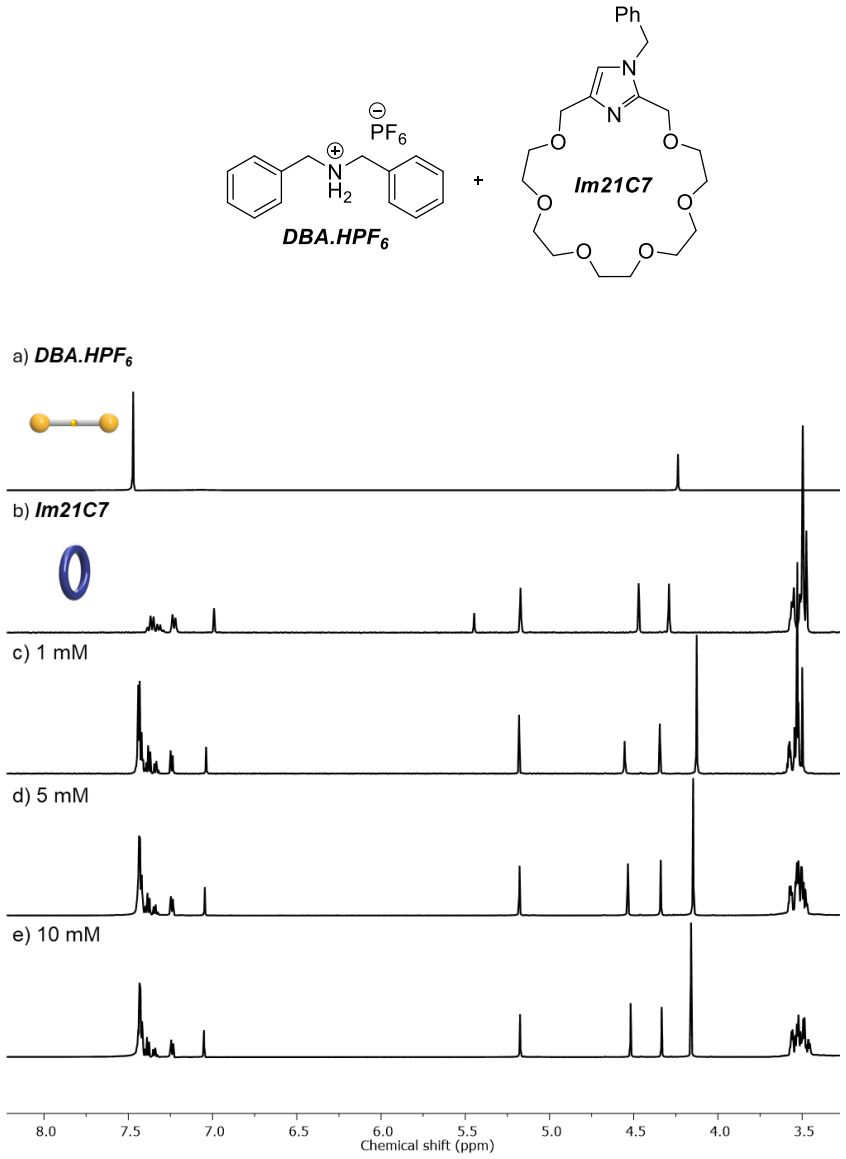

Figure S49. ^{1}H NMR spectrum in MeCN at 20°C of a) DBA.HPF6 b) Im21C7 c) 1 mM 1:1 mixture of **Im21C7** and **DBA.HPF$_6$** d) 5 mM 1:1 mixture of Im21C7 and **DBA.HPF$_6$** e) 10 mM 1:1 mixture of **Im21C7** and **DBA.HPF$_6$**.

DB24C8 and DBA.HPF6

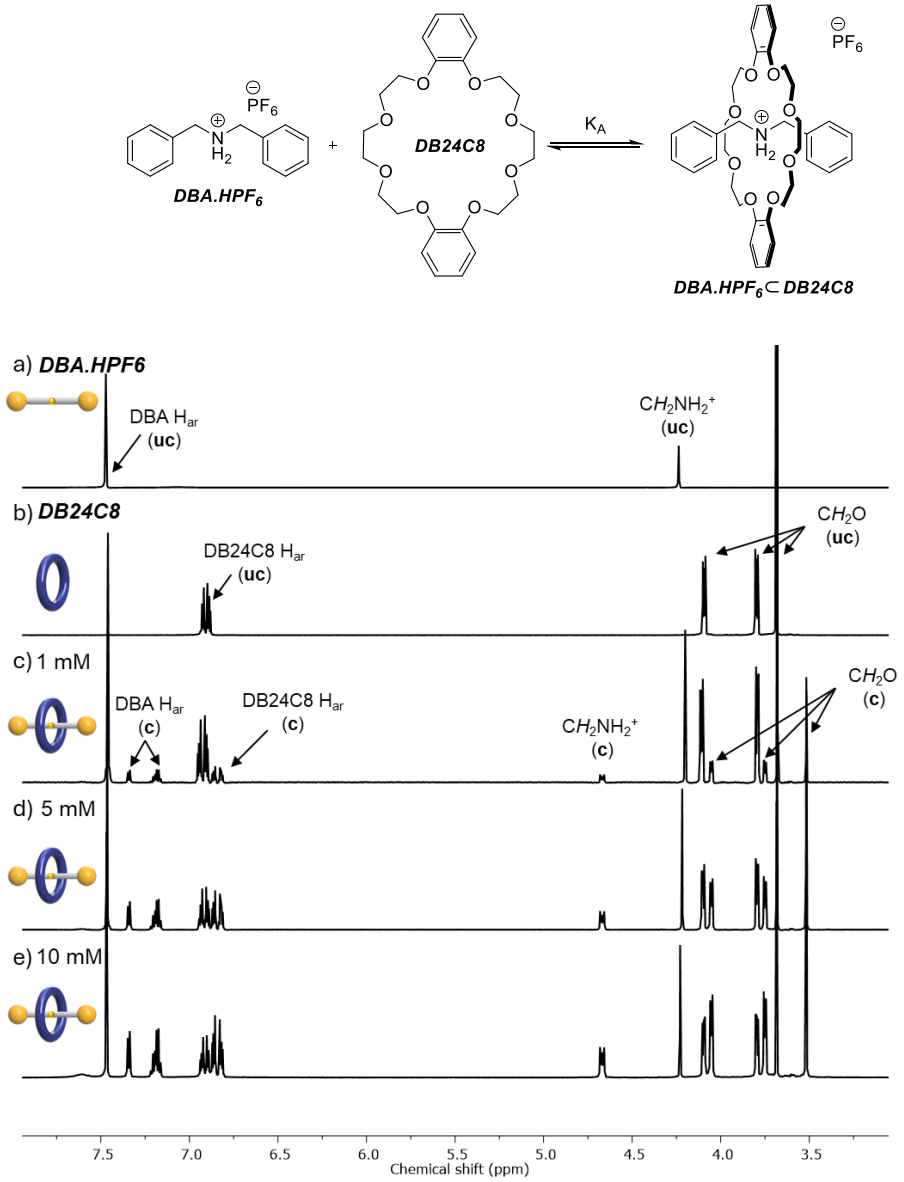

Figure S50. ^{1}H NMR spectrum in MeCN at 20°C of a) **DBA.HPF$_6$** b) **DB24C8** c) 1 mM 1:1 mixture of **DB24C8** and **DBA.HPF$_6$,** computed K_a = 323 M^{-1} d) 5 mM 1:1 mixture of **DB24C8** and **DBA.HPF$_6$,**

computed K_a = 349 M^{-1} e) 10 mM 1:1 mixture of **DB24C8** and **DBA.HPF$_6$**, computed K_a = 370 M^{-1}. (uc) refers to the free species and (c) to the complexed species

P24C8 and DBA.HPF$_6$

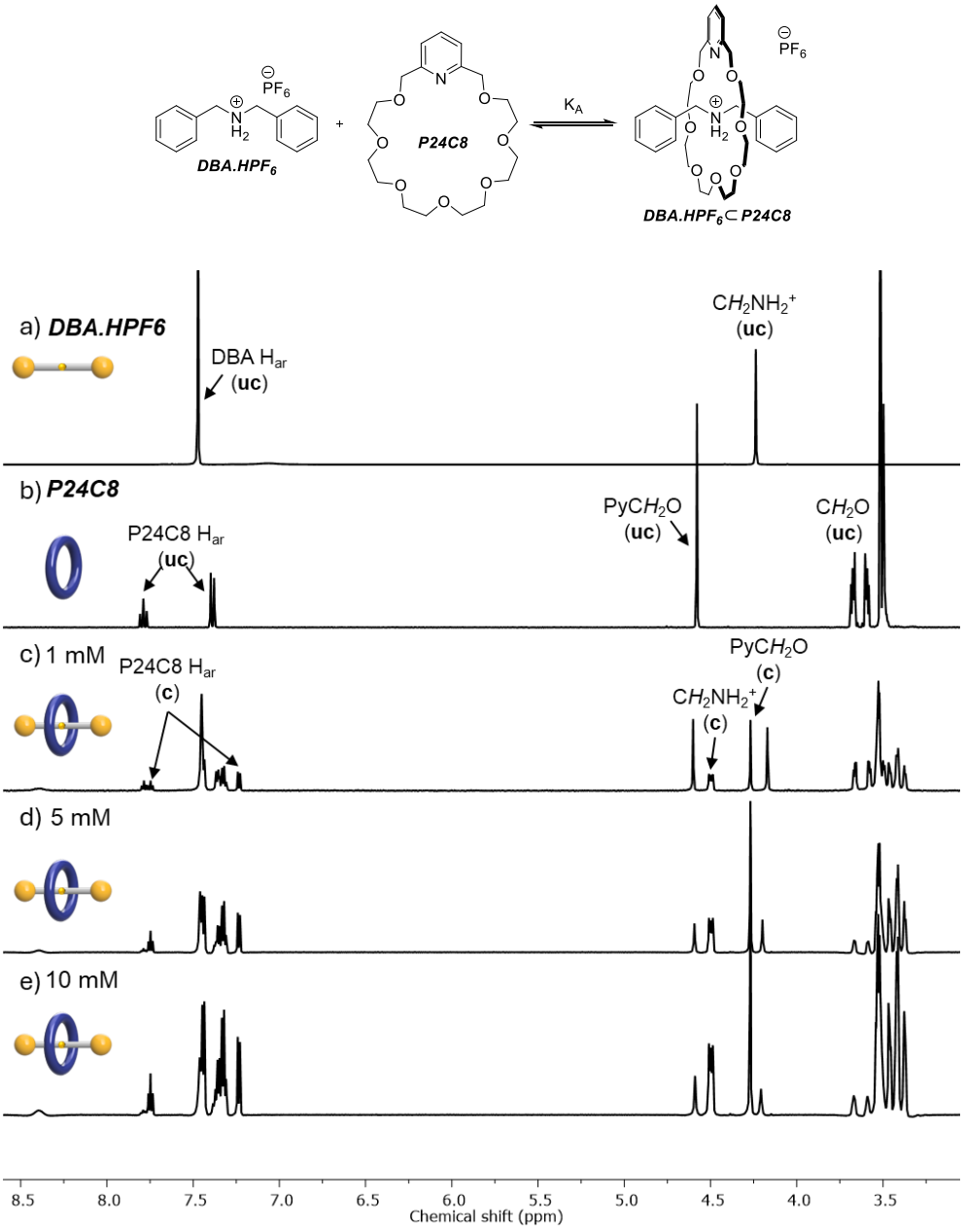

Figure S51. ^{1}H NMR spectrum in MeCN at 20°C of a) **DBA.HPF6** b) **P24C8** c) 1 mM 1:1 mixture of **P24C8** and **DBA.HPF$_6$**, computed KA = 1726 M-1 d) 5 mM 1:1 mixture of **P24C8** and **DBA.HPF$_6$**, computed K_a = 2044 M^{-1} e) 10 mM 1:1 mixture of **P24C8** and **DBA.HPF$_6$**, computed K_a = 2113 M^{-1}. (uc) refers to the free species and (c) to the complexed species.

Im24C8 and DBA.HPF$_6$

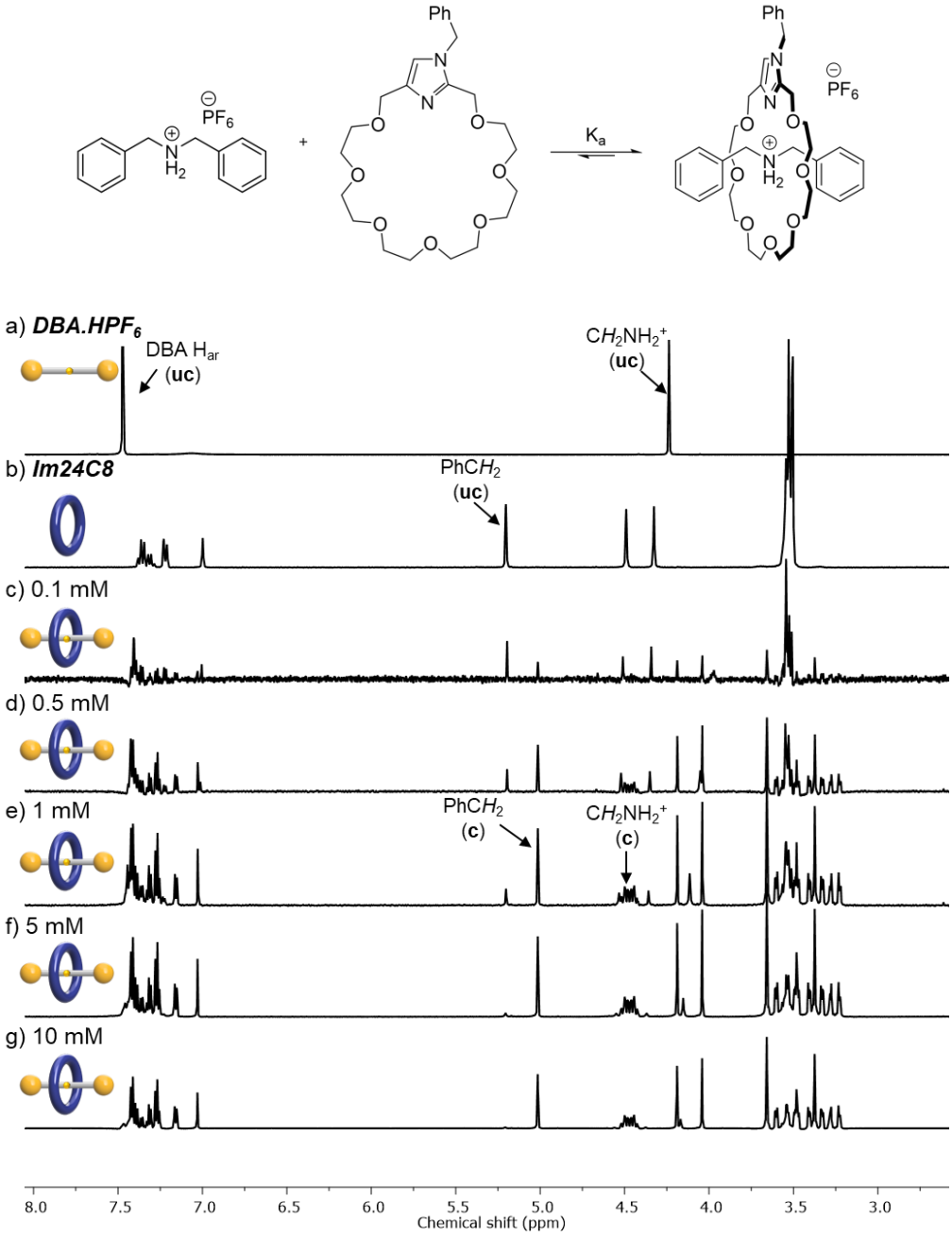

Figure S52. ^{1}H NMR spectrum in MeCN at 20°C of a) **DBA.HPF$_6$** b) **Im24C8** c) 0.1 mM 1:1 mixture of **Im24C8** and **DBA.HPF$_6$** d) 0.5 mM 1:1 mixture of **Im24C8** and **DBA.HPF$_6$**, computed K_A = 10668 M^{-1} e) 1 mM 1:1 mixture of **Im24C8** and **DBA.HPF$_6$**, computed K_A = 22474 M^{-1} f) 5 mM 1:1 mixture of **Im24C8** and **DBA.HPF$_6$**, computed K_A = 50169 M^{-1} g) 10 mM 1:1 mixture of **Im24C8** and **DBA.HPF$_6$**. (**uc**) refers to the free species and (**c**) to the complexed species.

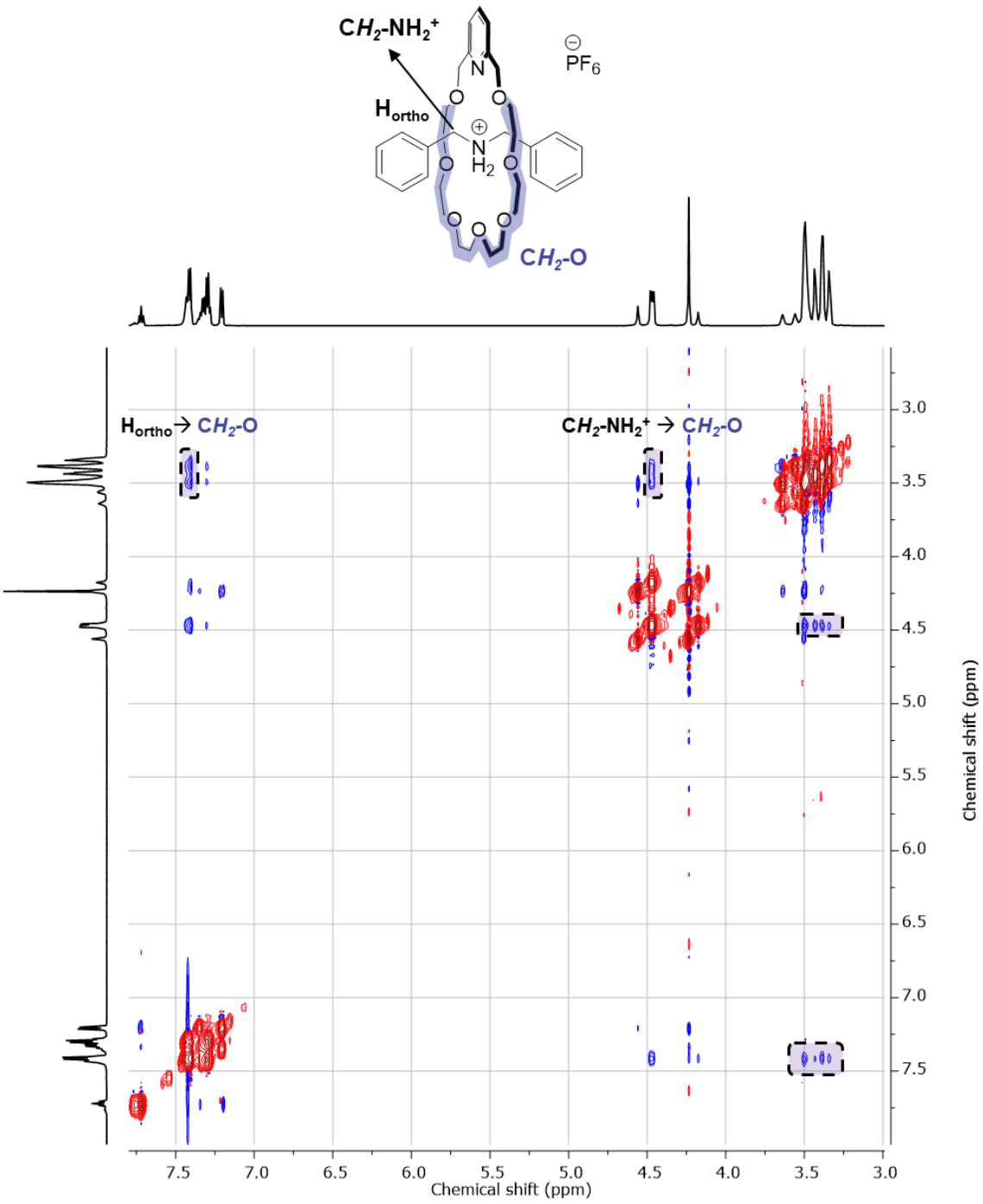

Figure S54. ^{1}H-^{1}H NOESY spectrum in MeCN at 20°C for a 10 mM 1:1 mixture of **P24C8** and **DBA.HPF$_6$**. EXSY correlations are in red and NOESY correlations in blue. Important NOESY correlations are highlighted.

X-Ray Crystallography Data

Im18C6•KPF$_6$ was crystallized from $CDCl_3$/Hexane in an NMR tube, crystals were stable outside the mother liquid at ambient conditions, but crystallization always led to the formation of crystal clusters that needed to be broken up to harvest a single crystal.

Diffraction data were recorded on a MAR345 image plate detector using MoKα radiation generated by an Incoatec IμS microfocus source (Montel mirrors) at ambient conditions. The unit-cells, data reduction and absorption correction (multi-scan method) were conducted using CrysAlisPro[3] software package. The structure was solved by dual space direct methods SHELXT[4] and refinement by full-matrix least-squares against F2 using SHELXL-2019/3[5]. All non-hydrogen atoms were refined anisotropically and hydrogen atoms were placed at calculated positions and refined in riding mode.

The crown ether is disordered and could be refined in two parts, the observed disorder of the macrocycle also causes the coordinated PF_6^- anion to be rotationally disordered in the equatorial plane.

CCDC 2556349-2556350 include the supplementary crystallographic data and can be downloaded free of charge from The Cambridge Crystallographic Data Centre via www.ccdc.cam.ac.uk/structures.

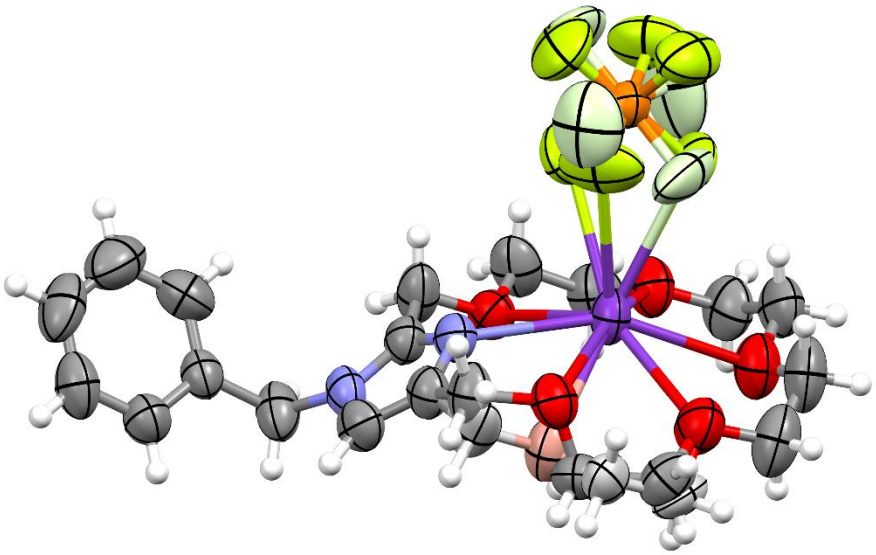

Figure S55: Ortep representation of **Im18C6•KPF$_6$**, the minor disordered parts are drawn in a lighter shade.

Table S2 contains the crystal and refinement details for the structure determination of **Im18C6•KPF_6**

Identification code	**Im18C6•KPF_6**
Empirical formula	$C_{20}\,H_{28}\,F_6\,K\,N_2\,O_5\,P$
Formula weight	560.51
Temperature (K)	297(2)
Wavelength (Å)	0.71073
Crystal system	Triclinic
Space group	*P*1
Unit cell dimensions (Å,°)	a = 8.5281(8)
	b = 8.5785(16)
	c = 9.6251(12)
	□= 76.799(13)
	□= 76.785(10)
	□ = 70.147(13)
Volume (Å^3)	635.97(17)
Z	1
Density (calculated) (g/cm^3)	1.464
Absorption coefficient (mm^{-1})	0.349
F(000)	290
Crystal size (mm^3)	0.20x 0.18 x 0.03
Theta range for data collection (°)	2.559 to 24.401
Reflections collected	7216
Independent reflections	4042 [$R_{(int)}$ = 0.0434]
Completeness to □ = 24.401° (%)	99.7
Absorption correction	Semi-empirical from equivalents
Max. and min. transmission	1.00000 and 0.77605
Refinement method	Full-matrix least-squares on F^2
Data / restraints / parameters	4042 / 226 / 390
Goodness-of-fit on F^2	1.053
Final R indices [I>2s(I)]	R1 = 0.0499, wR2 = 0.1191
R indices (all data)	R1 = 0.0666, wR2 = 0.1311
Absolute structure parameter	0.04(4)
□□ (max,min)(e.Å^{-3})	0.232, -0.261

† Twinned crystal, refined against HKLF5 formatted data imposing Merge 0.

Computational Details

Conformational sampling of free Im18c6 was performed with CREST (version 2.12) [6] /xTB (version 6.7.0) [7] at the GFN2-xTB[8] level with the ALPB[9] implicit solvation model for acetonitrile, using the quick sampling protocol. All structures within 1.0 kcal/mol of the minimum energy structure (8 total), were subsequently reoptimized with ORCA 5.0.3[10] at the ωB97X-D4/def2-TZVPP[11,12] level using the RIJCOSX[13] approximation with the def2/J auxiliary basis set[14], TightSCF convergence criteria, and the CPCM[15] implicit solvation model for acetonitrile. Frequency calculations at the same level of theory were used to confirm the absence of imaginary frequencies. The final energy and coordinates for the lowest energy structure are provided in Table S3.

Table S3 – Final electronic energy and coordinates for optimized structure of free **Im18C6**

Final Gibbs Free Energy = -1265.14893123 Eh							
Atom	Coordinates			Atom	Coordinates		
C	-4.291753903	0.729300201	1.785897388	H	4.949937927	-1.998377196	-0.774952335
H	-3.842062042	1.471667323	2.437909348	O	4.04044255	-0.972216303	0.690171861
C	-5.604849623	0.329156578	1.993949646	C	3.079869513	-1.017249459	1.734456051
H	-6.177786166	0.76201975	2.806519908	H	3.289899053	-1.8640894	2.403282558
C	-6.180074511	-0.631454087	1.16756323	H	2.073103926	-1.147018632	1.326920751
H	-7.203302123	-0.949879413	1.331724877	C	3.134829297	0.271235939	2.526909931
C	-5.433280959	-1.182577091	0.134176642	H	2.486656915	0.160109105	3.400458824
H	-5.872507641	-1.933558434	-0.513056675	H	4.154631168	0.461311558	2.881486547
C	-4.11831725	-0.777796672	-0.075061793	O	2.653736273	1.387789746	1.791241387
H	-3.54442655	-1.219642904	-0.881646985	C	3.67128768	2.115286584	1.115803496
C	-3.539730299	0.181409276	0.748341395	H	4.255365709	1.452821542	0.471290866
C	-2.123327497	0.673399754	0.539111326	H	4.349800897	2.571040986	1.850356931
H	-2.128290755	1.631230402	0.020034213	C	3.046264057	3.212933827	0.284378333
H	-1.639459823	0.83343071	1.503603406	H	2.329119938	3.781122137	0.889324832
N	-1.30161035	-0.245087963	-0.230949201	H	3.841152816	3.892005259	-0.033548036
C	-0.998770305	-0.174304322	-1.552371727	O	2.421633984	2.751211557	-0.904644213
N	-0.281552045	-1.210311992	-1.935133675	C	1.081113232	2.30939676	-0.759112215
C	-0.126219033	-1.996658601	-0.813502432	H	0.538337556	2.962676458	-0.065372102
C	-0.753695494	-1.406059142	0.245985002	H	1.045306587	1.289249904	-0.365946417
C	0.653449827	-3.276203214	-0.824010618	C	0.43361738	2.401200988	-2.134966862
H	0.119487839	-4.049372423	-0.269859285	H	0.608736029	3.402555728	-2.535658374

H	0.775446789	-3.613108524	-1.860444454	H	0.876955192	1.674461781	-2.82312162
O	1.924088351	-3.166481282	-0.190094549	O	-0.976075246	2.220708155	-2.053555832
C	2.855000939	-2.39940987	-0.940204774	C	-1.445359674	0.940608418	-2.447513393
H	2.418248651	-1.439041867	-1.238314668	H	-1.115745033	0.699027372	-3.462172713
H	3.125082717	-2.948458112	-1.85208516	H	-2.535030997	1.01504532	-2.445485667
C	4.099325934	-2.14489723	0.10727743	H	-0.855680429	-1.698915776	1.279183257
H	4.299749997	-3.022835564	0.521276649				

^{1}H and ^{13}C characterization data

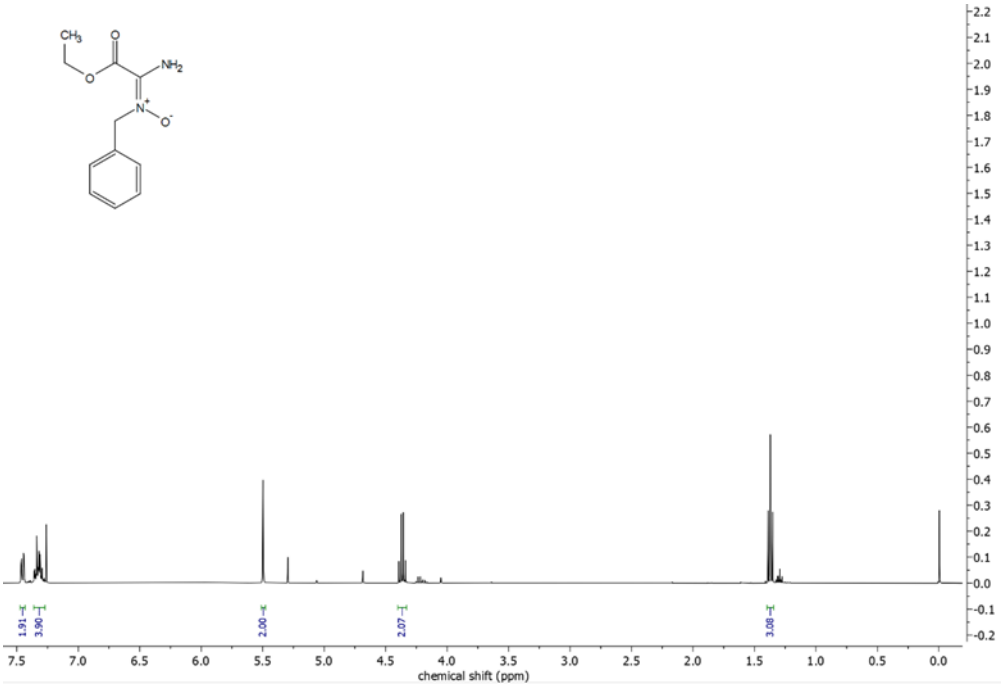

Figure S56 – ^{1}H NMR spectrum in CDCl3 of (Z)-1-amino-N-benzyl-2-ethoxy-2-oxoethan-1-imine oxide (**1**)

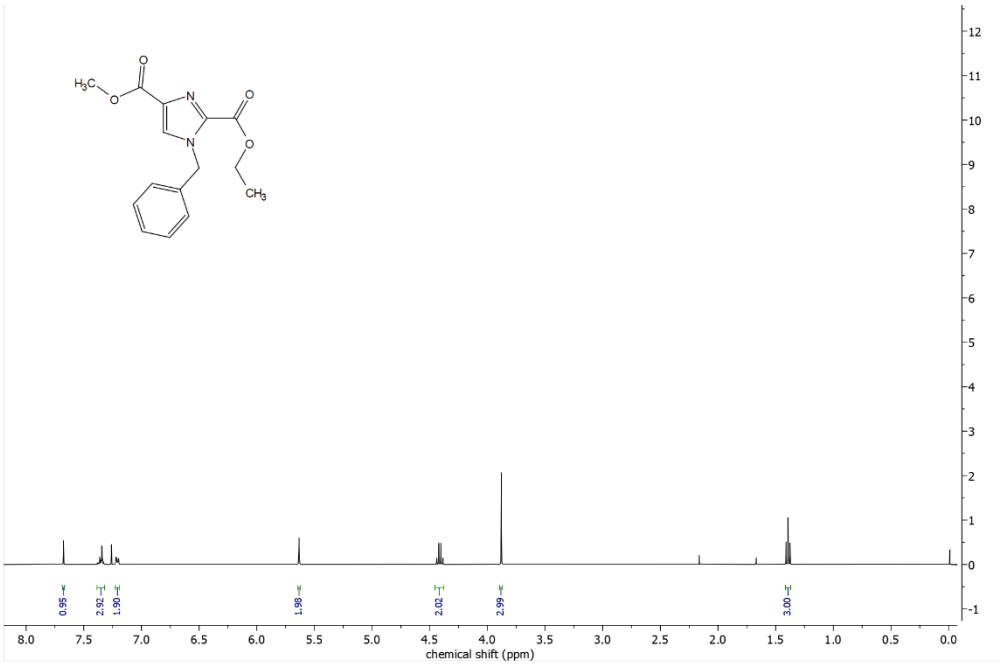

Figure S57: ^{1}H NMR spectrum in $CDCl_3$ of 2-ethyl 4-methyl 1-benzyl-1H-imidazole-2,4-dicarboxylate (**2**)

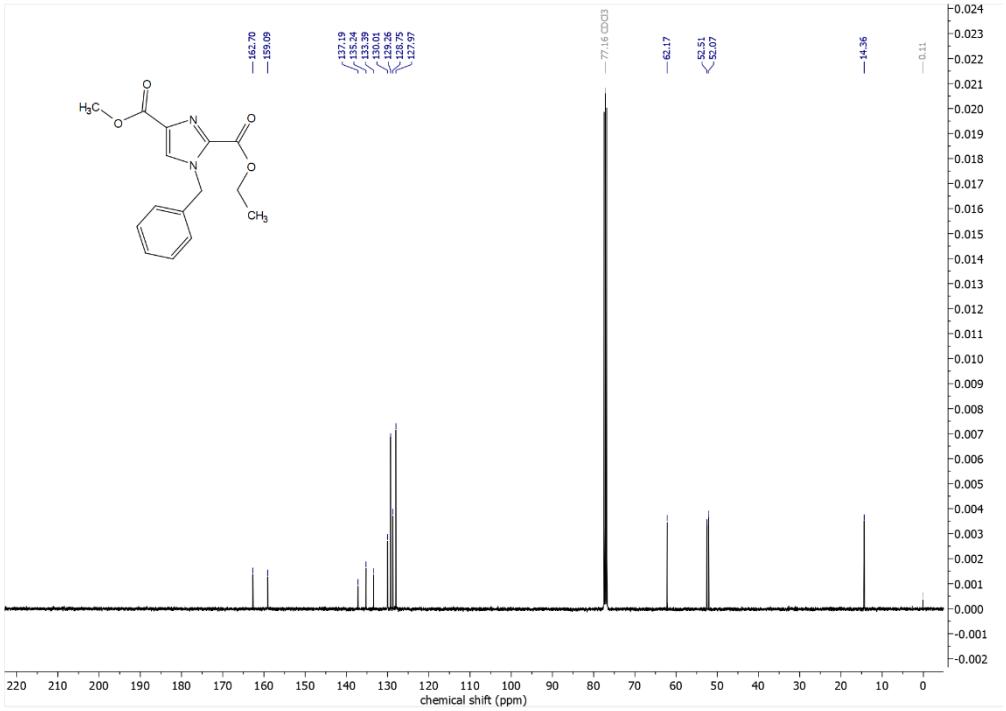

Figure S58: ^{13}C NMR spectrum in $CDCl_3$ of 2-ethyl 4-methyl 1-benzyl-1H-imidazole-2,4-dicarboxylate (**2**)

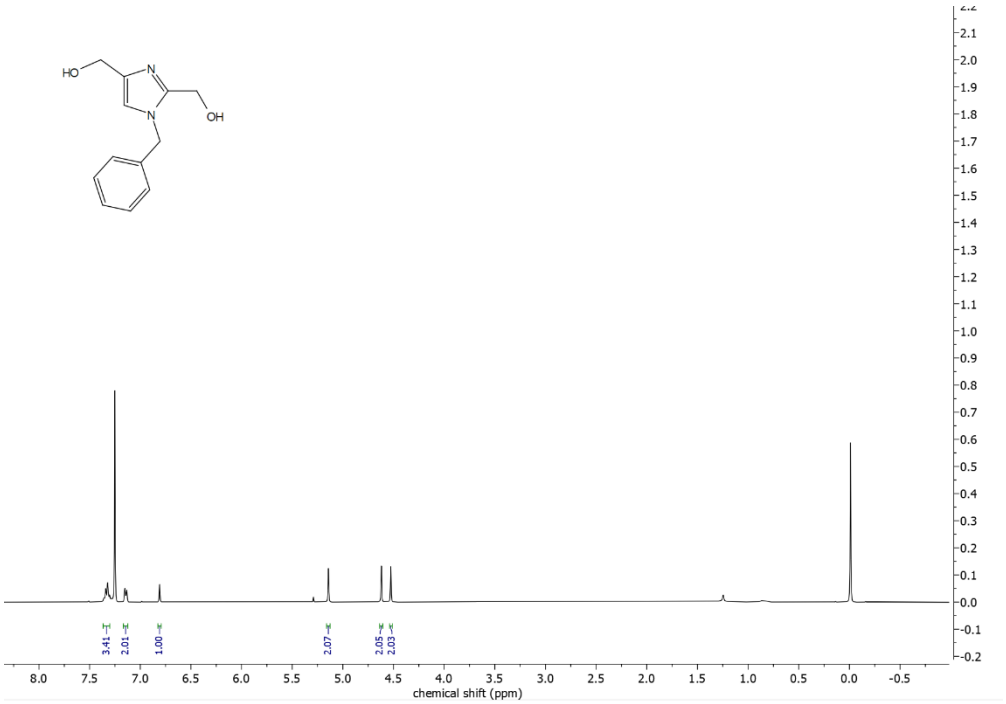

Figure S59: ^{1}H NMR spectrum in $CDCl_3$ of (1-benzyl-1H-imidazole-2,4-diyl)dimethanol (**3**)

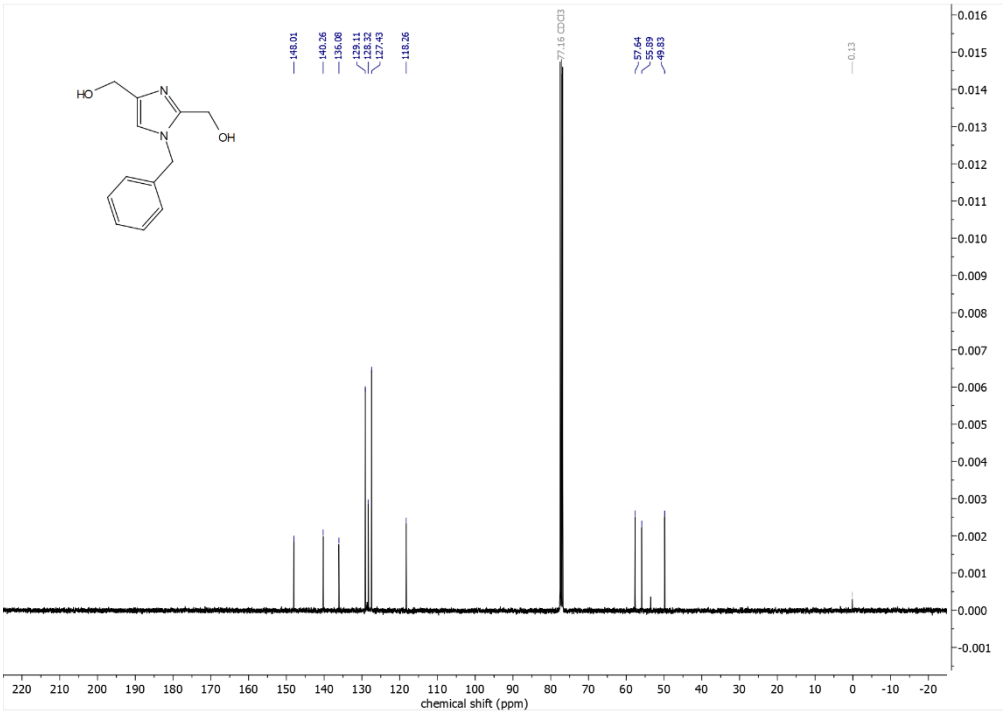

Figure S60 : ^{13}C NMR spectrum in $CDCl_3$ of (1-benzyl-1H-imidazole-2,4-diyl)dimethanol (**3**)

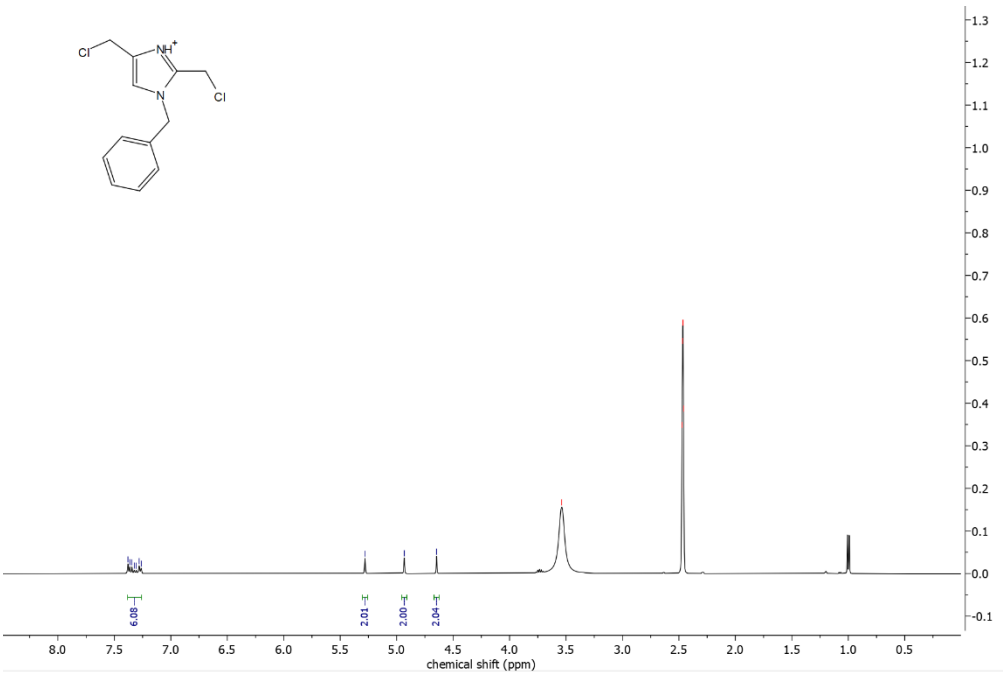

Figure S61: ^{1}H NMR spectrum in dmso of (**4**)

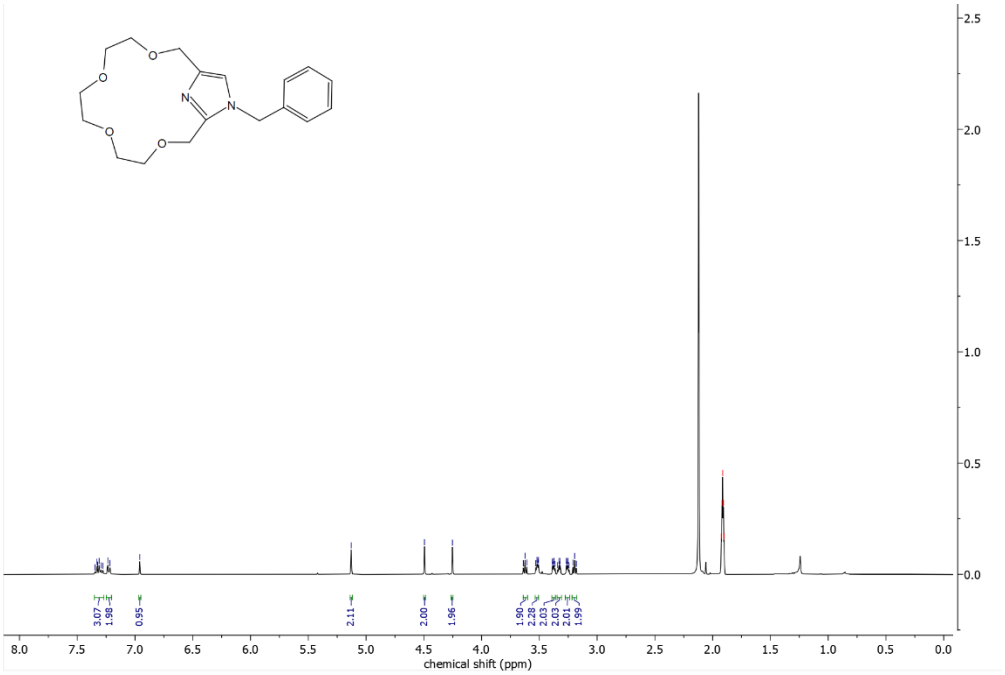

Figure S62: ^{1}H NMR spectrum in CD_3CN of **ImBn**15C5

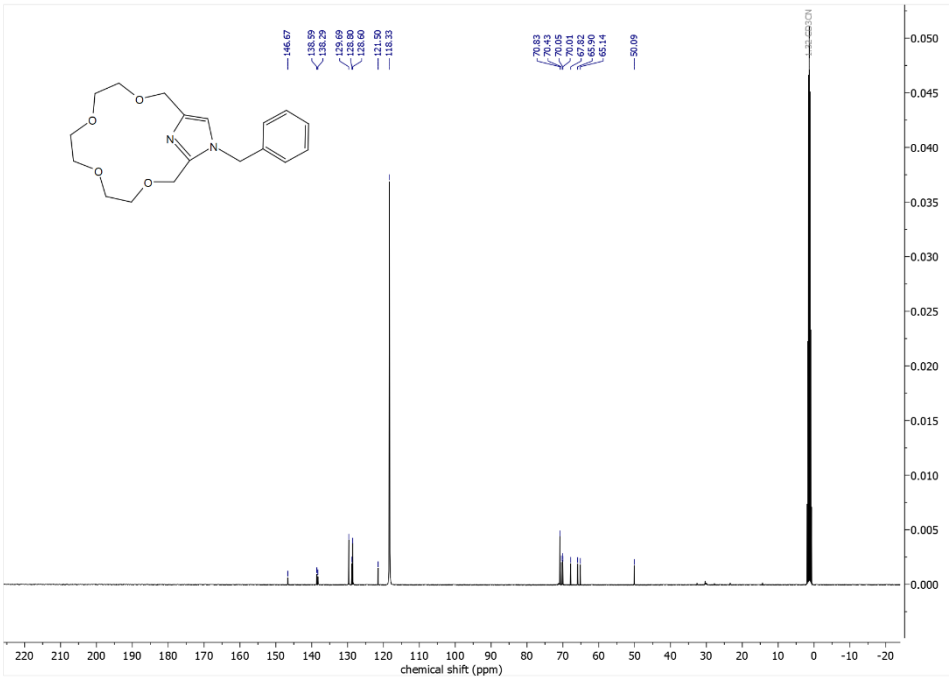

Figure S63: ^{13}C NMR spectrum in CD_3CN of **ImBn15C5**

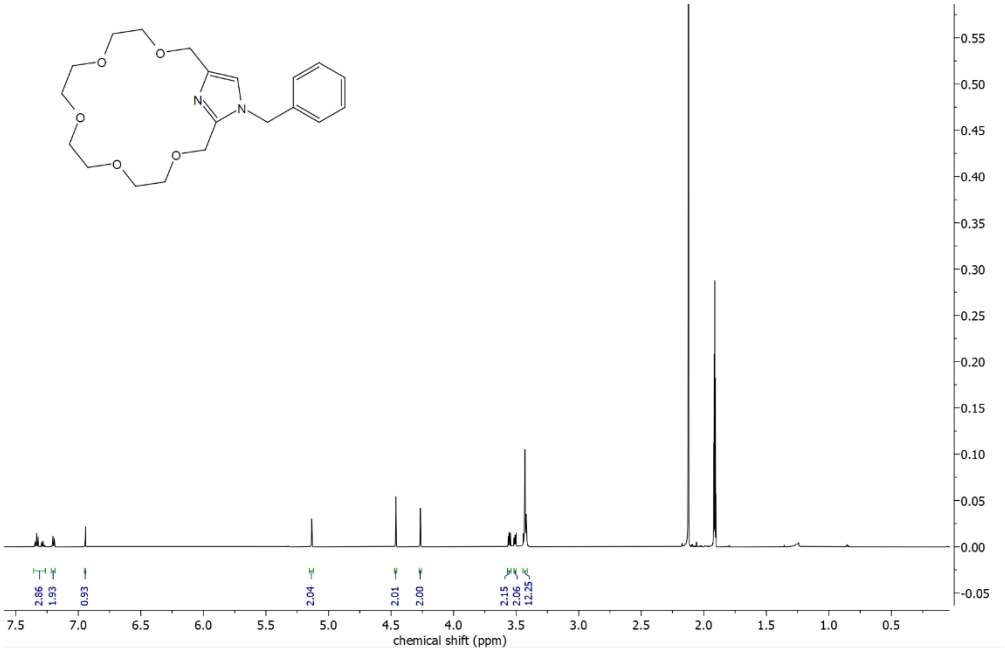

Figure S64: ^{1}H NMR spectrum in CD_3CN of **ImBn18C6**

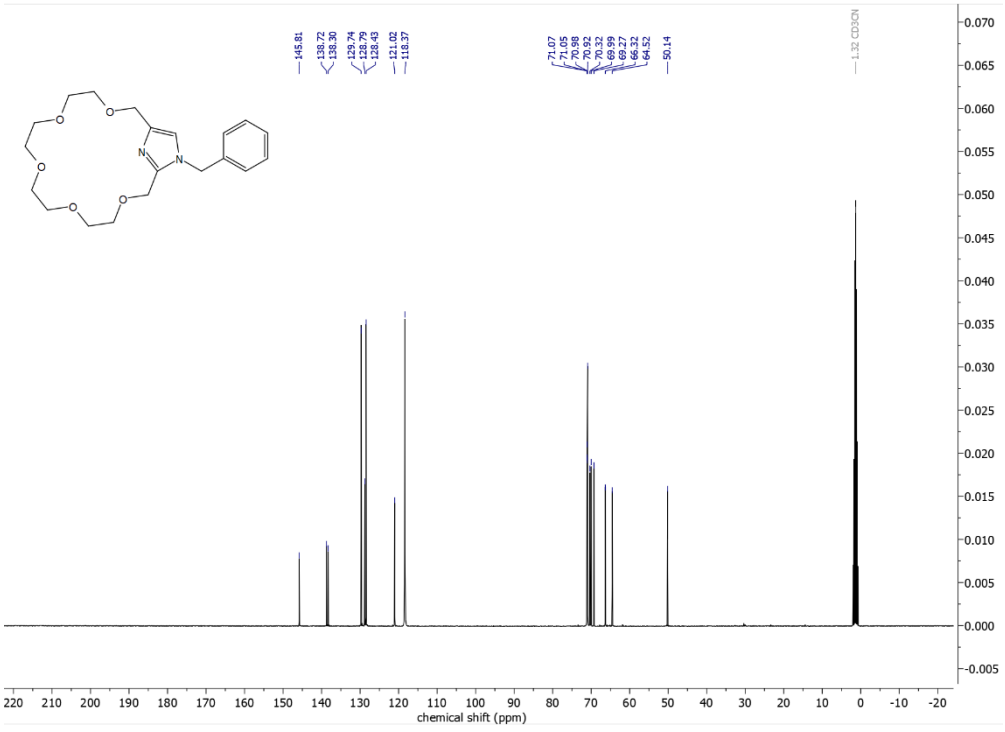

Figure S65: ^{13}C NMR spectrum in CD_3CN of **ImBn18C6**

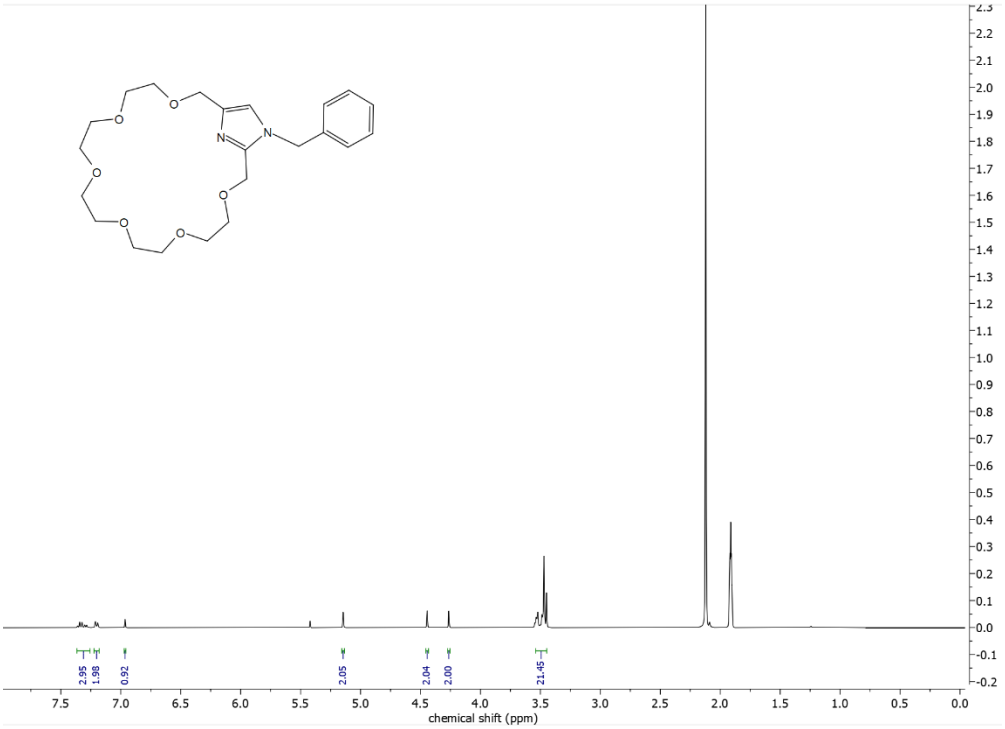

Figure S66 : ^{1}H NMR spectrum in CD_3CN of **ImBn21C7**

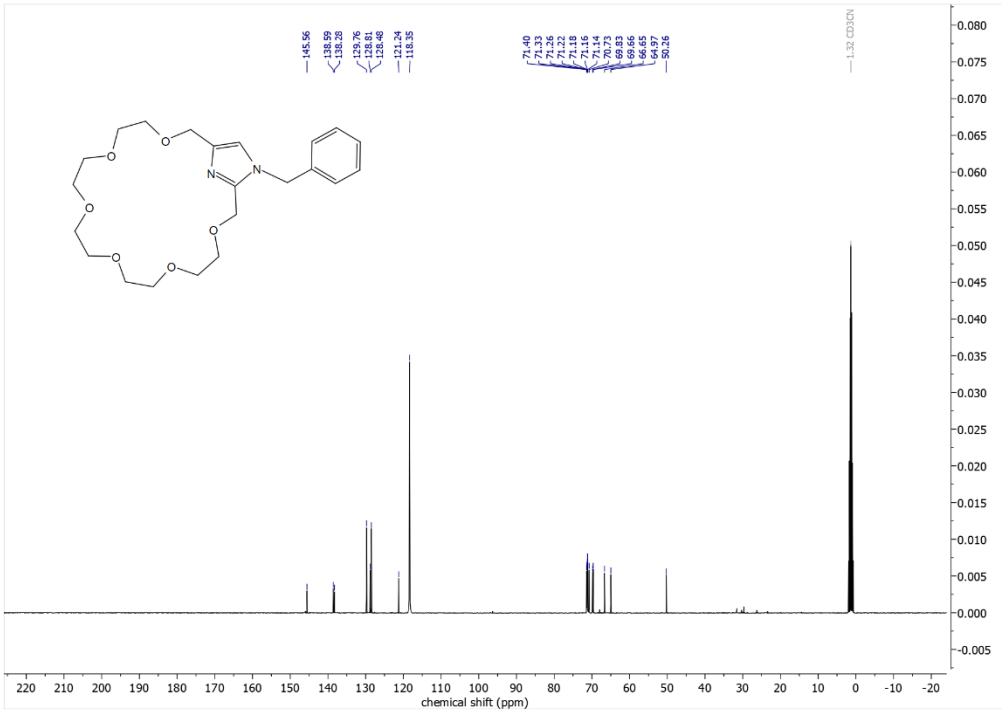

Figure S67: ^{13}C NMR spectrum in CD_3CN of **ImBn21C7**

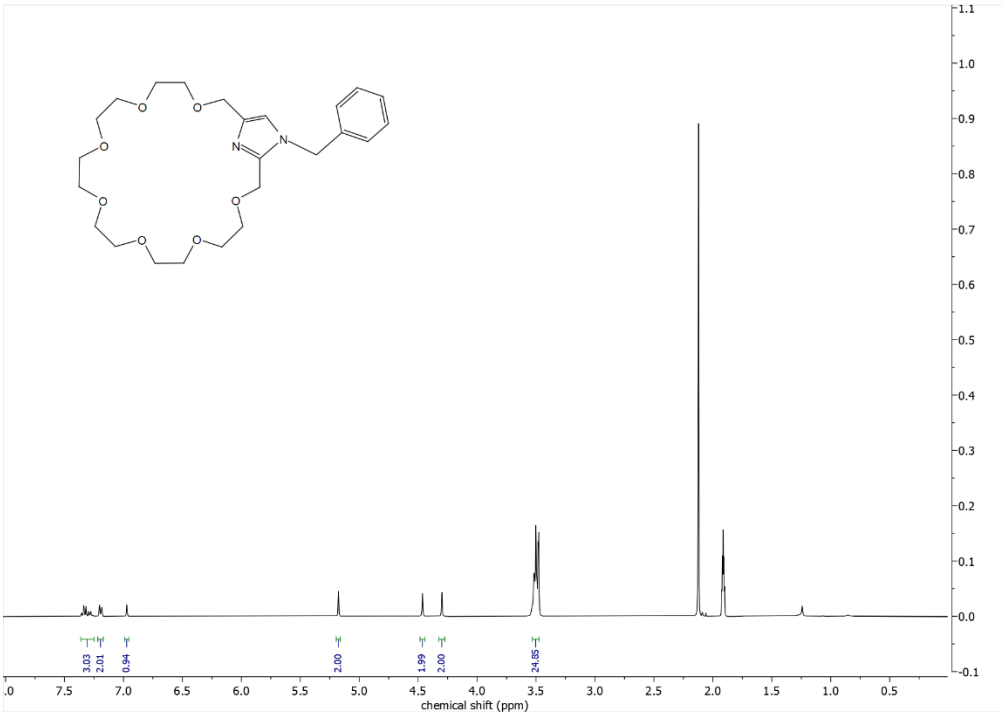

Figure S69: ^{1}H NMR spectrum in CD_3CN of **ImBn24C8**

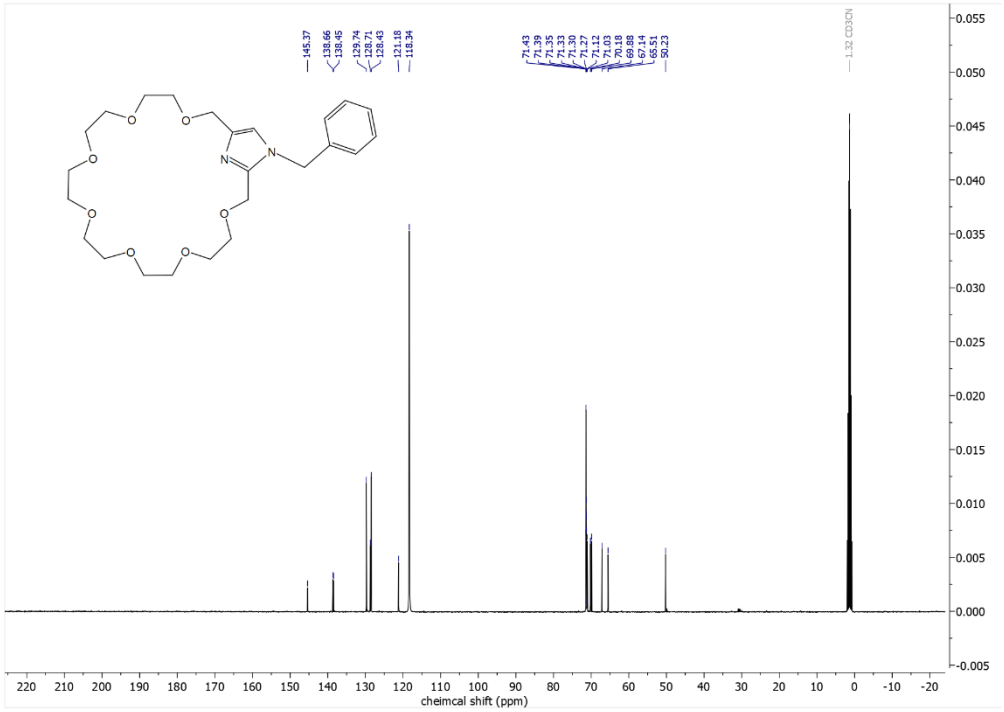

Figure S69: ^{13}C NMR spectrum in CD_3CN of **ImBn24C8**

Supporting Information References

1) Thordarson, P. Determining Association Constants from Titration Experiments in Supramolecular Chemistry. *Chem. Soc. Rev.* **2011**, *40* (3), 1305–1323. https://doi.org/10.1039/c0cs00062k.

2) Hibbert, D. B.; Thordarson, P. The Death of the Job Plot, Transparency, Open Science and Online Tools, Uncertainty Estimation Methods and Other Developments in Supramolecular Chemistry Data Analysis. *Chem. Commun.* **2016**, *52* (87), 12792–12805. https://doi.org/10.1039/C6CC03888C.

3) *CrysAlis*^{Pro}, version 1.171.37.35; Rigaku Oxford Diffraction

4) Sheldrick, G. M. (2015). *Acta Cryst.* A**71**, 3-8.

5) Sheldrick, G. M. (2015). *Acta Cryst.* C**71**, 3-8.

6) Pracht, P.; Bohle, F.; Grimme, S. Automated exploration of the low-energy chemical space with fast quantum chemical methods. *Phys. Chem. Chem. Phys.* **2020**, 22, 7169–7192. https://doi.org/10.1039/C9CP06869D

7) Bannwarth, C.; Caldeweyher, E.; Ehlert, S.; Hansen, A.; Pracht, P.; Seibert, J.; Spicher, S.; Grimme, S. *WIREs Comput. Mol. Sci.* **2020**, 11, e1493. https://doi.org/10.1002/wcms.1493

8) Bannwarth, C.; Ehlert, S.; Grimme, S. GFN2-xTB—An Accurate and Broadly Parametrized Self-Consistent Tight-Binding Quantum Chemical Method with Multipole Electrostatics and Density-Dependent Dispersion Contributions. J. Chem. Theory Comput. **2019**, 15, 1652–1671. https://doi.org/10.1021/acs.jctc.8b01176

9) Ehlert, S.; Stahn, M.; Spicher, S.; Grimme, S. Robust and Efficient Implicit Solvation Model for Fast Semiempirical Methods. *J. Chem. Theory Comput.* **2021**, 17, 4250–4261. https://doi.org/10.1021/acs.jctc.1c00471

10) Neese, F. Software update: the ORCA program system—Version 5.0. *WIREs Comput. Mol. Sci.* **2022**, 12, e1606. https://doi.org/10.1002/wcms.1606

11) Mardirossian, N.; Head-Gordon, M. ωB97X-V: A 10-parameter, range-separated hybrid, generalized gradient approximation density functional with nonlocal correlation, designed by a survival-of-the-fittest strategy. *Phys. Chem. Chem. Phys.* **2014**, 16, 9904–9924. https://doi.org/10.1039/C3CP54374A

12) Caldeweyher, E.; Ehlert, S.; Hansen, A.; Neugebauer, H.; Spicher, S.; Bannwarth, C.; Grimme, S. A generally applicable atomic-charge dependent London dispersion correction. *J. Chem. Phys.* **2019**, 150, 154122. https://doi.org/10.1063/1.5090222

13) Weigend, F.; Ahlrichs, R. Balanced basis sets of split valence, triple zeta valence and quadruple zeta valence quality for H to Rn: Design and assessment of accuracy. *Phys. Chem. Chem. Phys.* **2005**, 7, 3297–3305. https://doi.org/10.1039/B508541A

14) Neese, F.; Wennmohs, F.; Hansen, A.; Becker, U. Efficient, approximate and parallel Hartree–Fock and hybrid DFT calculations. A 'chain-of-spheres' algorithm for the Hartree–Fock exchange. *Chem. Phys.* **2009**, 356, 98–109. https://doi.org/10.1016/j.chemphys.2008.10.036

15) Barone, V.; Cossi, M. Quantum Calculation of Molecular Energies and Energy Gradients in Solution by a Conductor Solvent Model. *J. Phys. Chem. A* **1998**, 102, 1995–2001. https://doi.org/10.1021/jp9716997